ADVANCES IN A MICROPHYSICS PARAMETERIZATION TO PREDICT SUPERCOOLED LIQUID WATER AND APPLICATION TO AIRCRAFT ICING

by

GREGORY THOMPSON

B.S., Pennsylvania State University, 1990

M.S., Colorado State University, 1993

A thesis submitted to the

Faculty of the Graduate School of the

University of Colorado in partial fulfillment

of the requirement for the degree of

Doctor of Philosophy

Department of Atmospheric and Oceanic Sciences

2016

This thesis entitled:

Advances in a Microphysics Parameterization to Predict Supercooled Liquid Water and Application to Aircraft Icing

written by Gregory Thompson

has been approved for the Department of Atmospheric and Oceanic Sciences.

Peter Pilewskie

Balaji Rajagopalan

Date

The final copy of this thesis has been examined by the signatories, and we find that both the content and the form meet acceptable presentation standards of scholarly work in the above mentioned discipline.

Thompson, Gregory (Ph.D., Department of Atmospheric and Oceanic Sciences)

Advances in a microphysics parameterization to predict supercooled liquid water and application to aircraft icing

Thesis directed by Professor Katja Friedrich

Aerosols influence cloud and precipitation development in complex ways due to myriad feedbacks at a variety of scales from individual clouds through entire storm systems. This thesis describes the implementation, testing, and results of a newly-modified bulk microphysical parameterization with explicit cloud droplet nucleation and ice activation by aerosols (Chapter 2). Furthermore, in order to simulate properly the well known aerosol indirect effects, the explicitly-predicted cloud droplet and ice radiative effective size had to be fully coupled with the radiation parameterization. Since this connection did not previously exist within the Weather Research and Forecasting (WRF) model, the methodology to link these two parameterizations is detailed in Chapter 3. Subsequent evaluation of 28 daily WRF convection-permitting forecasts using the coupled cloud-radiation system resulted in sensible cloud-radiation indirect effects and modest improvements in simulated infrared brightness temperature, amount of solar radiation reaching the ground, and surface temperature. However, it also uncovered the fact that WRF run at this grid spacing (~4 km) generally under-predicted aerial coverage and depth of clouds, particularly in the mid-troposphere at temperatures conducive to ice accreting on aircraft. Further evidence of the model predicting insufficient clouds at typical aircraft icing temperatures of -5 to -20°C was found by comparing aircraft measurements of liquid water content (LWC), median volume diameter (MVD), and temperature against model results from a decade-long WRF simulation (Chapter 4). In general, WRF correctly represented the typical characteristics of LWC and MVD stratified by temperature that was found in aircraft data that were collected during icing events. Also, in a case study analysis, the model correctly predicted the occurrence of aircraft icing between 63 and 84% of the time for a nine-hour duration. Ultimately, however, this research indicates a need to consider sub-grid scale cloud production in WRF and to take into account the activation of aerosols as cloud condensation nuclei within unresolved eddies.

Acknowledgements

I greatly appreciate the tremendous support of Dr. Katja Friedrich and Laurie Conway in expertly facilitating my progress to reach this stage of my education and career. Also, Dr. Peter Pilewskie (CU), Dr. Balaji Rajagopalan (CU), Dr. Matthias Steiner (NCAR), and Dr. Ligia Bernardet (NOAA) provided me with superb advice and guidance to achieve this goal. As a non-traditional returning student to a university, I am grateful to fellow students such as Brian Rainwater, Ren Smith, Bobbie Wallace, Sabrina Cochrane, Rochelle Worsnop, and Ariel Morrison. In reaching this goal over two decades later than my B.S. and M.S. degrees, I realize how influential Drs. Craig Bohren, Bruce Albrecht, Tom Ackerman, William Cotton, and Roger Pielke have been to my intervening career as well as my education. Thank you all.

The work presented here would not have been possible without the support of my employer, the National Center for Atmospheric Research's Research Applications Laboratory. This is very gratefully acknowledged as well as the primary funding support for roughly twenty years from the Federal Aviation Administration's Aviation Weather Research Program. The FAA-AWRP office has ardently supported the research and development in aircraft icing that ultimately resulted in this thesis.

I extend high praise to long-time friends and colleagues including Ben Bernstein, Istvan Geresdi, Hugh Morrison, Jason Nachamkin, Aaron Braeckel, Arnaud Dumont, Terri Eads, Trude Eidhammer, and Alison Nugent. This core group of excellent scientists and close friends are to be commended for countless hours of fruitful discussions related to aircraft icing, cloud physics, storm chasing, computer programming, beer brewing (as well as choosing and drinking), and so much more. Mentorship from NCAR's Roy Rasmussen, Marcia Politovich, and Matthias Steiner helped to shape my career for which I'm very grateful.

But, the highest praise of all is reserved for the most significant people in my life, my parents, my incredible wife, Dee, and our two wonderful children, who have supported me in this endeavor more strongly than I deserved or could have ever expected. I shall thank them endlessly for giving me this life as an atmospheric scientist. Its somewhat stunning to trace a life's path back thirty-seven years to a Mid-Atlantic blizzard (President's Day storm, 19 Feb 1979) followed by daily viewing of Public Broadcasting System's ***A. M. Weather*** that most likely led to this very day.

Contents

Tables

Figures

1. Introduction

Ultimately, the genesis of nearly all naturally-occuring clouds are aerosol particles known as cloud condensation nuclei (CCN), which, in general, are smaller than a micron in size. Typical numerical weather prediction (NWP) models utilize grid scales of multiple kilometers that make the prospect of properly predicting CCN and resulting clouds and precipitation difficult. In addition, there are few direct and routine measurements of aerosols and CCN available to input into NWP models, particularly at levels above the earth's surface. Due to this lack of CCN information, most bulk cloud microphysics schemes in use in NWP models today assume a simplistic constant cloud droplet number concentration. However, cloud physicists have long recognized the importance of variable cloud droplet concentration as it affects the overall droplet sizes and resulting production of precipitation due to the collision-coalescence process.

With today's available high-performance computer hardware, NWP models have greatly increased model resolution as compared to a decade ago, but capturing all scales of vertical motions responsible for clouds still remains many decades away. Fluctuations in vertical velocity within a few meters distance greatly affect an air parcel's supersaturation value, which subsequently affects the activation of aerosols as CCN (Köhler, 1921). In the interim, there is a need for low computational cost and moderately complex aerosol treatments in NWP models in order to improve cloud, radiation, precipitation, and temperature forecasts. The subject matter of this thesis is the development and testing of a coupled "aerosol-aware" cloud microphysics scheme implemented into the Weather Research and Forecasting (WRF) model that utilizes two newly-added aerosol species, one for CCN and one for ice nucleation (IN). This effort represents an intermediate step in complexity since full aqueous chemistry and numerous aerosol species of differing sizes is prohibitively costly to run on existing computers at typical NWP model grid spacings. Therefore, with good basic fundamentals of overall aerosol number concentration, reasonable estimates of vertical velocity produced explicitly on the grid scale in a high resolution NWP model, and coupling of cloud particle sizes to radiation, the proposed framework may be used to test and refine the microphysics scheme through comparisons to existing observational data.

In Chapter 2, a detailed description of the recently developed "aerosol-aware" microphysics scheme is given. The scheme extends the one-moment cloud water variable previously described by Thompson et al. (2008) by predicting the number concentration of droplets directly activated by aerosols. Droplet activation is achieved using a pre-computed look-up table created using a more complex parcel model. Using both droplet number concentration and mixing ratio permits a more accurate representation of the particle size distribution. The new scheme was tested using idealized conditions first and then using a WRF 72-h simulation of a continental-scale winter cyclone. Sensitivity experiments with a basic state, or control input aerosol condition along with far more polluted and far cleaner aerosol conditions revealed sensitivities to cloud properties, radiation, and precipitation. The contents of Chapter 2 were published in the *Journal of the Atmospheric Sciences* (Thompson and Eidhammer, 2014: “A Study of Aerosol Impacts on Clouds and Precipitation Development in a Large Winter Cyclone”).

In Chapter 3, the methods to couple the explicitly-predicted cloud droplet and ice/snow sizes from the microphysics scheme as inputs to the radiation parameterization are detailed. Since aerosols directly affect the droplet number concentration and droplet size, this step was necessary to investigate the first aerosol indirect effect (Twomey, 1974). Prior versions of WRF microphysics and radiation schemes were not fully coupled, because the radiation scheme used a priori values for droplet or ice crystal sizes. Using the newer aerosol-aware microphysics, a more thorough treatment of aerosol-cloud interactions is now possible in WRF without using the far more computationally costly WRF-Chem model. Afterwards, the sensitivity of the coupling to radiation was tested in a 28-day study of high-resolution convective weather forecasts to see if there were improvements to incoming solar radiation, cloud-top-temperature (CTT), and surface temperature. The work in this chapter was published in *Atmospheric Research* (“Explicitly-Coupled Cloud Physics and Radiation Parameterizations and Subsequent Evaluation in WRF High-Resolution Convective Forecasts”).

In Chapter 4, the aerosol-aware scheme was used in an unprecedented high resolution, continental-scale, decade-long WRF simulation. The multi-year simulation permitted an investigation of the model’s ability to predict aircraft icing environments. Federal Aviation Administration (FAA) aircraft measurements in icing conditions spanning multiple decades and including the general characteristics of temperature, liquid water content, droplet concentration, and median volume diameter were compared to the same quantities predicted by the model. If the model can reproduce the conditions conducive to aircraft icing, then a real-time forecast system using the explicitly-predicted supercooled liquid water could be developed to warn pilots of potentially hazardous en route or surface icing conditions. A case study of a high-impact icing day that the FAA provided was analyzed in terms of the High Resolution Rapid Refresh model (a specific configuration of WRF) to predict supercooled water in the same approximate space as pilots who had reported icing on their aircraft. The research reported in this chapter is in the final stages of preparation to submit to the *Journal of Aircraft*.

The overall significance of the work discussed here is the description and robust testing of a moderately-complex aerosol-cloud-radiation-precipitation package of fully coupled physical parameterizations. This dissertation also shows just one example, aircraft icing, from a broad spectrum of potential applications that are now made possible. Using this framework, future studies can investigate the impacts of aerosol increases or decreases on cloud and precipitation development and associated changes to regional or continental-scale hydrology (at the seasonal or longer time scales). Also, it is plausible that WRF-model estimates of aerosol indirect effects could be quantified and used as a baseline for global climate model simulations. It is well recognized that aerosol indirect effects represent a key uncertainty in climate change projections (IPCC 2007) because traditional general circulation models (GCMs) do not adequately represent cloud and precipitation processes. With the new additions to WRF reported herein together with a baseline decade-long “Control” experiment at high resolution, there exists an opportunity to quantify the sensitivities of clouds, radiation, and precipitation to aerosol changes on a continental scale.

2. A study of aerosol impacts on clouds and precipitation development in a large winter cyclone

This chapter is reprinted with permission from:

Thompson, G and T. Eidhammer, 2014: A study of aerosol impacts on clouds and precipitation development in a large winter cyclone. J. Atmos. Sci., 71, 3636–3658.

2.0 Abstract

Aerosols influence cloud and precipitation development in complex ways due to myriad feedbacks at a variety of scales from individual clouds through entire storm systems. This paper describes the implementation, testing, and results of a newly-modified bulk microphysical parameterization with explicit cloud droplet nucleation and ice activation by aerosols. Idealized tests and a high-resolution, convection-permitting, continental-scale seventy-two hour simulation with five sensitivity experiments showed that increased aerosol number concentration results in more numerous cloud droplets of overall smaller size and delays precipitation development. Furthermore, the smaller droplet sizes cause the expected increased cloud albedo effect and more subtle longwave radiation effects. Although increased aerosols generally hindered the warm-rain processes, regions of mixed-phase clouds were impacted in slightly unexpected ways with more precipitation falling north of a synoptic-scale warm front. Aerosol impacts to regions of light precipitation, less than approximately 2.5 mm per hour, were far greater than impacts to regions with higher precipitation rates. Comparisons of model forecasts with five different aerosol states versus surface precipitation measurements revealed that even a large scale storm system with nearly a thousand observing locations did not indicate which experiment produced a more correct final forecast indicating a need for far longer duration simulations due to magnitude of both model forecast error and observational uncertainty. Lastly, since aerosols affect cloud and precipitation phase and amount, there are resulting implications to a variety of end-user applications such as surface sensible weather and aircraft icing.

2.1 Introduction

It is well known that aerosols affect cloud microphysics through their role in nucleating cloud and ice particles. An increase in aerosol concentration generally leads to more numerous, but smaller droplets for a given liquid water content, which results in an increase of the cloud albedo, known as the first indirect effect (Twomey, 1974). Further, due to decreases in cloud droplet size, precipitation processes can be delayed and reduced, which is referred to as the second indirect effect (Albrecht, 1989). However, numerous feedbacks and interactions with the ice phase and other aspects of cloud dynamics make it difficult to tease out exactly how cloud microphysical changes due to aerosol changes affect the radiative balance, precipitation and dynamics in a systematic and quantitative way (c.f., Levin and Cotton, 2009).

The role aerosols play in altering warm-phase clouds has been intensively studied for multiple decades, but, until recently, less attention has been devoted to aerosols affecting mixed-phase clouds. Whereas liquid-only clouds tend to be somewhat simpler to examine, aerosols may impact mixed-phase clouds by changing the overall population and/or size of droplets that potentially alter freezing (Bigg, 1953) and riming (Saleeby et al. 2009) processes as well as the vertical profile of latent heat release (c.f., Khain et al. 2008). Modeling studies that focused on single convective cloud systems or simulations performed for short time periods have found precipitation differences from a few to several hundred percent due to aerosols (e.g. review by Tao et al. 2012) including either/both increases or decreases in precipitation. To complicate matters, some precipitation sign differences may be responding to differing environmental conditions. For example, dry continental versus moist maritime convective clouds respond differently to changes in aerosols (Khain et al. 2008, 2009; Teller et al. 2008; Cui et al. 2011) and even the environmental wind shear was found to play a role in how aerosols affect convective clouds and resulting precipitation (Fan et al. 2009; Lee et al. 2008; Lebo and Morrison, 2013).

Recently, large-scale, high-resolution, and long-duration modeling studies have been conducted (Seifert et al. 2012; van den Heever et al. 2011; Grabowski and Morrison, 2011) and found that aerosol impacts to cloud systems interplay with the dynamics in a “naturally-buffered” system. Even when relatively large changes in aerosols were simulated, the resulting surface precipitation differences were only a few percent overall; although larger impacts may occur locally.

Other mixed-phase cloud types such as orographic clouds may reveal systematic precipitation impacts in varying aerosol conditions. For example, Saleeby et al. (2009) found a shift in the location of the precipitation, with a reduction on the windward slope and increase on the leeward side of a mountain barrier in wintertime orographic clouds. Although mountain-range total snow amount remained mostly unchanged, the distribution over the crest of a mountain range potentially impacts specific water basins. Similar findings were reported by Igel et al. (2013) in relation to aerosol impacts on precipitation in the vicinity of a warm front: precipitation reduced near the front but increased farther northward as aerosol concentration was increased. For the orographic cloud system, Saleeby et al. (2009) argued that the increase in precipitation on the leeward side was attributed to reduced riming on ice crystals due to reduced water droplet size in the more polluted conditions, which allowed the crystals to be carried farther downwind before reaching the ground. The warm frontal study also showed a less efficient snow riming process, but the precipitation increase distant from the warm front was attributed to increased accretion of cloud droplets by rain as aerosols increased the droplet number and liquid water content (LWC) but decreased overall droplet size.

Changes to cloud properties by aerosols are not only important to radiation, precipitation, and dynamics but also to any weather applications in which the phase and amount of water and ice content may be highly susceptible to small changes. For example, the amount of aircraft icing is directly dependent on the LWC and size of supercooled water droplets. Rosenfeld et al. (2013) attributed frequent incidences of aircraft icing near the U.S. west coast to clean maritime air with low concentrations of cloud condensation and ice nuclei and stressed the importance of including aerosols when modeling aircraft icing.

To address a complex and uncertain problem that affects storms from convective to synoptic scales, the Thompson et al. (2008) bulk microphysics scheme was recently updated to incorporate aerosols explicitly in a simple and cost-effective manner. The scheme nucleates water and ice from their dominant respective nuclei and tracks and predicts the number of available aerosols. Using the Weather Research and Forecasting (WRF) model (Skamarock et al. 2008), the scheme was tested in a high-resolution (4-km grid spacing) simulation of a three-day winter storm event over the entire contiguous U.S. The previous version of the scheme is widely used and well tested in WRF for quantitative precipitation forecasts (QPF) applications (Rasmussen et al, 2011; Ikeda et al. 2010; Molthan et al. 2012), because it consistently compares well to precipitation measurements (Liu et al. 2011) and was developed with in-flight aircraft and ground icing applications in mind (Nygaard et al. 2011; Podolskiy et al. 2013). Therefore, we believe it is well suited to address potential connections of aerosol impacts to cloud properties that subsequently affect radiation, precipitation amount and type, and aircraft icing.

This paper is organized as follows: a description of the numerical model is found in the next section along with more detailed descriptions of the activation of water and ice by two aerosol species. Results of the newly coupled aerosol-cloud physics parameterization tested under idealized flow conditions are presented in Section 2.3. Next, a synoptic-scale, multi-day winter cyclone is presented in Section 2.4 along with results from a suite of high resolution, continental-scale model simulations including sensitivity experiments using different aerosol number concentrations. The final section contains a summary and conclusions.

2.2 Numerical model

The simulations in this study were performed using the Weather Research and Forecasting (WRF) model, version 3.4.1 with modifications discussed below. The WRF model includes many choices for various physical parameterizations of radiation, boundary layer, microphysics, and land-surface interactions, but we avoided the use of a cumulus parameterization by applying a high resolution grid as discussed in Section 2.4. Most pertinent to this study, we used the Thompson et al. (2008) bulk microphysics scheme that treats five separate water species: cloud water, cloud ice, rain, snow, and a hybrid graupel/hail category. To minimize computational cost, prior versions of this scheme utilized one-moment prediction of mass mixing ratio for some species (cloud water, snow, and graupel) mixed with two-moment prediction (addition of number concentration) of cloud ice and rain. The number concentrations of single-moment species could be diagnosed from mixing ratio and various diagnostic relations between size distribution shape and other parameters found in the scheme. Cloud water was assumed to follow a generalized gamma distribution with a diagnostic but variable "shape parameter" based on a pre-determined value of droplet number concentration set in the code, which was always intended to be changed by users for specific cases.

The scheme has now been updated to incorporate activation of aerosols as cloud condensation and ice nuclei and, therefore, explicitly predicts the droplet number concentration of cloud water as well as the number concentrations of the two new aerosol variables, one each for CCN and IN. Rather than determine a priori the specific aerosol types and chemical composition of multiple aerosol categories, which can lead to high computational burden and significant complexity, we simply refer to the hygroscopic aerosol as a “water-friendly” (N_{wfa}) aerosol and the non-hygroscopic ice nucleating aerosol as “ice-friendly,” (N_{ifa}) although the latter is primarily considered to be dust. Consistent across all forms of water species (vapor, liquid, or solid), each species mass mixing ratio or number concentration follows the same governing conservation equation:

$$\frac{\partial\Phi}{\partial t} = -\frac{1}{\rho}\nabla\cdot(\rho\mathbf{U}\Phi) - \frac{1}{\rho}\frac{\partial(\rho V_\Phi\Phi)}{\partial z} + \delta\Phi + S_\Phi, \tag{1}$$

where Φ is mass mixing ratio or number concentration of any water species, t is time, ϱ is the air density, $\boldsymbol{U}$ is the 3D wind vector, z is height, V_Φ is the appropriately-weighted fallspeed of Φ, $\delta\Phi$ represents the sub-grid scale mixing operator, and S_Φ represents the various microphysical process rate terms. Descriptions of the numerous process rate terms for previously existing species are found in Thompson et al. (2004, 2008) while the terms for newly predicted variables of cloud droplet number concentration, N_c, and the number of each aerosol species, N_{wfa} and N_{ifa} are provided in Eqs. 2 4 below along with more detailed descriptions of specific terms found in subsequent paragraphs:

$$\begin{aligned}\frac{dN_c}{dt} = &-\begin{pmatrix}\text{rain, snow, graupel}\\ \text{collecting droplets}\end{pmatrix} - \begin{pmatrix}\text{freezing into}\\ \text{cloud ice}\end{pmatrix} - \begin{pmatrix}\text{collide/coalesce}\\ \text{into rain}\end{pmatrix} - (\text{evaporation})\\ &+ \begin{pmatrix}\text{CCN}\\ \text{activation}\end{pmatrix} + \begin{pmatrix}\text{cloud ice}\\ \text{melting}\end{pmatrix},\end{aligned} \tag{2}$$

$$\begin{aligned}\frac{dN_{\text{wfa}}}{dt} = &-\begin{pmatrix}\text{rain, snow, graupel}\\ \text{collecting aerosols}\end{pmatrix} - \begin{pmatrix}\text{homogeneous nucleated}\\ \text{deliquesced aerosols}\end{pmatrix} - (\text{CCN activation}) + \begin{pmatrix}\text{cloud and rain}\\ \text{evaporation}\end{pmatrix}\\ &+ \begin{pmatrix}\text{surface}\\ \text{emissions}\end{pmatrix},\end{aligned} \tag{3}$$

$$\frac{dN_{\text{ifa}}}{dt} = -\begin{pmatrix}\text{rain, snow, graupel}\\ \text{collecting aerosols}\end{pmatrix} - (\text{IN activation}) + \begin{pmatrix}\text{cloud ice}\\ \text{sublimation}\end{pmatrix} + \begin{pmatrix}\text{surface}\\ \text{emissions}\end{pmatrix}. \tag{4}$$

As compared to the prior Thompson et al. (2008) scheme with eight microphysics species to advect/predict, the new scheme with its three additional variables increases computational cost by approximately 16%. The most significant increase in computing time is due to advection of new species, not the additional coding of various source/sink terms. In contrast, the simplest of WRF-Chem options available at the time of writing increases the number of variables by over a factor of two, which would massively impact computer memory and time. The subsections below describe the aerosol activation methods and input aerosol dataset used in simulations discussed in subsequent sections.

2.2.1 Cloud droplet nucleation

Cloud droplets nucleate from explicit aerosol number concentration (N_{wfa}) using a look-up table of activated fraction determined by the model's predicted temperature, vertical velocity, number of available aerosols, and pre-determined values of hygroscopicity parameter (0.4 in experiments performed in this research) and aerosol mean radius (0.04 μm). The look-up table was created by explicit treatment of Kohler activation theory using these five variables within a parcel model by Feingold and Heymsfield (1992) with additional changes by Eidhammer et al. (2009) to use the hygroscopicity parameter (Petters and Kreidenweis, 2007). This implementation follows the same basic structure used by the Regional Atmospheric Modeling System (RAMS) as described by Saleeby and Cotton (2004, 2008) in which an assumed log-normal distribution with different values of aerosol mean radius and a constant geometric standard deviation (1.8) were pre-set as parameters when creating the table. The activation of aerosols as droplets in the new scheme is done at cloud base as well as anywhere inside a cloud where the look-up table value is greater than the existing droplet concentration. Nucleation of new droplets is prevented when existing ice hydrometeors would otherwise grow by water vapor deposition in a single time step that causes sufficient depletion of vapor to result in water sub-saturated conditions; however this rarely occurs in most updrafts because ice growth processes are relatively slow. Upon nucleation, the participating aerosols are removed from the population (third term in Eq. 3), though they can be restored as regenerated aerosols, to the parent category, via hydrometeor evaporation in which one aerosol is returned to Nwfa for each cloud or rain drop evaporated (represented by the fourth term in Eq. 3). Furthermore, aerosols are removed by precipitation scavenging (first term in Eq. 3) using aerosol collision efficiencies computed following Wang et al. (2010) using a standard geometric sweep-out such as performed by other parts of the microphysics such as rain collecting cloud water.

For this study, any effects of sub-grid turbulence on vertical velocity and nucleation of water droplets or ice were neglected, however the newly added variables of aerosol number concentrations were mixed consistently with heat, moisture, and momentum fluxes produced by the boundary-layer parameterization (represented by $\delta\Phi$ in Eq. 1). The simulations discussed below in Section 2.4 used relatively high-resolution grid spacing of 4 km and primarily included well-organized clouds forced by large-scale ascent that suffice to exclude sub-grid-scale vertical motions, however, simulations with coarser resolution should consider potential contributions by a distribution of vertical velocities within a model single grid box. Possible alternatives to relate a distribution of vertical velocities coupled with model-predicted TKE or eddy diffusivity variables to nucleate droplets (Ghan et al. 1997; Morrison and Pinto, 2005; Morrison and Gettelman, 2008; Morales and Nenes, 2010) were bypassed to keep the new version consistent with the simpler one-moment cloud water scheme. Likewise, the RAMS simulations of Saleeby and Cotton (2004, 2008) and Igel et al. (2013) activated aerosols as droplets using grid-scale velocities only. A future version will likely incorporate the sub-grid scales using guidance from LES simulations to parameterize CCN activation due to turbulence, but we avoided this complication at this early stage. However, since the model may have a small downward vertical velocity and yet be fully saturated, although likely to be brief, the CCN activation by the look-up table assumes a minimum upward velocity of 1 cm s^{-1}.

The “water-friendly” aerosol category was designed to be a combination of sulfates, sea salts, and organic matter, because these aerosols represent a significant fraction of known CCN and are found in abundance in clouds worldwide. At this time, black carbon was ignored. More sophisticated aerosol treatments could be incorporated into future versions, but the competition for water vapor to nucleate cloud droplets with many aerosol constituents of unknown chemical composition is poorly understood and subject to further research before incorporation into a mesoscale numerical weather prediction model. Additionally, several studies have concluded that chemical properties are not nearly as important as the assumed aerosol number/size distribution (e.g., Dusek et al. 2006; Ward et al. 2010). The scheme is currently capable of representing different aerosol populations by altering the hygroscopicity and aerosol mean radius variables, although, for this study, these variables were held constant throughout. Additionally, the simulations presented here are intended to be sensitivity experiments using first-order approximately representative aerosol number concentrations, mean size, and hygroscopicity while we do not claim to be forecasting precise aerosol amounts/composition.

2.2.2 Cloud ice activation

Cloud ice activates based on the number concentration of mineral dust aerosols since this species is considered to be highly active and most abundant naturally-occuring ice nuclei in the atmosphere (DeMott, 2003; Cziczo, 2004; Richardson, 2007; Hoose, 2010; Murray et al. 2012). While other constituents may act as ice nuclei, the best direct correlation of activated ice crystals and aerosols acting as nuclei appears to be dust. Similar to CCN activation, the addition of more aerosol species acting as IN leads to unnecessary complications as multiple species compete for the water vapor in complex ways. A future version of the scheme may incorporate other ice nuclei when future research clearly indicates such a requirement. The number of dust particles that nucleate into ice crystals is determined following the parameterization of DeMott et al. (2010) when above water saturation to account for condensation and immersion freezing and by the parameterization of Phillips et al. (2008) when less than water saturated to account for deposition nucleation. In addition, the freezing of deliquesced aerosols using the hygroscopic aerosol concentration is parameterized following Koop et al. (2000), shown as the second term in Eq. 3.

The freezing of existing water droplets continues to follow the Bigg (1953) volume and temperature parameterization as previously used in Thompson et al. (2008), except that the dust aerosol concentration alters the “effective temperature” to freeze more (or fewer) water drops when more (or fewer) dust particles are present. This connection intends to increase nucleation by considering the higher likelihood of contact nucleation by Brownian motion causing a dust particle to come into contact with a supercooled water droplet. As currently implemented based on an inspection of typical background dust concentration of 0.1 particles per liter of air, there is no alteration of the freezing of water droplets due to dust when compared against the prior Bigg’s freezing implementation in the Thompson et al. (2008) scheme. However, for each order of magnitude increased (decreased) number concentration, the effective temperature for freezing of droplets is decreased (increased) by one degree. Quantitatively, we have no basis for instituting this ad hoc method of altering the water drops freezing point by the presence of dust, only qualitative belief that some effective increase in freezing water drops due to the presence of high dust concentration is likely due to an increased likelihood of freezing by contact nucleation or immersion via an embedded dust nuclei inside of water drops. All of the ice nucleation mechanisms by dust can be readily switched off in favor of using the previous ice nucleation scheme as found in Thompson et al. (2008). Separate ice nucleation sensitivity experiments are beyond the scope of this study and will be reported in the future since this study focuses exclusively on aerosols acting as CCN, except a single test of the old versus new ice nucleation techniques was performed for an idealized test discussed in Section 2.3. However, since the freezing of water drops contains explicit dependence on their size (volume), there are implicit links to aerosol sensitivities found in the mixed-phase region discussed in detail below (Section 2.4) even without altering the ice nucleation methods explicitly.

2.2.3 Aerosol input data

The aerosol number concentrations in the winter storm simulations in Section 2.4 were derived from multi-year (2001-2007) global model simulations (Colarco, 2010) in which particles and their precursors are emitted by natural and anthropogenic sources and are explicitly modeled with multiple size bins for multiple species of aerosols by the Goddard Chemistry Aerosol Radiation and Transport (GOCART) model (Ginoux et al. 2001). The aerosol input data we used included mass mixing ratios of sulfates, sea salts, organic carbon, dust, and black carbon from the 7-year simulation with 0.5-degree longitude by 1.25-degree latitude spacing. We transformed these data into our simplified aerosol treatment by accumulating dust mass larger than 0.5 μm into the ice nucleating, non-hygroscopic mineral dust mode, N_{ifa} and combining all other species besides black carbon as an internally-mixed cloud droplet nucleating, hygroscopic CCN mode, N_{wfa}. Input mass mixing ratio data were converted to final number concentrations by assuming log-normal distributions with characteristic diameters and geometric standard deviations taken from Chin et al. (2002; Table 2).

For simplicity, we implemented a variable lower boundary condition that represents aerosol emissions based on the starting near-surface aerosol concentration and a simple mean surface wind to calculate a flux (constant through time) using the following relation applied only to the model lowest level, represented by the last term in parenthesis in Eq. (3): $dN_{wfa}/dt = 10^{[LOG(N_{wfa})-3.69897]}$, which results in 0.01×10^6 kg^{-1} s^{-1} for N_{wfa} = 50 cm^{-3}, 0.1×10^6 kg^{-1} s^{-1} for N_{wfa} = 500 cm^{-3} and 1.0×10^6 kg^{-1} s^{-1} for N_{wfa} = 5000 cm^{-3} for example. A 3-day averaging test revealed that the aerosol number concentration remained very close to the

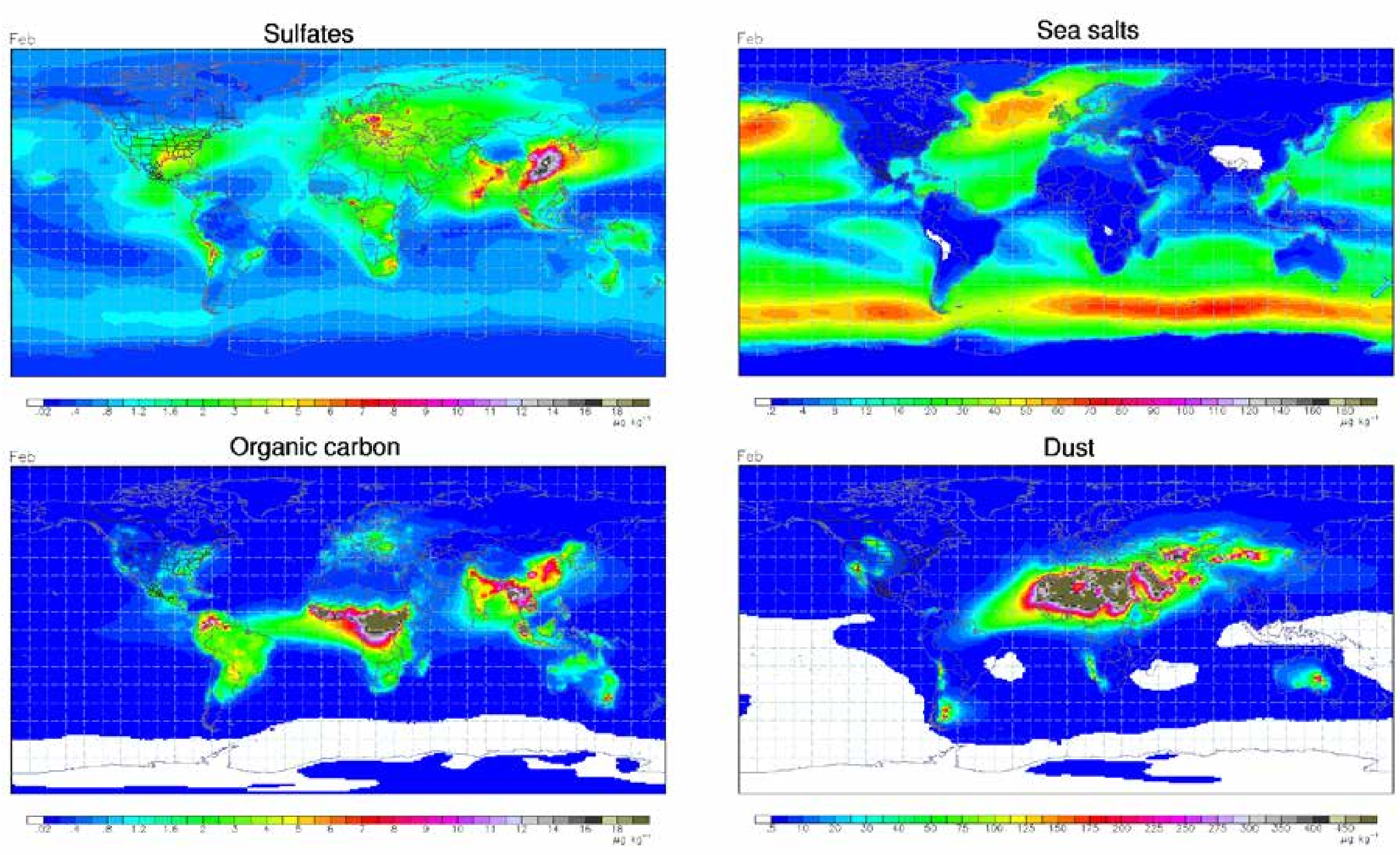
Sulfates

Sea salts

Organic carbon

Dust

FIG. 2.1: Sample global climatological mixing ratio (μg kg^{-1}) of aerosols of sulfate, sea salt, organic carbon, and dust for the month of February at model level nearest the surface created from a 7-year GOCART model simulation.

climatological condition over most of the domain, revealing that this simple assumption is more advanced than holding initial aerosol concentration constant as other studies have done (Igel et al. 2013). An earlier test that held only the lowest model level constant in time everywhere led to an obvious and unrealistic domain-wide increase in aerosols over the three day simulation. Our oversimplification can be remedied in future versions using more explicit aerosol emissions inventories or coupling with a full chemistry model such as WRF-Chem (Grell, 2005) or WRF-CMAQ (Wong et al. 2012).

In this application, the aerosols represent a monthly climatology sufficient for running a series of sensitivity experiments. It was not our intent to produce a proper simulation of the aerosol conditions of a particular event since such measurements are not widely available in space and time over a scale of the simulations in Section 2.4. Samples of the climatological aerosol dataset are shown in Fig. 2.1 and were interpolated to the WRF model horizontal and vertical points for initial and lateral boundary condition data.

2.3 Idealized Tests

For fundamental testing, WRF was configured using simple two-dimensional flow over a hill similar to tests of prior versions of the scheme described in Thompson et al. (2004, 2008). We used a domain with 600 points, spaced 1 km apart and 72 vertical levels spaced from 50 m near the surface to 250 m near the mid-troposphere, and the model was integrated for six hours. To test the warm-rain process in complete isolation from potential complications of the ice physics, the initial temperature profile was warmed to avoid cloud tops reaching glaciation temperatures. Horizontal wind linearly increased from zero at the surface to 10 m s^{-1} at 1 km and above and impinged on a 1-km high and 25-km half-width mountain barrier that produced a maximum updraft velocity of 0.2 m s^{-1} (see Fig. 2.2). Other sensitivity tests with a steeper 10-km half-width mountain increased the maximum updraft velocity to 0.5 m s^{-1} in order to test higher aerosol activation rates. Two initial aerosol conditions with exponentially decreasing profile of concentration from the surface to 2 km and constant amount above were used to test aerosol sensitivity. In one experiment, a surface aerosol concentration of 250 cm^{-3} decreased to 50 cm^{-3} aloft, which might be typical of a clean maritime air mass, whereas a second experiment started with 1000 cm^{-3} near the surface and decreased to 250 cm^{-3} aloft (see Fig. 2.2), which might be more typical of a continental air mass.

Additional experiments including the ice phase were performed in which the thermodynamic profile was cooled to match the same temperature and moisture profile used in Thompson et al (2008), otherwise the conditions shown in Fig. 2.2 were maintained, but only the steeper mountain profile was used. In order to refer to the sensitivity experiments with abbreviated reference names, we use the following nomenclature: "Warm" or "Cold" describes the simulations excluding and including ice phase, respectively; "25" and "10" refer to the mountain half-width; and "Mar" and "Con" refer to the Maritime and Continental aerosol concentrations, respectively, as shown in Table 2.1.

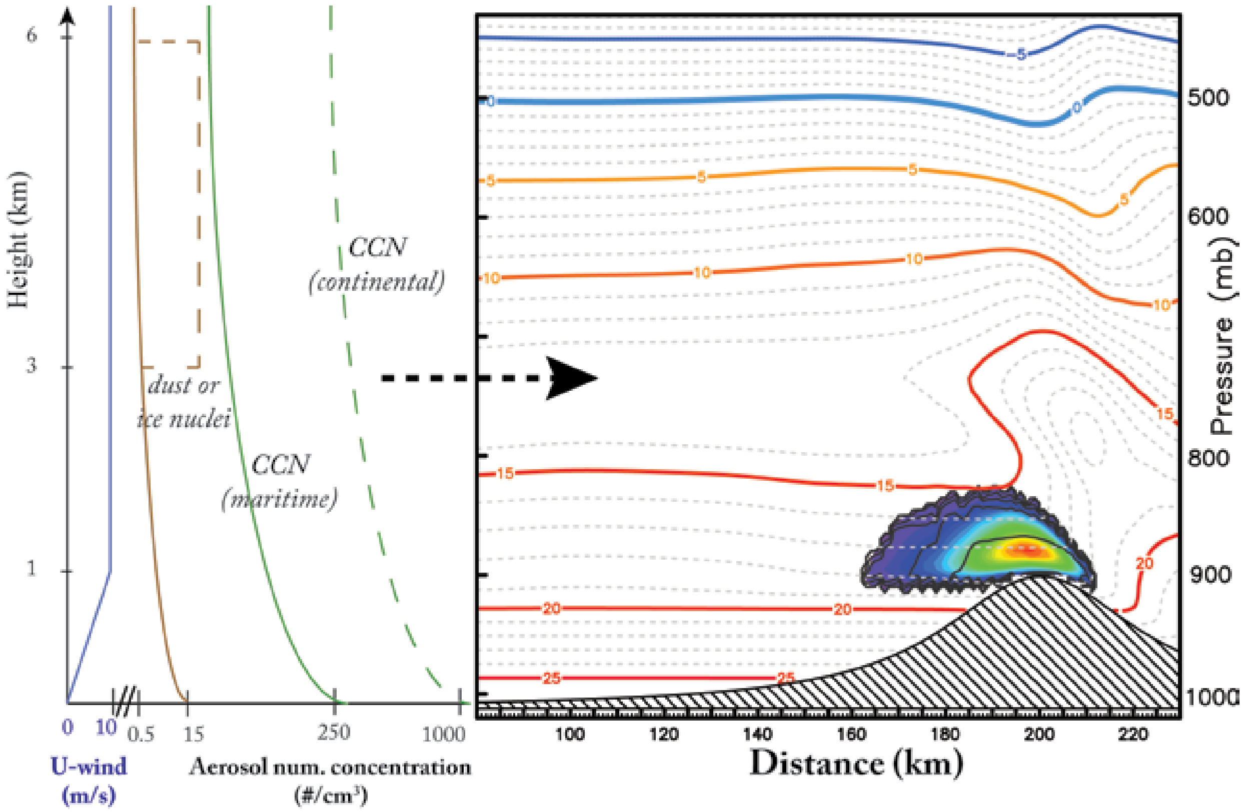

Fig. 2.2: Initial condition profiles of U-wind, CCN aerosol concentration and IN aerosol concentration for the WRF idealized "bell-hill" sensitivity experiments. Cloud water content (color filled; maximum=~0.5 g/cm^{-3}) at 3 hours is shown in the right portion of the figure along with temperature lines (colored lines every 5°C; dashed every 1°C).

As expected, all simulations with higher aerosol concentration caused a corresponding increase in cloud droplet number concentration since the updraft strength and attendant liquid water content (LWC) remained nearly constant. Fig. 2.3 shows that the low aerosol concentration experiments had about twice as many grid points with droplet concentrations below 50 cm^{-3} compared to simulations with higher number of aerosols. Also, the Continental experiments produced a flat range of droplet concentrations from 25 to 200 cm^{-3} because the updrafts were relatively weak while the Maritime experiments produced no droplet concentration exceeding 100 cm^{-3}. Table 2.1 shows that the computed mean cloud droplet concentration remained quite low, on average, at only 54 to 72 cm^{-3} for the continental experiments, which was two to three times larger than the 25 cm^{-3} of the Maritime experiments.

TABLE 2.1: Results from series of WRF idealized experiments without ice phase (WARM) or with ice phase (COLD), with 25 or 10-km half-width mountain barrier and with Maritime (Mar) or Continental (Con) aerosol concentration.

Experiment name	With ice?	Barrier half-width (km)	Initial aerosols	Mean droplet concentration (cm^{-3})	Mean droplet size (μm)	Time to rain (mm:ss)
Warm_25_Mar	No	25	Maritime	25	13.5	30:35
Warm_25_Con	No	25	Continental	54	9.5	1:00:15
Warm_10_Mar	No	10	Maritime	28	13.4	16:40
Warm_10_Con	No	10	Continental	72	9.8	27:55
Cold_10_Mar	Yes	10	Maritime	27	11.0	08:50
Cold_10_Con	Yes	10	Continental	68	8.1	17:55

Since the LWC was nearly constant regardless of aerosol concentration, the larger droplet concentration in the Continental experiment must contain smaller overall droplet sizes that greatly affect the ability of the cloud to form rain from the collision-coalescence process. This is readily confirmed in Table 2.1 that shows the median size of cloud droplets was only 9.5 μm in the Continental experiments versus 13.5 μm in the Maritime experiments. Furthermore, we see that the Maritime experiment with the steeper mountain slope was the first to produce rain (16:40), taking roughly half the time that was needed in the higher aerosol number concentration of experiment Continental (27:55). The broader, 25-km half-width mountain required nearly twice the time in each experiment to produce rain due to its weaker updraft. In other words, the strong updrafts associated with the steeper terrain simply

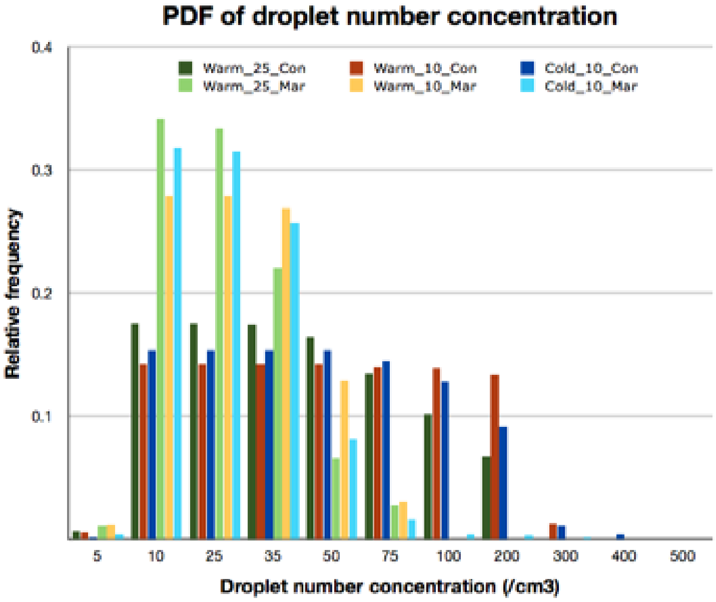

FIG. 2.3: Histogram of relative frequency of WRF model grid points with specific quantities of cloud water droplet number concentration from each of the sensitivity experiments run for the idealized "bell-hill" 2D flow case. Also refer to Table 1 for other parameters.

supply condensing water at a more rapid pace that enhances droplet growth to rain sizes far more effectively than impacts due to changing aerosol concentrations, droplet number, or size combined with the weaker updrafts.

When the temperature profile was cooled to match the sounding used in Thompson et al. (2004), the simulation produced a cloud with a temperature of -13°C at its top and ice formed in the simulations. However, rather than initiating ice solely from a temperature-dependent function following Cooper (1986), the mineral dust aerosol was responsible for ice initiation as described earlier. The inclusion of ice roughly halved the time to produce precipitation from 16:40 to 8:50 in the Maritime experiments or from 27:55 to 17:55 in the Continental experiments. The smaller overall number concentration and mean size of cloud droplets was due to riming of droplets onto snow. Another test (not shown) in which the scheme was changed back to the original Cooper (1986) ice nucleation did not alter the precipitation timing or amounts noticeably. A final experiment (not shown) in which the dust aerosol was increased by a factor of three between 3 and 6 km, as shown in Fig. 2.2, also had a negligible effect on precipitation. These additional tests do not reveal significant impacts of ice initiation sensitivity because the cloud was simply too shallow and warm to contain significant ice. Analysis of ice sensitivities remains as future work.

2.4 Winter cyclone simulations

Between 31 Jan and 2 Feb 2011, a large extratropical winter cyclone developed in the central USA and moved eastwards across the Appalachian mountains. With this storm came a variety of surface weather including near-record low temperatures and light snow in the northern High Plains, regions of lake effect snow in the Great Lakes, moderate to heavy snowfall in the Central Plains, a mixture of snow, ice pellets and freezing rain from the Ohio River Valley to New England, and moderately strong convection in the Southeast in advance of the cold front. In addition, a weak upper-air low-pressure system moved slowly eastward across the Desert Southwest region producing mostly light snowfall in the southern Rocky Mountains. In the central part of the country, the storm has been called “The Groundhog Day Blizzard” (NCDC, http://www.ncdc.noaa.gov/billions/events.pdf) since one to two feet of snow paralyzed the city of Chicago and caused an estimated $1.8 billion worth of damage along with 36 deaths in a multi-state region.

For each six-hour period within the three-day storm, between 350 and 500 surface weather reporting sites recorded a trace or more of precipitation and nearly 1000 sites across the whole country recorded precipitation in the 3-day period. Because of the widespread impact of the storm, and myriad of cloud and precipitation forcing mechanisms, including synoptic, mesoscale, and orographic, we believe the event is well suited for extensive modeling sensitivity experiments.

2.4.1 Model configuration

WRF was configured with a single convection-permitting grid of 4 km horizontal spacing with 1200 x 825 grid points covering the entire contiguous U.S., also using reasonably high vertical resolution with 72 levels up to model top at 73 hPa with stretched spacing from 50 m near the surface to 750 m near the tropopause. Input and lateral boundary condition atmospheric data were supplied by the Rapid Update Cycle (RUC) model analyses every three hours. The simulations utilized the Noah land surface model (Barlage et al. 2010), Yonsei University planetary boundary layer scheme (Hong et al. 2006), and the Rapid Radiative Transfer Model (RRTM-G; Iacono et al. 2000) radiation scheme and no convective parameterization since the grid was sufficiently high-resolution to predict most clouds explicitly.

At the time of writing, no existing radiation scheme in publicly-available WRF code utilizes fully coupled effective radii of all hydrometeor species as known within the microphysics scheme into the radiative computations involving clouds, which is insufficient for performing aerosol-cloud sensitivity experiments. Therefore, this missing link was remedied by explicitly computing the effective radii of cloud water (c.f., Slingo, 1989), ice, and snow (c.f., Stephens et al. 1990) directly in the microphysics scheme and passing those values to the RRTM-G scheme to calculate the cloud optical depth parameter. At present, the sulfates, sea salt, organic carbon and dust aerosols used by the microphysics scheme to activate water droplets and ice crystals do not scatter or absorb radiation directly and only the typical background amounts of gasses and aerosols present within the RRTM-G scheme were considered for scattering/absorption/emission of direct radiation in this study.

Fig. 2.4 shows results of the WRF Control simulation at 42 hours, valid at 1800 UTC 01 Feb 2001 and reveals broad regions of snow (blue color-fill: 1-h snow amount) and rain (green color-fill: 1-h rain amount) with an overlapping region of both plus graupel (red color-fill: 1-h graupel amount). The gray-shaded regions represent the accumulated total precipitation amount thus far in the simulation and the various red/

blue-shaded dots represent the difference between observed and WRF-simulated 6-h precipitation. The storm obviously impacted a very large portion of the U.S. and includes very typical extratropical cyclone characteristics of a synoptic-scale warm and cold front as well as less obvious orographic forcing, lake-effect snow, and convection.

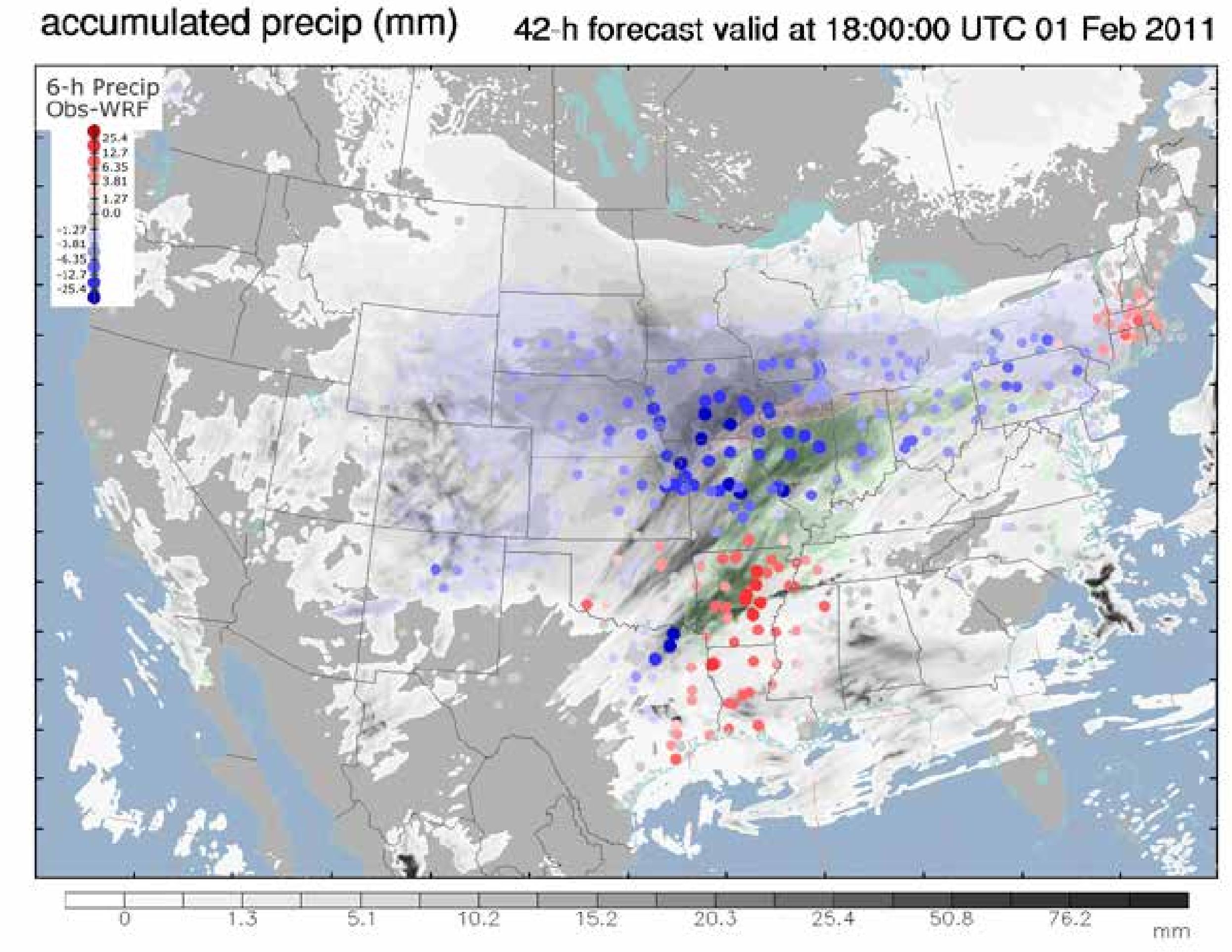

Fig. 2.4: WRF 42-h forecast of accumulated precipitation (mm; gray-filled shades) valid 1800 UTC 01 Feb 2011 with semi-transparent overlay of 1-h snow amount (blue color-filled regions), 1-h rain (green color-filled regions), 1-h graupel (red color-filled regions), blue/red color-fillled dots represent 6-h observed minus WRF precipitation amounts showing areas of over-forecast (blue dots) precipitation and under-forecast (red dots) precipitation.

2.4.2 Sensitivity experiments

A suite of sensitivity experiments was run to test in a robust and comprehensive manner the physics of the new aerosol-aware microphysics in contrast to the non-aerosol scheme as well as the impact of changing the amount of aerosols on cloud and precipitation development. First, to create a set of benchmark tests, the non-aerosol scheme with original 1-moment cloud water (Thompson et al. 2008) was run with constant and extremely low droplet concentrations of 50 cm^{-3}, followed by a moderately high value of 750 cm^{-3}. These simulations represent very clean versus moderately polluted conditions and provide reasonable bounds for the simulations using explicit aerosols. We will refer to these as “Nc50” and “Nc750” respectively. Second, the aerosol-aware scheme was run with the input and lateral boundary condition data as described in Section 2.2.3 with the first simulation representing aerosol conditions that should be representative of conditions present in the current era. This simulation will be referred to as “Control.” Next, a simulation that reduced at all model grid points the aerosol number concentration to one-tenth the control concentrations, “Clean,” and a final simulation with ten times the control concentrations, “Polluted” were performed. Changes to aerosol characteristics such as chemical composition, hygroscopicity, or mean radii were not tested for these simulations, solely the aerosol number concentrations. Furthermore, there were no changes made to the non-hygroscopic aerosol (dust) number concentration in order to minimize any changes due to ice nucleation in these tests.

Although the benchmark tests used single values of droplet number concentration that were constant in space and time, the computed radiative effective size was fully coupled into the radiation scheme as described previously. If the aerosol-aware scheme produced results that varied wildly in comparison to the benchmark experiments with low and high droplet concentrations, then almost certainly an error in coding would be indicated. Furthermore, the benchmark experiments provide bounds to cloud, precipitation, and radiation properties and impacts for simulations where aerosols were explicitly introduced.

2.4.3 Cloud property impacts

Consistent with the results of the 2-D idealized tests, the fully 3-D simulation showed the expected result that number concentration of cloud droplets increased with increasing aerosol concentration. Along with the increase in droplet concentration, a very prominent decrease in mean size of droplets was noted, and, since the radiation scheme properly accounted for the radiative effective radius, there was an absolute indication of the first aerosol indirect effect: the “cloud albedo” effect (Twomey, 1974). Fig. 2.5 shows mostly positive differences of cloud droplet concentration (top panel; warm colors), mostly negative differences of mean effective radius (middle panel; cool colors), and mostly increased outgoing shortwave radiation (bottom panel; warm colors) when subtracting the less polluted Clean simulation from the higher aerosol concentration Control simulation. Numerically, the average difference of reflected shortwave radiation in these two simulations was a 5.4% increase in cloud albedo due higher aerosol concentration of the Control vs. Clean experiments when computed from 6-h intervals during daylight hours. This behavior was entirely consistent when any of the experiments with lower aerosol or droplet concentration was subtracted from a corresponding experiment with more aerosols. Likewise, consistent behavior was found in the difference of longwave radiation reaching the ground below clouds (average 0.47% increase) as well as top of the atmosphere outgoing longwave radiation (average 0.11% decrease) although not shown.

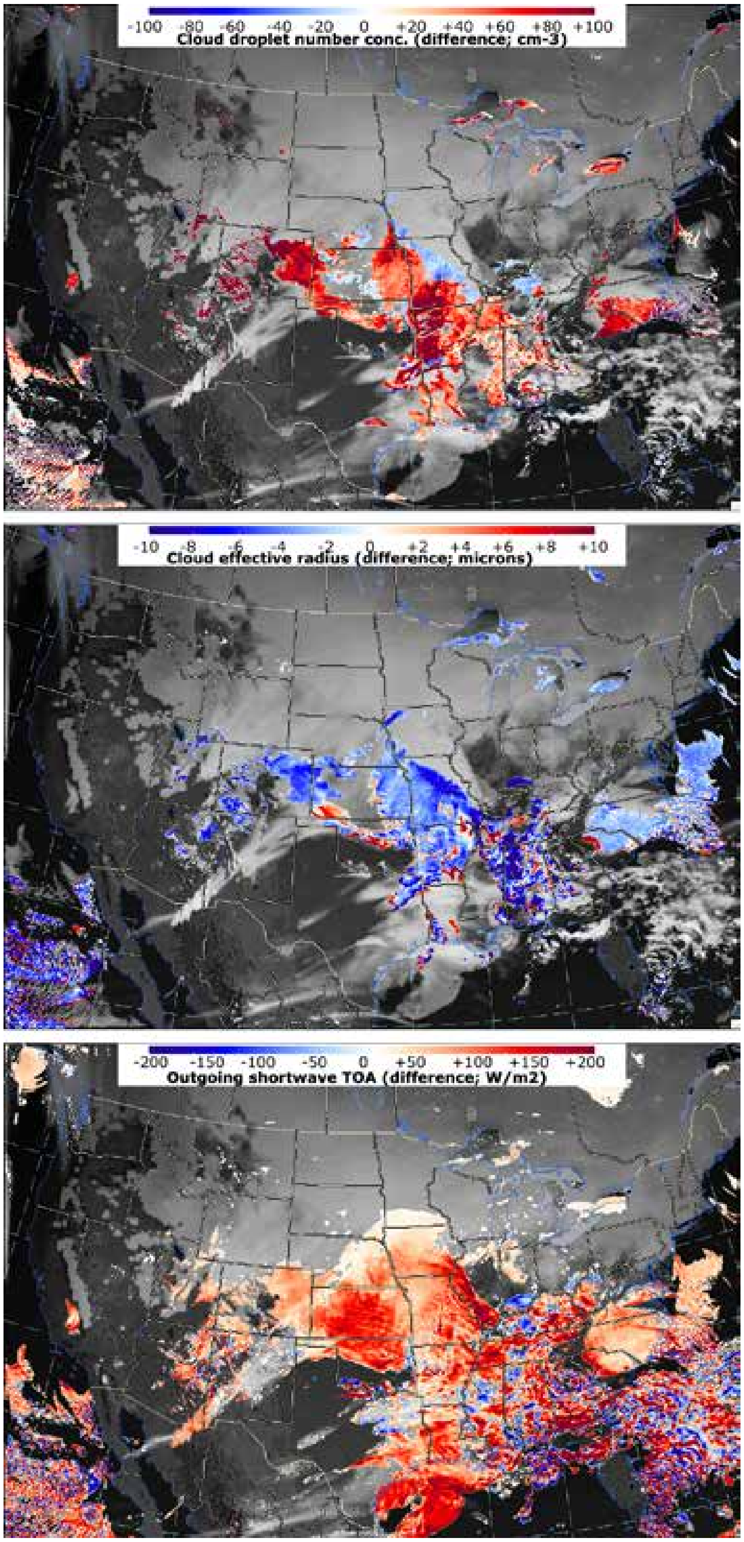

FIG. 2.5: WRF 18-h forecast valid 1800 UTC 31 Jan 2011 showing difference of cloud droplet number concentration (cm^{-3}) at approximately 1600 m above ground over Kansas (top panel), difference in mean effective radius of cloud droplets (microns) at the same level (middle panel), and difference of outgoing shortwave radiation (W/m^{-2}) at the top of the atmosphere (bottom panel) between ***Control*** and ***Clean*** aerosol experiment.

2.4.4 Water droplet distribution changes

It is difficult to encapsulate all of the changes to water droplet sizes and amounts for a series of simulations with millions of spatial grid points over 72 hours, but we believe the next set of three figures best illustrates the changes to water droplet distributions as aerosol number concentrations were changed. In Figs 2.6-2.8, we plotted a random sampling of points containing any liquid water, either cloud droplet or rain, in terms of their median volume diameter (MVD) versus liquid water content (LWC). On the left portion of each figure, cloud droplets are shown with a linear MVD scale, while points with rain are shown using a logarithmic scale on the X-axis. Each dot is color coded by temperature with gray dots for any temperature value above 0°C, then red, orange, green, and blue dots for each ten degree increment below zero. This color coding provides insights into possible changes to size as well as frequency of finding water drops in specific temperature ranges in the mixed phase region as aerosols were changed in the various experiments. In addition, the solid black lines on the left portion of Figs. 2.6-2.8 represent the results of the benchmark simulations, Nc50 and Nc750, while we omit the rain drops because they are

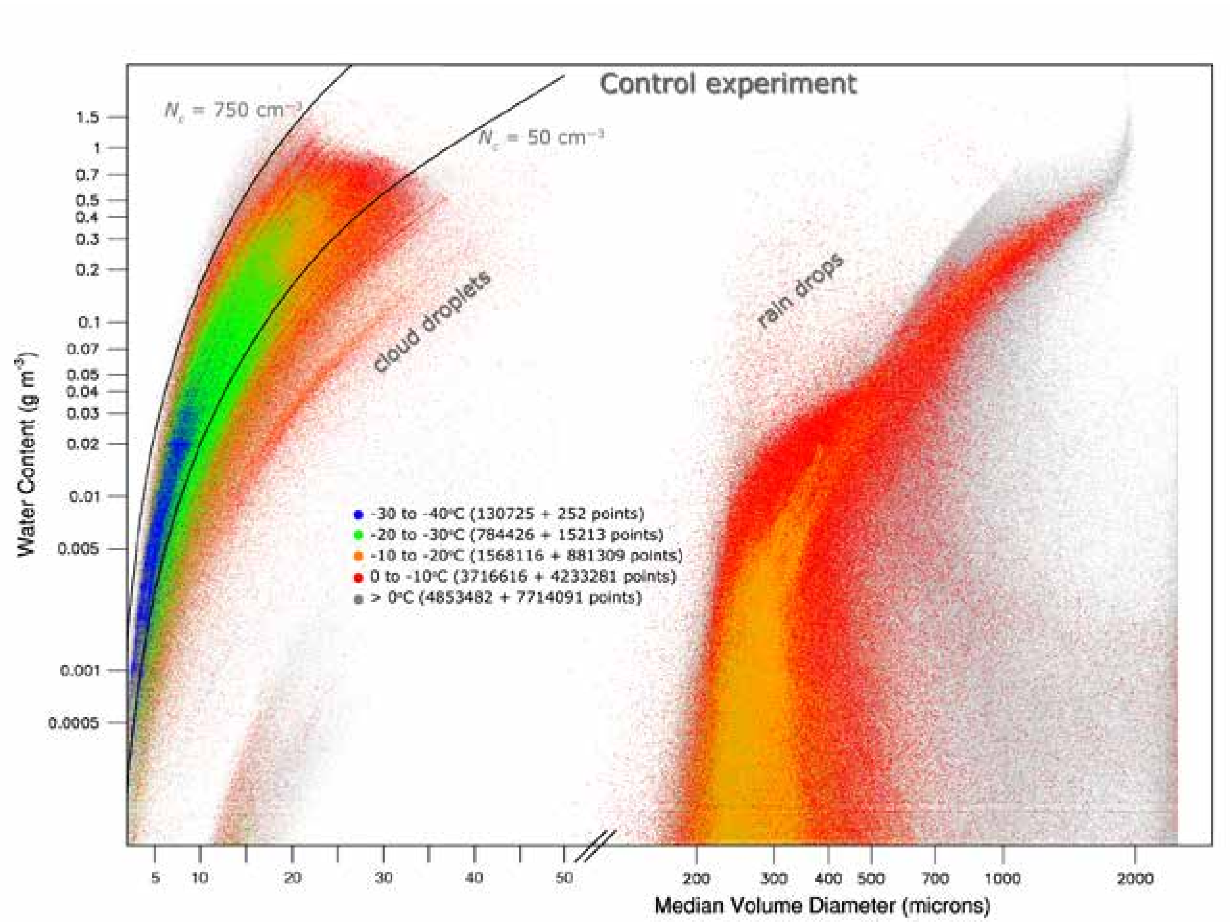

FIG. 2.6: Random sample of WRF grid points from the ***Control*** aerosol sensitivity experiment with cloud water (left) or rain (right) plotted as a function of median volume diameter (MVD), liquid water content (LWC), and tempreature (color coded: gray dots indicate T>0C, red, orange, green, and blue dots represent each consecutive 10°C lower, respectively. Note the logarithmic Y-axis scale and combined linear (cloud droplets) to logarithmic (rain) scale on X-axis.

redundant with those found in the other two figures. Nc50 and Nc750 collapse to a single line because a constant number concentration of droplets gives only one value of MVD for any particular LWC using the simple mass-diameter power-law relation of $m(D) = aD^b$.

Note in Fig. 2.6, created from the Control simulation, that nearly all points containing cloud water lie within the bounds of the benchmark simulations and note how the highest LWC and largest MVD correspond to the highest temperatures. Also note how the number of grid points of cloud water decreases sharply with decreasing temperature, which we would expect since liquid water more likely freezes as temperature decreases and larger drops freeze before smaller drops in general (Bigg, 1953). Where the MVD of rain is relatively small, the corresponding LWC is small, and the preponderance of these points were produced via collision-coalescence process and subsequent accretion of other cloud droplets in the warm-rain process, while the narrowing diagonal region into higher LWC and larger MVD dominantly represents grid points of rain produced from melting ice, which would be expected to be larger.

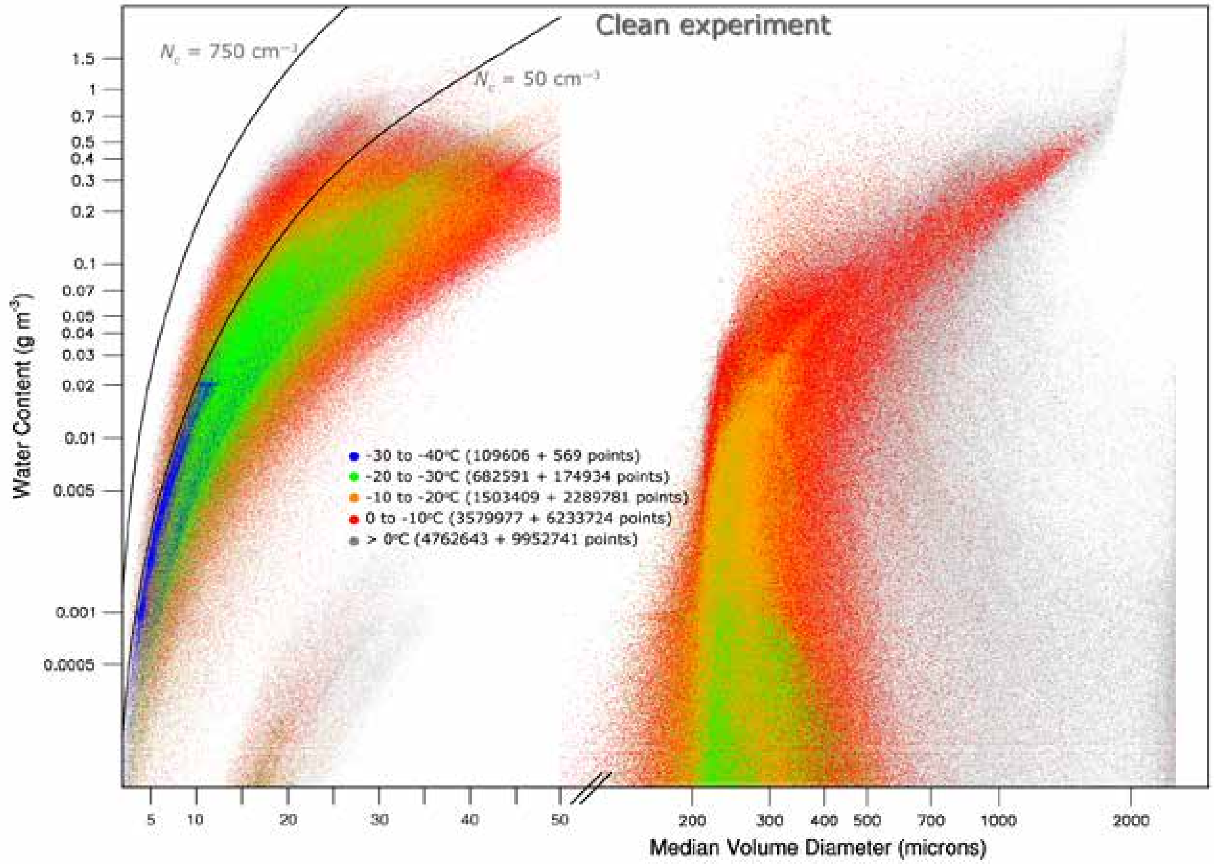

FIG. 2.7: Same as Fig. 2.6 except from the ***Clean*** aerosol sensitivity experiment.

Then, to see alterations to water distributions with the decreased aerosol number concentration in the Clean experiment, refer to Fig. 2.7 and note how the distribution of cloud droplets significantly shifts to the right side of the Nc50 line indicating a notable increase of MVD and corresponding decrease in droplet number. Also note the upper extent of LWC as the larger mean size of water leads to more rapid rain production by enhancing the warm-rain processes, which is easily confirmed by the indicated number of rain points at all temperatures. In fact, a factor of ten more grid points with rain between -20 and -30°C (green dots) appears along with a factor of four increase between -10 and -20°C (orange dots) when reducing aerosols by a factor of ten between Control and Clean. Note the larger Y-axis vertical extent of LWC (rain) by colored dots between 200 and 400 μm in Fig. 2.7 compared to Fig. 2.6. A more subtle feature appears in the narrow diagonal region of rain with higher LWC and larger MVD as relatively fewer grid points appear in this region in the Clean experiment as compared to the Control experiment. We will refer to this narrowing region towards the upper-right of these graphics as the "flame tip" and provide a physical connec-

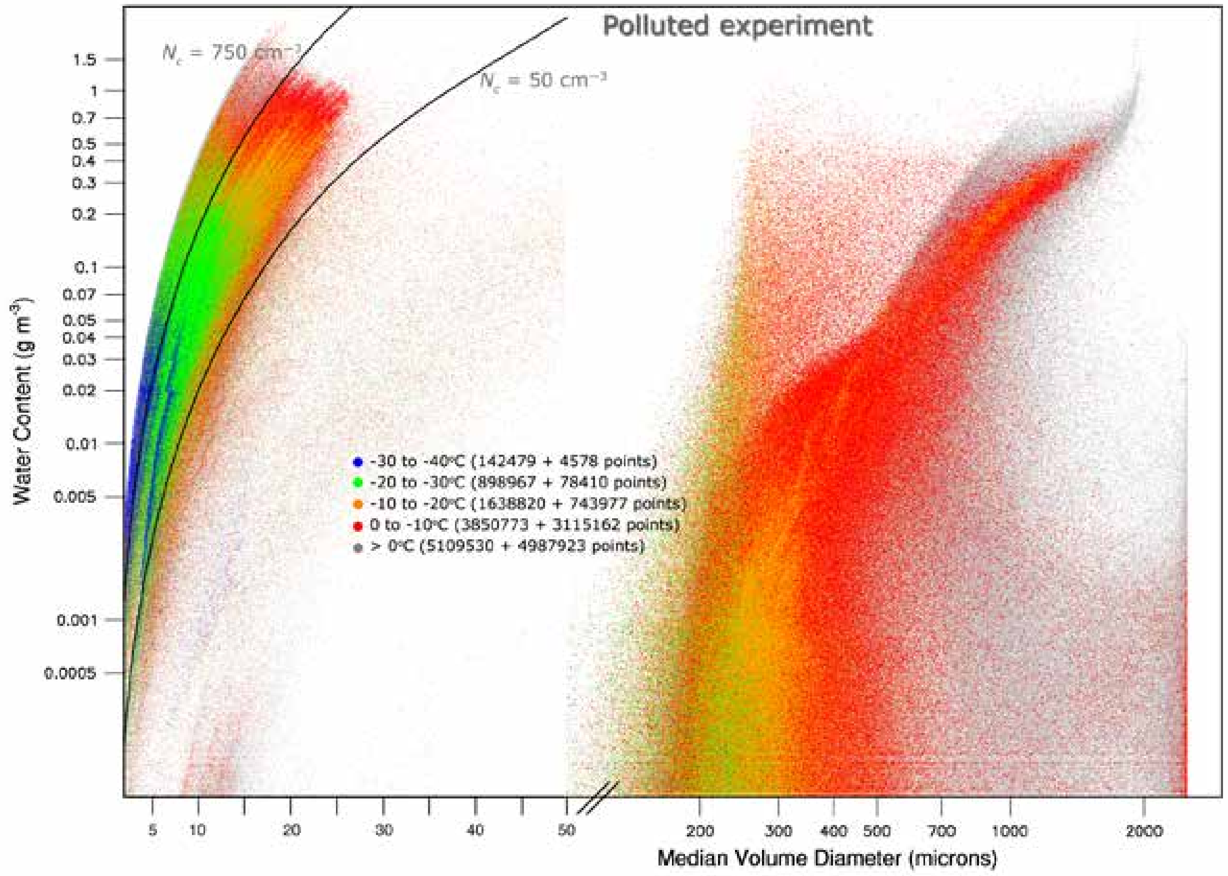

Fig. 2.8: Same as Fig. 2.6 except from the ***Polluted*** aerosol sensitivity experiment.

tion for differences seen between Figs. 2.6-2.8 in the next subsection.

In the final sensitivity experiment, Polluted, in which the aerosols were increased by a factor of ten more than Control, the most notable change of Fig. 2.8 is the dramatic shift of grid points with cloud water towards much smaller MVD and slightly higher LWC. This makes physical sense since the increased aerosol concentration is leading to smaller overall mean size of cloud water that subsequently hinders the warm-rain processes. There are also more cloud droplets surviving to lower temperatures due to their lower likelihood of freezing as their mean size decreases.

2.4.5 Precipitation impacts

The changes to water droplet populations by changing aerosols definitely resulted in changes to surface precipitation, but not in entirely obvious ways. Fig. 2.9 shows the individual differences of rain, snow, and graupel amounts for the second day of the simulation between the Control and Clean experiments. Table 2.2

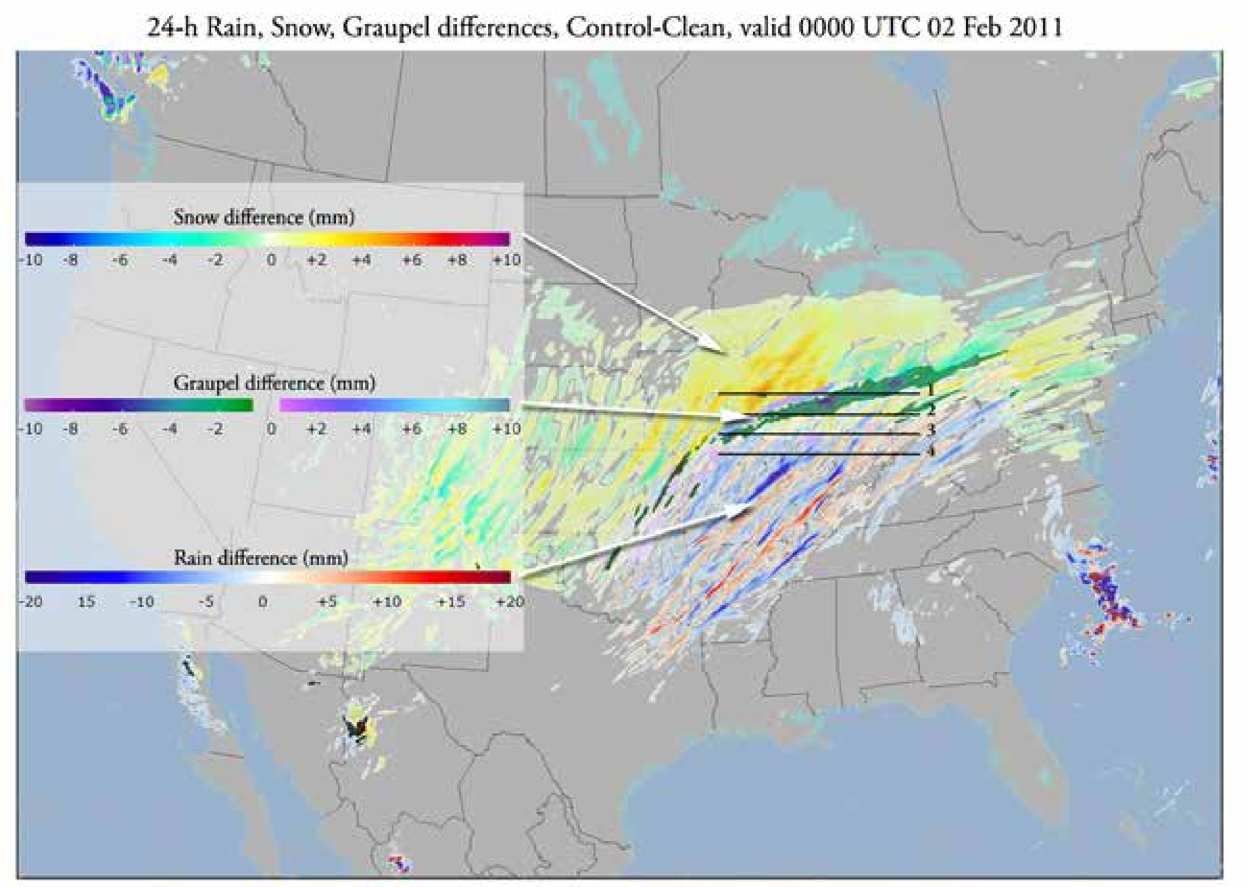

Fig. 2.9: Individual rain, snow, and graupel precipitation amount differences (mm) for 24-h period ending 0000 UTC 02 Feb 2011 between the ***Control*** and ***Clean*** sensitivity experiments. Four, numbered horizontal lines represent cross-sections for horizontal water flux analysis shown in the next figure.

also contains precipitation amounts by type from all the experiments along with various differences and percentage change between high and low aerosol concentration experiments. Other time periods (not shown) confirmed similar patterns. Overall, there are mixed signals of both increased and reduced rain and snow amounts due to evolution and location differences of narrow precipitation bands; however, the primary signals were a reduction of rain in the southeast portion and an increase of snow in the northern portion as aerosols were increased. The reduction of rain seems logical since the warm-rain processes were hindered by overall smaller droplets (Albrecht, 1989), but the very widespread and obvious increase of snow with higher aerosol concentration was not expected.

TABLE 2.2: Total rain, snow, and graupel surface precipitation amounts in the region between the Rocky Mountains and eastern USA coastline for 24-h ending 0000 UTC 02Feb2013 (day2) from series of WRF sensitivity experiments. Percentage change values in difference columns are [(*A*-*B*)/*B*] whereas parenthesized percentage values are [(*A*-*B*)/*Total*].

Experiment	Nc50 (mm)	Nc750 (mm)	Control (mm)	Clean (mm)	Polluted (mm)	Difference Nc750-Nc50	Difference polluted - clean	Difference Polluted-Control	Difference Control-Clean
Rain	769K	726K	751K	797K	730K	-43K -5.6% (-2.8%)	-67K -8.9% (-4.3%)	-22K -2.9% (-1.4%)	-45K -5.7% (-2.9%)
Snow	735K	774K	748K	707K	763K	39K +5.3% (+2.5%)	56K +8.0% (+3.6%)	16K +2.1% (+1.0%)	41K +5.8% (+2.6%)
Graupel	59K	49K	61K	65K	58K	-10K -16.9% (-0.6%)	-6.6K -10.3% (-0.4%)	-3.4K -5.5% (-0.2%)	-3.3K -5.1% (-0.2%)
Total	1564K	1549K	1560K	1568K	1551K	-25K (-0.9%)	-17K (-1.1%)	-9.6K (-0.6%)	-7.8K (-0.5%)

We believe that the increase in snow was due to the generally reduced warm-rain processes in the southern U.S. permitting many more cloud droplets, albeit smaller, to be transported northward (and possibly lofted higher) into the snow-producing clouds found to the north. While the overall mean size of droplets may have been smaller when aerosols were more numerous, the geometric sweep-out of those droplets increases because there were so many more droplets to intercept as well as larger LWC even though there was a general decrease in collision efficiency (Hindman et al. 1992) between snow and cloud water. This was confirmed by calculating the horizontal flux of cloud water crossing through four parallel WRF X-Z (west-east) grid planes during four 6-h time periods on day 2. Note in Fig. 2.10 how the flux of water was largest through each plane and for each 6-h interval in the simulations with the highest aerosol concentration, and the flux was percentage-wise larger in the X-Z planes to the south and smaller to the north. An additional contribution to the increase of snow in the north was also possible from an enhanced Wegener–Bergeron–Findeisen process as some of the cloud droplets could have evaporated to vapor that subsequently migrated to the ice and snow; however, individual process rates were not captured during the model simulations to confirm this hypothesis.

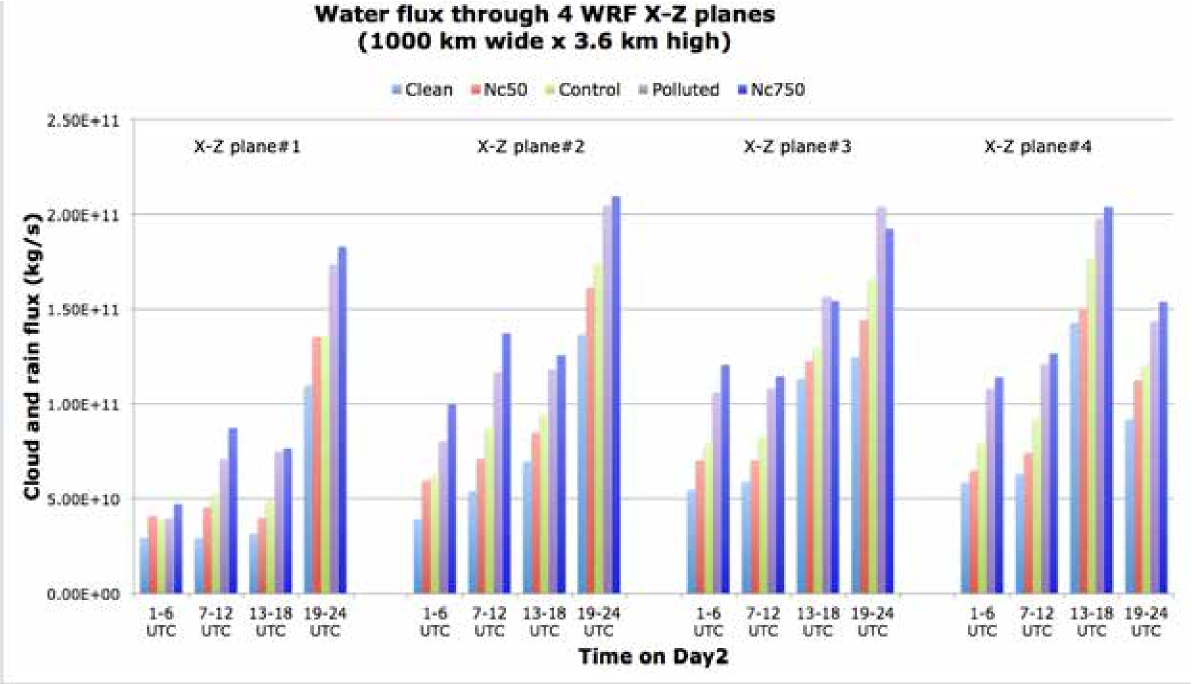

FIG. 2.10: Horizontal water flux through 4 WRF X-Z planes (1000 km wide from 0.5 to 4.0 km height) shown in preceeding figure during four 6-h intervals on the second simulation day for each of the sensitivity experiment.

Further evidence and confirmation that rain and graupel generally decreased while snow increased when aerosols were increased is provided in Fig. 2.11. Differences of individual rain, snow, and graupel precipitation amounts between experiments with higher aerosol concentration minus experiments with lower aerosol concentrations are shown for each day as well as the sum of all three days. The largest decrease in rain and corresponding increase in snow occurs between the experiments with the greatest difference of aerosol concentration (Polluted minus Clean). Comparisons between experiments with less drastic aerosol change produced less drastic precipitation differences showing consistent and robust behavior of the aerosol effects. Furthermore, the decrease in rain amount exceeded the increase in snow and differences of graupel were quite small, but also consistently less graupel with increasing aerosols. We speculate that this was due to the overall reduction in number of points with rain and overall smaller droplet size that hindered freezing of rain drops into graupel particles in this scheme.

While the amount of rain reaching the surface decreased with higher aerosol concentrations, the most common reductions occurred primarily in association with extremely light precipitation. Fig. 2.12 shows distributions of rain, snow, and graupel in precipitation bins of varying amounts for each hour of the 72-h simulation. Whereas the count of grid points with hourly rain went down as aerosols increased, there was hardly any noticeable change in counts of hourly amounts greater than 2.5 mm over entire synoptic storm scale regions. Similarly, decreases in the amount and frequency of light rain but not heavier rain was noted in relation to significant increases of aerosol concentration in an observational and modeling study over eastern China by Qian et al. (2009). Also, Sorooshian et al. (2010) found much greater impact of aerosols to light precipitation in contrast to heavier precipitation and attributed it to cloud thickness property since

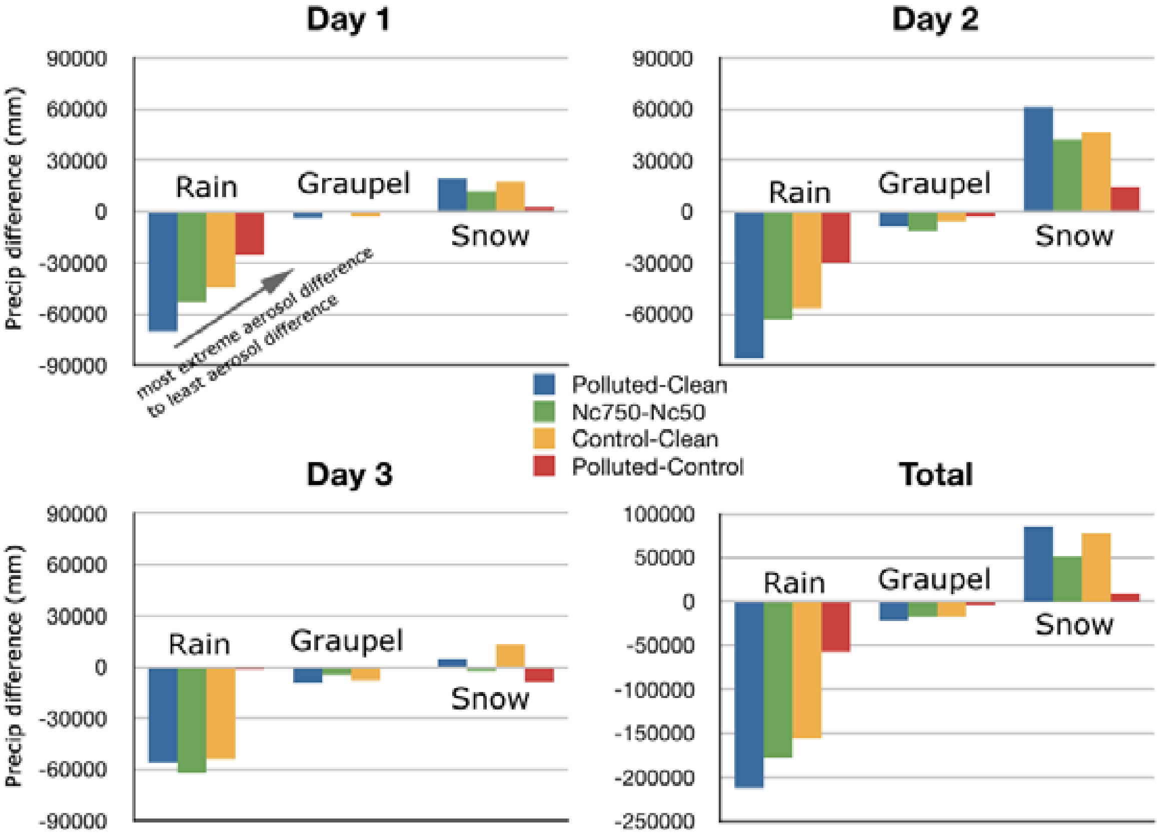

FIG. 2.11: Individual rain, snow, and graupel precipitation amount differences (mm) for each 24-h period during the three day period and total for all days created by summing over any grid box between various sensitivity experiments, but always subtracting an experiment with higher aerosol number concentration from an experiment with lower concentration as shown by the key.

deep clouds offer plenty of opportunity for rain to accrete cloud droplets over a large cloud depth as compared to relatively thin clouds.

As mentioned in the previous subsection, there was another change to the mixed-phase precipitation region worthy of mention, although more subtle than the preceding noted effects. The “flame tip” region shown in Figs. 2.6-2.8 shows a decrease in grid points with relatively high LWC and large MVD in Clean (Fig. 2.7) as compared to Control (Fig. 2.6) with lesser differences seen between Control and Polluted (Fig. 2.8). The scattering of points oriented vertically along MVD = 300 μm was dominantly produced by warm-rain processes whereas gray dots (T > 0°C) towards the flame tip were dominantly produced by melting snow/graupel. Consistent with the snow increase due to aerosol increase found in the region north of the warm front (Fig. 2.9), which was dominated by glaciated clouds filled with snow, it appears that increasing aerosols increased the overall

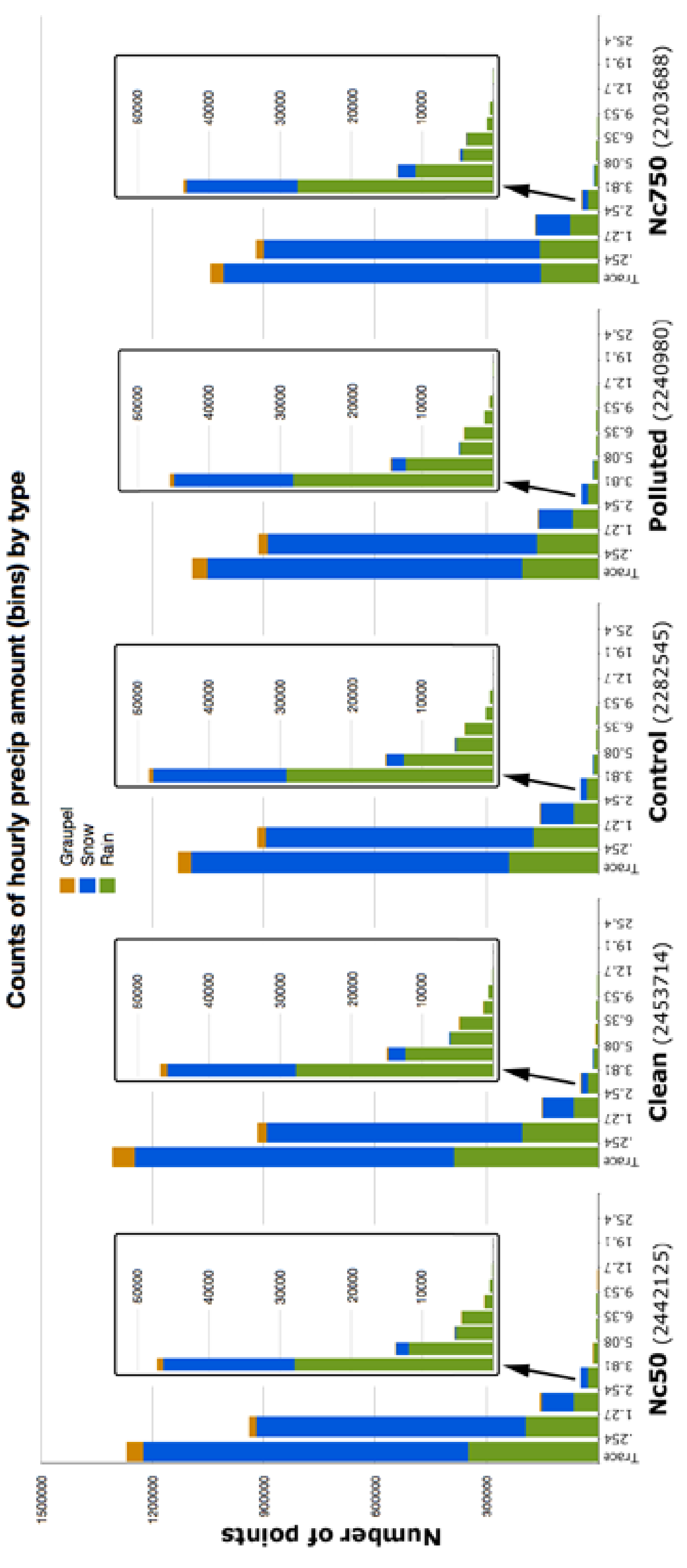

Fig. 2.12: A count of hourly rain (green), snow (blue), and graupel (gold) precipitation amounts in amount bins [Trace, 0.254, 1.27, 2.54, 3.81, 5.08, 6.35, 9.525, 12.7, 19.05, 25.4 mm; each X-axis in inches as in original repors] over full 72 hour simulation for each of the sensitivity experiments.

size/mass of snow aloft that subsequently melted into rain before reaching the surface; however, Fig. 2.11 showed that the additional melted ice does not compensate for the loss of rain by warm-rain processes.

Another interesting aerosol effect in regions of mixed-phase surface precipitation is noted in Fig. 2.13. For any model grid point containing a mixture of rain and snow/graupel during an hour we computed the fraction of liquid precipitation as rain/(rain+snow+graupel) and counted each 10% bin. After normalizing by the number of grid points with any precipitation, we found that as aerosols increased, there was a relatively higher fraction of liquid precipitation. One potential hypothesis for this effect is corollary to the increased snow to the north of the warm front, which is that the less efficient rain production in the south allowed more cloud droplets to transport northward into the zone of mixed-phase region near the warm front where rain accreted more cloud droplets simply due to higher number of them, albeit smaller size, and resulted in a disproportionate increase in rain reaching the ground compared to graupel/snow. This hypothesis is supported by similar results seen in Igel et al. (2013) where they attributed slightly higher surface precipitation amounts approximately 150 km north of the warm front to higher rates of rain accreting cloud droplets.

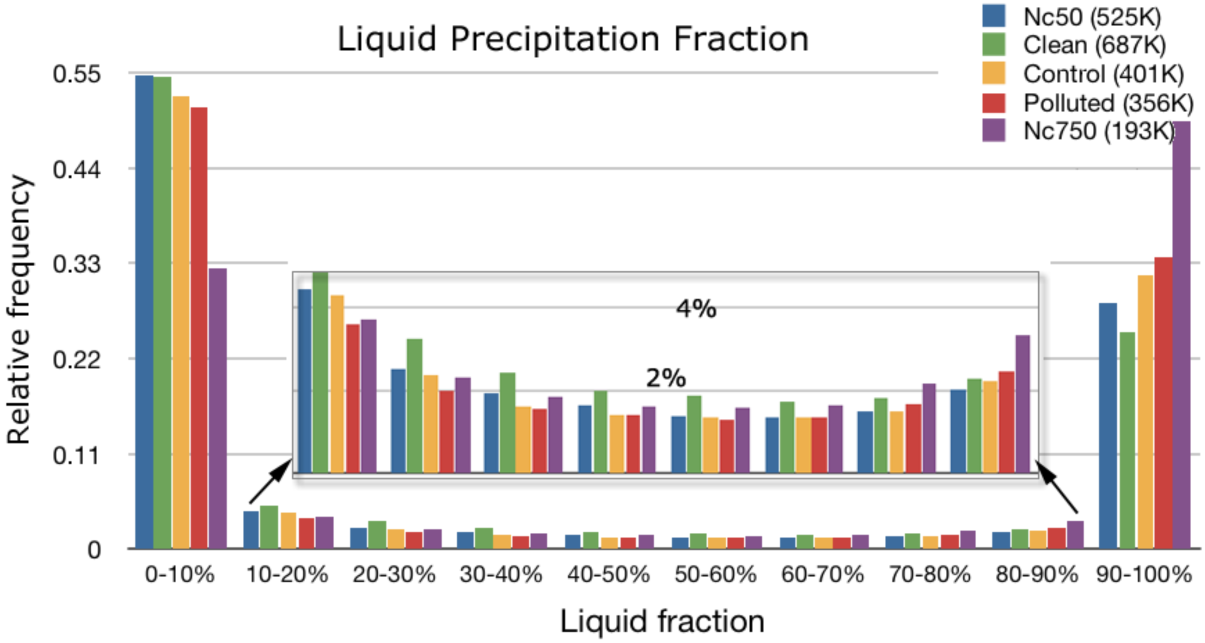

Fig. 2.13: Relative count of 10-percent bins of liquid to total precipitation fraction from hourly data for the full 72 hour simulation for each of the sensitivity experiments. The total count of points with any surface precipitation is given in parenthesis in the color legend.

A final aspect of precipitation was analyzed to determine if using a simpler microphysics scheme without aerosols and constant cloud droplet concentration or the new scheme with low, moderate, or high aerosol concentration produced any improvement as compared to observations. Unfortunately, errors in precipitation observations (Rasmussen et al. 2012) and errors in the model forecast at single sites (even a thousand sites with precipitation during a large-scale winter storm) far outweigh the scale or magnitude of changes seen in our five sensitivity experiments. Fig. 2.14 illustrates that model forecast errors were rather large and extremely variable and each experiment produced very similar error statistics. In fact, our results indicate no statistically-significant differences among the five experiments as evidenced by the overlapping means and confidence intervals shown in Fig. 2.14. And, since the fidelity of observed snow water equivalent data in automated precipitation measurements, especially during moderate to high winds, lacks credibility, we excluded most snow reports from the data used to create Fig. 2.14. As examples of the measurement problem: Quincy, IL reported 559 mm of snow yet only 2 mm liquid equivalent; Moline, IL reported 467 mm of snow with 4 mm liquid equivalent; Chicago-Midway airport reported 457 mm of snow with only 5 mm of liquid yet Chicago-O'Hare airport reported 508 mm of snow and 41 mm liquid equivalent. Massive errors such as these are rampant in automated reporting stations during snowstorms in recent decades and evaluators of model forecasts should remember to question observational data quality when assessing model performance. A massive number of the deep blue dots in Fig. 2.4 representing serious model over-forecasts of precipitation are likely to be far lower error than it superficially appears. Regardless, when we exclude measurements that likely coincided with snow, we did find that our WRF simulation produced a noticeable bias of under-forecasting the highest precipitation amounts, indicating frequently-

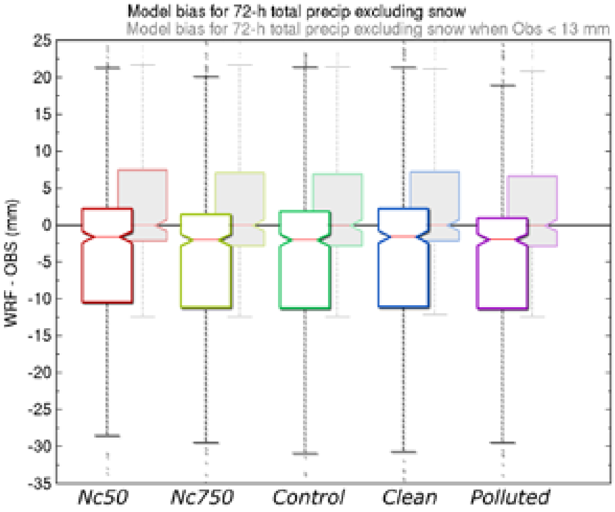

Fig. 2.14: Model bias of 72-h total precipitation, excluding locations reporting snow due to large undercertainties with water equivalent amount from the five WRF model sensitivity experiments. Dark boxes represent all precipitation observation locations (except snow) while the gray-shaded, lightly-outlined boxes are model bias for amounts less than 13 mm

missed convective events combined with near zero mean bias of light precipitation (amount less than 13 mm over 72 hours) with a slight model over-forecast problem for the light amounts.

To emphasize a main point about aerosols affecting precipitation amounts, even though aerosols changed the water size distributions as dramatically as seen in Figs. 2.6-2.8, which subsequently affected at least six microphysical processes: autoconversion, collection of cloud water by rain, snow, and graupel, freezing of cloud water and rain, the accumulation of all these processes remained negligible as compared to combined errors in observations and model precipitation forecasts. Perhaps the only way to know for certain if the more complex physics with more realistic spatial and vertical distributions of aerosols improves forecasts of precipitation is to perform far longer integrations over months, seasons, or years.

2.5 Conclusions

To address a complex and uncertain research problem that affects storms from convective to synoptic scales, the Thompson et al. (2008) bulk microphysics scheme was updated to incorporate aerosols explicitly. The scheme nucleates water and ice from their dominant respective nuclei and fully tracks and predicts the number of available aerosols. Using the Weather Research and Forecasting (WRF) model, the scheme was tested in a high resolution (4-km spacing) simulation of a three-day winter storm event over the entire contiguous U.S. A control simulation with climatological aerosol conditions and two sensitivity experiments with clean (one-tenth) and polluted (ten times) conditions were used to evaluate the magnitude of various aerosol-cloud-precipitation interactions. Additional experiments that ignored aerosols and used the older, 1-moment cloud water prediction combined with constant (in space and time) high and low droplet number concentration revealed entirely consistent behavior with the aerosol-included experiments and gives credence to robustness of results and physics of the scheme.

There were numerous notable and fundamental changes to water droplet size distributions and subsequent precipitation and radiation impacts from varying aerosol number concentration that were consistent with expected aerosol indirect effects. Increasing aerosol concentration produced consistently more droplets of overall smaller size that hindered the warm-rain processes (Albrecht, 1989) and increased cloud albedo (Twomey, 1974). When comparing the Control vs. Clean experiments, the cloud albedo increased by 5.4% in the experiment with the higher aerosol concentration. Differences in longwave radiation reaching the ground due to cloud property changes were more subdued, as expected, increasing only 0.47% while outgoing longwave radiation to space decreased even less, -0.11%, due to cloud opacity changes by the different aerosol concentrations affecting droplets and ice crystal sizes.

Space and time-integrated surface precipitation differences between experiments with more or fewer aerosols revealed rather modest effects overall (3-8% reduction of rain, 2-5% increase of snow) for this 72-h winter cyclone simulation. Findings in Section 2.4.5 were consistent with a study by Igel et al. (2013) in which the precipitation amount in the immediate vicinity of a synoptic-scale warm front decreased slightly whereas amounts north of the warm front increased. This was due to higher cloud droplet number concentration and LWC being transported northward as aerosol concentration increased and subsequent capture by falling snow and rain increased due to higher available LWC even though collisions efficiencies reduced due to smaller overall droplet size. This may have broad and important implications for overall water transport being affected by aerosols and provide shifts in precipitation patterns on a continental scale.

Although clear from Fig. 2.9 that very specific locations may have changed precipitation amounts more drastically, most of the changed rain regions involved shifts in location while the amounts nearly offset, especially in moderate to high precipitation bands, since Fig. 2.12 showed that only the lightest amounts of precipitation showed high susceptibility to aerosol changes. Therefore, we speculate, that if we simulated an entire season's worth (similar to Seifert et al. 2012) of real weather across an entire continent, most of the location shifts in precipitation due to different aerosol conditions would be likely to smear out with successive storms due to changing wind directions, convergence features, and dynamical interactions. The basic behavior of dominantly less rain and slightly more snow is a plausible outcome for numerous extratropical winter cyclones such as the one studied here, but we would expect only modest changes to surface precipitation from changing aerosol concentration when using reasonable estimates of typical aerosol concentrations and integrated over an entire season and a large region, especially considering our experiments used factors of ten above/below the typical values.

Clear from Fig. 2.14 is that there were no statistically-significant differences in the model's surface precipitation forecasts when using different aerosol conditions and comparing to observations. We point out the following difficulties in verifying model forecasts of surface precipitation to validate sensitivity experiments such as ours:

- errors in model cloud forecast timing and location may greatly outweigh differences among sensitivity experiments,
- observational uncertainty can be massive, particularly with liquid equivalent snow measurements in blowing snow conditions,
- sensitivity of aerosols to resulting precipitation is potentially weaker or stronger in models than what is truly found in nature but determining such a bias is exceedingly difficult.

Perhaps more important to validation efforts are the changes to water droplet distributions such as those illustrated by Figs 2.6–2.8 although insufficient aircraft data exists to perform an objective analysis. However, the general trend of cloud droplet concentrations shown in the Control simulation (Fig. 2.6) as compared to the Clean (Fig. 2.7) or Polluted (Fig. 2.8) experiments gives at least subjective positive comparison to previously published aircraft data (e.g., Cober and Isaac, 2012; Sand et al. 1984; Politovich and Bernstein, 2002).

While extensive research continues to focus on aerosol effects on surface precipitation, this study also shows explicitly how aerosols affect the water droplet size distribution aloft. This is an important consideration for any in-flight aircraft icing applications because the liquid water content and size of drops are critical to the accumulation of ice on airplane control surfaces (Arenberg, 1943). Therefore, using the data from these experiments, we performed relatively simple ice accretion calculations intended to predict aerosol effects on a final application to aircraft icing. The equations used for ice accretion on a standard cylinder followed Makkonen (2000) where the change in mass with time is a product of collision efficiency, LWC, velocity, and cross-sectional area of the cylinder (details found in Appendix 1). Using the WRF simulation data, we calculated a dM/dt value for any model grid point with either cloud water or rain at temperatures below 0°C each hour from 6 to 72 h from all five sensitivity experiments. Next, we calculated the frequency of occurrence of each order of magnitude bin of ice accretion rate, shown in Fig. 2.15. The figure shows that as aerosols were increased, there was generally an increase in ice accretion by cloud water (left panel) up until the largest ice accretion rate when the trend reversed direction. In contrast to the smaller cloud droplets, the effect of increasing aerosols generally reduced the ice accretion from larger rain drops (right panel) except in the highest category of ice accretion. These appear to be logical because an increase in aerosol concentration led to more numerous (but smaller) cloud water droplet number concentrations with higher LWC because of the hindered warm-rain production. The increase in LWC overcompensated for the decrease in cloud droplet size since collision efficiency of droplets decreases as droplet size decreases since the smallest droplets pass around a moving object and follow the airstream rather than impinge on the surface of the cylinder/wing. The general decrease in frequency of ice accretion due to rain as aerosols increase follows from the decrease in grid points with rain as aerosols increased due to the reduced warm-rain processes. The increased frequency of small droplet icing may imply that more "rime" icing may occur as aerosols are increased while the frequency of "clear/glaze" icing may decrease if aerosols are increased.

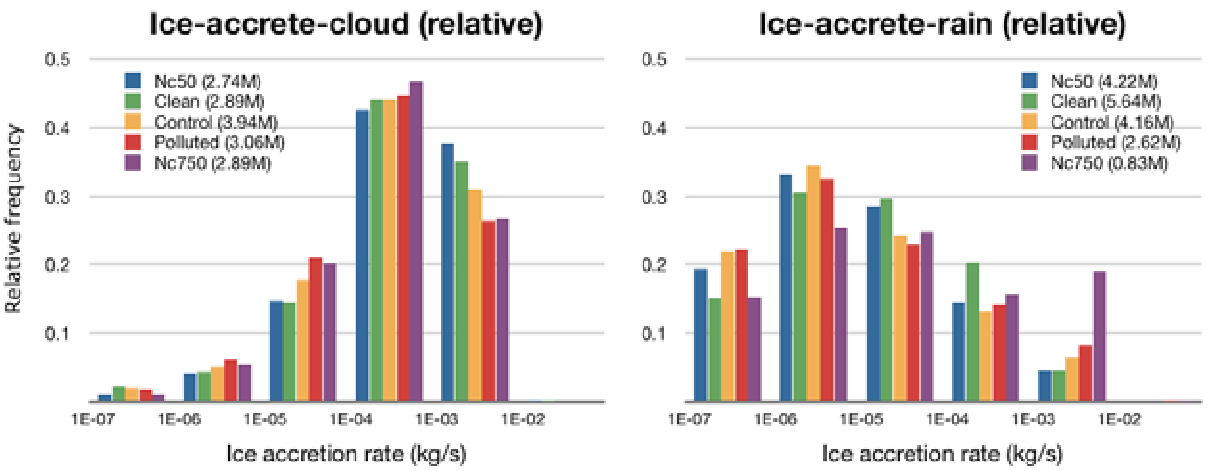

FIG. 2.15: Relative frequency of occurence of ice accretion rates (mass per unit time, kg s^{-1}) shown for each order of magnitude accretion rate due to supercooled cloud liquid water (left) and rain (right) for each of the sensitivity experiments (colored bars).

A natural extension of this study would be to run a series of similar sensitivity experiments for multiple months, seasons, and years to capture the breadth of precipitation systems across most of a continent and study the resulting changes in *regional* precipitation, especially in water-sensitive areas of the western U.S. Also this study did not break down various mesoscale forcing mechanisms such as orographic forced snow (or rain), lake effect, sea-breeze areas, or strong convective regions to investigate aerosol effects on more localized precipitation, but the foundation for these tests was demonstrated. Additionally, we believe this scheme is well-suited to simulate long duration convective events including typical non-severe shallow convection along with deep convective squall lines, supercells, and MCSs, since all inherently-linked dynamics and feedbacks are present in this type of configuration using a well-established convection-permitting model (WRF). Such simulations could be used to validate many claims of aerosol invigoration of shallow and deep convection (c.f., Li et al. 2011; Tao et al. 2012) and perhaps reveal if aerosols effects are *causing* specific responses in convection or are simply *correlated* with various convective weather situations (Morrison and Grabowski, 2011, 2013).

2.6 Acknowledgements

The authors wish to thank David Gill and Jim Dudhia for their advice and support of various WRF code modifications. Alison D. Nugent, Roy Rasmussen, and Hugh Morrison are gratefully acknowledged for their discussions that ultimately improved this work, and Kyoko Ikeda is thanked for helping to create Fig. 2.14. This research is in response to requirements and funding by the Federal Aviation Administration. The views expressed are those of the authors and do not necessarily represent the official policy or position of the FAA.

3. Explicitly-Coupled Cloud Physics and Radiation Parameterizations and Subsequent Evaluation in WRF High-Resolution Convective Forecasts

This chapter is reprinted with permission from:

Thompson, G , M. Tewari, K. Ikeda, S. Tessendorf, C. Weeks, J. Otkin and F. Kong, 2016: Explicitly-coupled cloud physics and radiation parameterization and subsequent evaluation in WRF high-resolution convective forecasts. Atmos. Res., 168, 92–104.

3.0 Abstract

The impacts of various assumptions of cloud properties represented within a numerical weather prediction model's radiation scheme are demonstrated. In one approach, the model assumed the radiative effective radii of cloud water, cloud ice, and snow were represented by values assigned a priori, whereas a second, "coupled" approach utilized known cloud particle assumptions in the microphysics scheme that evolved during the simulations to diagnose the radii explicitly. This led to differences in simulated infrared (IR) brightness temperatures, radiative fluxes through clouds, and resulting surface temperatures that ultimately affect model-predicted diurnally-driven convection. The combined approach of evaluating simulated versus observed IR brightness temperatures, radiation reaching the ground, and surface temperature forecasts revealed the root model biases better than evaluating any single variable. This study found that the Weather Research and Forecasting (WRF) model predicted less overall clouds than was observed, particularly in the mid-troposphere, but that properly connecting the assumptions of particle sizes in the microphysics scheme to the radiation scheme resulted in sensible cloud-radiation indirect effects and modest improvements in simulated IR brightness temperature, amount of solar radiation reaching the ground, and surface temperature.

3.1 Introduction

Radiation and cloud microphysics parameterizations are perhaps the most computationally demanding part of numerical weather prediction models. In the last few decades, a plethora of new schemes of each type has emerged with increasingly complex treatment (e.g., Stensrud, 2007) since computational power has greatly increased. Specialists in microphysics modeling have increased number of predicted species from only a single cloud water and ice species (i.e., mass mixing ratios) to more complex double-moment schemes with number concentration and/or additional ice species (Meyers et al, 1997; Morrison and Pinto, 2005; Milbrandt and Yau, 2005; Woods et al, 2007; Thompson et al. 2008; Morrison and Milbrandt, 2015). Simultaneously, radiative transfer modeling experts have introduced more complex band-by-band (wavelength) treatments (Mlawer et al. 1997) while accounting for more gaseous and aerosol species (ozone, CO_2, water vapor, dust, black carbon, sulfates, etc.). Even with more recent advances in radiation schemes, numerous studies indicate wide-ranging differences in clear-sky radiation (Fouquart et al. 1990; Boucher et al. 1998; Zamora et al. 2005) due to internal methods or complexity or species considered. Far greater uncertainties arise with treatments of clouds by various radiation schemes. Furthermore, as code creators of these seemingly separate parameterizations focus their specialization even further, the end result is often a disconnect between assumptions of water droplet size and ice crystal size and/or shape between the set of these two schemes (Stensrud, 2007).

In general, global climate models (GCMs) do not suffer from this gap of knowledge between the microphysics and radiation schemes, primarily because they were built with this requirement in mind for climate simulations/applications; however, the same situation is less common in mesoscale models such as the Weather Research and Forecasting (WRF) model (Skamarock and Klemp, 2008). The reason is primarily the incorporation of many choices of physical parameterizations that can be inter-connected with the fewest shared variables thus giving the most flexibility. The inclusion of properly computed radiative effective size of cloud water droplets is paramount when discussing climate impacts associated with aerosol indirect effects. Furthermore, the IPCC reports clearly reveal that the largest uncertainty in all climate model simulations continues to be the aerosol indirect effects. The various IPCC climate models account for the physical principle that a cloud populated with a large number of small droplets has a higher shortwave reflectance (albedo) than the same liquid water content cloud composed of fewer but larger droplets (Twomey, 1979). While this principle is widely known and accounted for in various radiation parameterizations, the explicit connection between a cloud microphysics parameterization and its radiative effective size of water and ice species used by the radiation parameterization isn't assured in all models. As more and more non-GCMs (i.e., WRF) are increasingly used in regional climate modeling applications, an effort to connect assumptions made by different code authors of separate physical parameterizations will be required for proper application to climate-scale problems.

Visible and infrared satellite images together with example WRF-model forecasts of shortwave radiation reaching the ground near mid-day are shown in Fig. 3.1 and illustrate how WRF's implementation of the Geophysical Fluid Dynamics Laboratory (GFDL) radiation scheme treats clouds[*] as compared to the Rapid Radiative Transfer Model-Global (RRTMG) scheme. Note the extensive areas of reduced

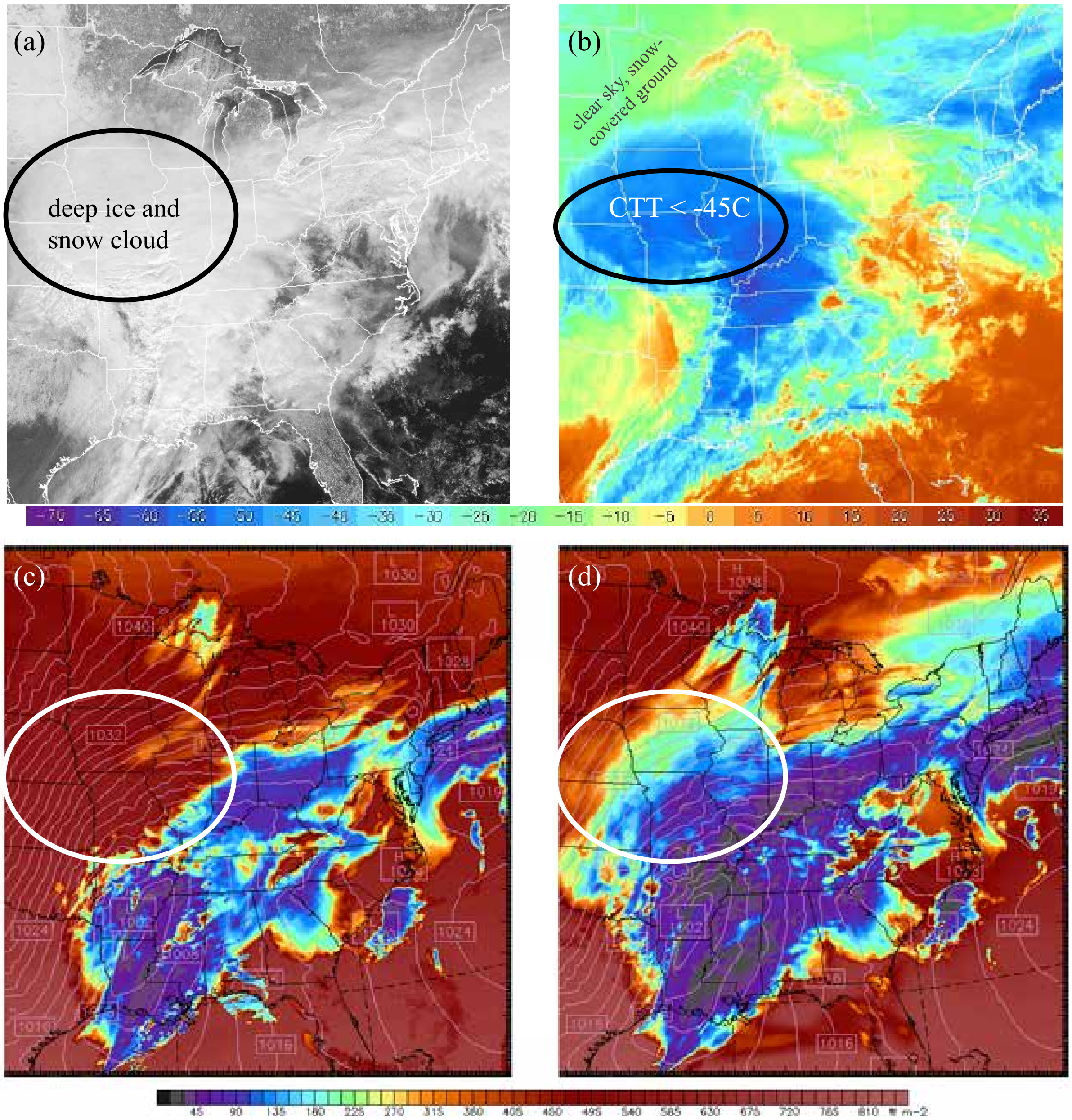

Fig. 3.1: GOES-13 visible (a) and infrared (b) satellite images at 17:45 UTC 01 Feb 2011 and sample WRF-model forecasts of shortwave radiation reaching the ground using the GFDL radiation scheme (c) and RRTMG scheme (d). In the version of GFDL radiation implemented into WRF the snow variable was ignored whereas RRTMG considers this species when computing radiation.

radiation reaching the surface in RRTMG as compared to GFDL. This occurred because the current implementation of the GFDL scheme in WRF includes only the cloud water and cloud ice variables while ignoring the snow variable when calculating radiative fluxes, whereas the current implementation of the RRTMG scheme includes snow in addition to these two variables. Meanwhile, in the model and in reality, it was snowing heavily at the time shown in Fig. 3.1 in Missouri and other nearby areas in both simulations containing equally deep and thick ice-phase clouds. This finding motivated us to explore the connections between these two radiation schemes (as implemented in the WRF model) and all hydrometeor species (cloud water, cloud ice, rain, snow, and graupel). Furthermore, we explored the various particle and size distribution assumptions that the microphysics scheme inherently uses and could communicate directly to the radiation scheme.

Prior work has evaluated the accuracy of simulated cloud fields in research and operational NWP models through comparisons of real and model-derived synthetic satellite observations (Karlsson 1996; Rikus 1997; Tselioudis and Jakob 2002; Lopez et al. 2003; Sun and Rikus 2004; Otkin et al. 2009). The model-to-satellite approach has been used to validate and improve the accuracy of cloud microphysics schemes (Grasso et al. 2014; Grasso and Greenwald 2004; Chaboureau and Pinty 2006; Otkin and Greenwald 2008; Grasso et al. 2010; Jankov et al. 2011). Synthetic satellite radiances derived from high-resolution NWP models have also been used as a proxy for future satellite sensors (Otkin et al. 2007; Grasso et al. 2008; Feltz et al. 2009) and have been shown to be a valuable forecast tool at convective scales (Bikos et al. 2012). Another example of the usage of the model-to-satellite approach is found in Cintineo et al. (2014) who showed a distinct lack of sufficient clouds with cloud-top temperature centered at about T = 260 K regardless of using four different microphysics schemes. This suggests the possibility that the model error is not related to cloud microphysics but rather other model errors. Another motivation of our research was to determine if assumptions with the radiation scheme or the proper coupling of effective size by the microphysics scheme together with the radiation scheme might be a possible cause of the reported error.

This paper is organized as follows: a description of the numerical experiments is found in the next section along with more detailed descriptions of the radiation scheme used and how specific alterations were implemented. Next, the results of ensemble experiments are presented in Section 3.3 highlighting the differences between coupled versus uncoupled cloud physics variables and radiation. Section 3.4 provides a more detailed inspection of example cloud areas to illustrate small-scale effects that are less obvious in the overall statistics. The final section contains a summary and conclusions.

3.2 Methodology

3.2.1 Numerical experiments

The simulations used in this study were performed with the Weather Research and Forecasting (WRF) model, version 3.4.1 with modifications discussed below. The WRF model includes many options to parameterize radiation, planetary boundary layer (PBL), microphysics, and land-surface processes and interactions. The University of Oklahoma's Center for Analysis and Prediction of Storms, OU-CAPS, has performed WRF-model ensembles for a number of recent years during six weeks in late Spring (e.g., Kong et al. 2014; Xue et al. 2010; Clark et al. 2012; 2015). In these simulations, the model was configured with 3 or 4 km horizontal grid spacing depending on which year and 51 vertical levels for a domain encompassing most of the continental U.S. To increase ensemble spread and to evaluate sensitivities due to physical parameterizations, each of the various members incorporated different PBL, radiation, and microphysics schemes, as well as different initial and lateral boundary data, and other variants. For the results discussed in this study, the ensemble members evaluated came from the 2013 Experimental Forecast Project, and all used the same PBL scheme referred to as Mellor-Yamada-Janic (Mellor and Yamada 1982, Janjic 2002), the Noah land-surface model (Chen and Dudhia 2001), the Thompson et al. (2008) bulk microphysics scheme and Rapid Radiative Transfer Model (RRTMG; Iacono et al. 2000) radiation scheme.

OU-CAPS ran WRF once daily from 23 Apr to 07 Jun 2013 starting each day at 0000 UTC and simulating for 48 hours, except over most weekends using the domain shown in Fig. 3.2. The initialization process included radar data assimilation to produce initial clouds, however, the results reported herein exclude the first six hours of forecast to avoid most issues related to model spin-up. Of the total 36 days with WRF model runs, all except two with corrupted model output files were used in subsequent analysis presented herein.

For the results shown later, the outer-most ring of 50 model points was ignored such that lateral boundary condition influences on the hydrometeors (cloud water, cloud ice, snow, rain, and graupel) would not profoundly influence the analyses. Under certain flow regimes and wind speed, eliminating only 50 points may be too few, but visual inspection of numerous model fields including individual hydrometeor species and synthetic satellite imagery deemed this number sufficient.

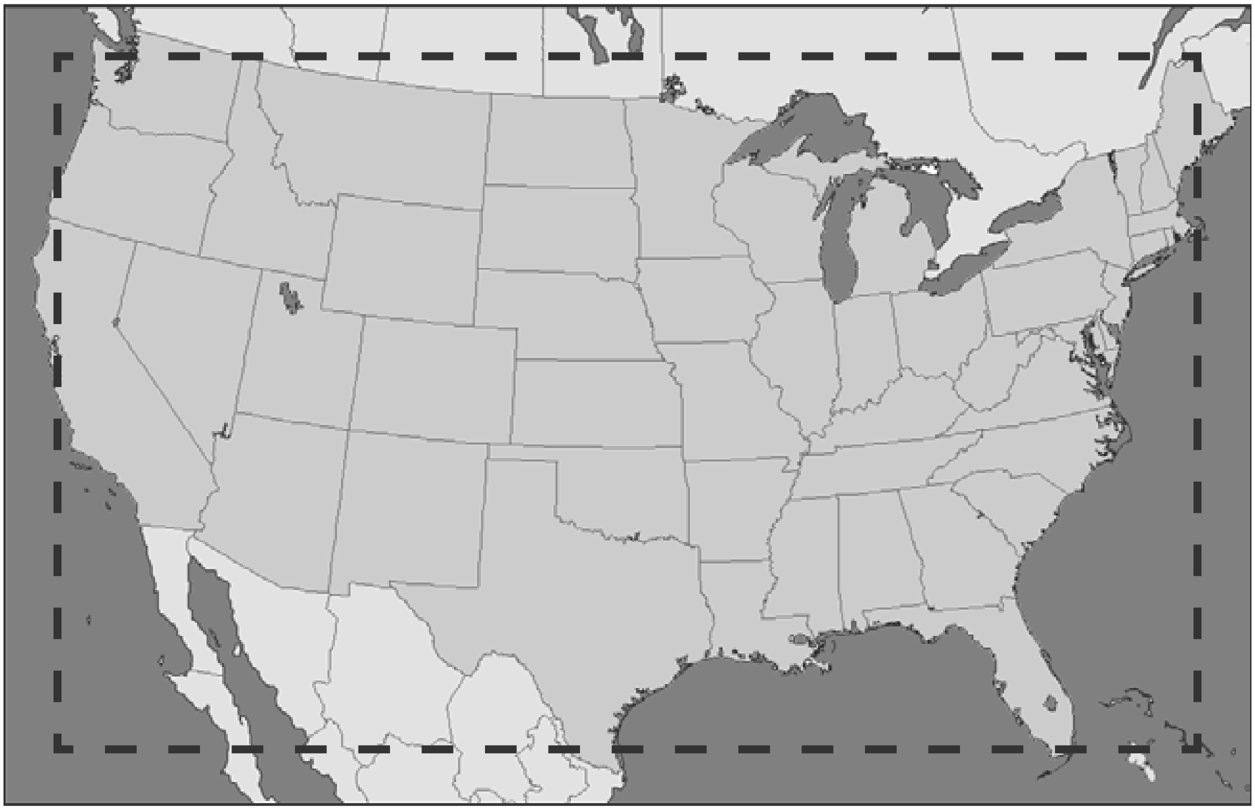

Fig. 3.2: The WRF model domain for 2013 OU-CAPS Spring Experimental Forecast with 1200 x 768 grid points spaced 4 km apart and 51 vertical levels. The dashed rectangle represents the outer 50 ring of points eliminated from analysis found in the Results subsection.

3.2.2 Radiation parameterization interface changes

The RRTMG scheme performs the radiative forward model calculations given clear or cloudy sky conditions as well as an option to treat aerosols, although this latter element was not enabled in these experiments. The existing WRF interface to RRTMG neglects partial cloudiness as nearly every grid box is considered completely cloudy if the microphysics parameterization contains explicit cloud hydrometeors or is considered entirely cloud-free if no such hydrometeors are predicted. RRTMG uses look-up tables to compute the absorbed, emitted, reflected, and transmitted components of broadband solar and longwave radiation within specific intervals (bins) of wavelength. The indexes of its internal look-up tables are wavelength and radiative effective radius of water droplets or ice crystals and resultant values of asymmetry parameter, single-scattering albedo, and cloud optical depth are used to compute radiative fluxes. Within the scheme the tables assume that water droplet radius ranges from 2.5 to 60.0 μm (Hu and Stamnes, 1993) and a population of randomly-oriented hexagonal ice crystals with radius between 2.0 and 140.0 μm (Fu et al. 1998). The interface code used between the WRF model and RRTMG strictly constrains the input sizes of water drops or ice crystals to these bounds.

The original RRTMG implementation into WRF used pre-determined values of cloud water and ice crystal size by default. While the version of the RRTMG scheme that gets activated when running the WRF-Chemistry model (Grell et al. 2005) contains direct calculations of water droplet sizes, although not ice size, the regular WRF code does not couple the droplet or crystal sizes with the particle size assumptions made by the grid-resolved microphysics scheme. The original v3.4.1 WRF implementation of the interface code for RRTMG assumes that cloud water droplets vary between 8 and 14 μm dependent upon temperature over land points and by modified relations over snow, sea ice, or open ocean. Similarly, the assumed ice crystal size in the WRF interface code is purely temperature dependent with values shown by Fig. 3.3. So, while a few microphysics schemes have mono disperse assumption of cloud water droplet spectra, some others have generalized gamma or inverse exponential assumption. As an example, the cloud droplet size distribution assumed in the Thompson et al. (2008) scheme has a variable gamma shape distribution that shifts according to the assumed droplet number concentration. Therefore the standard WRF code was modified in order to pass explicitly-computed radiative

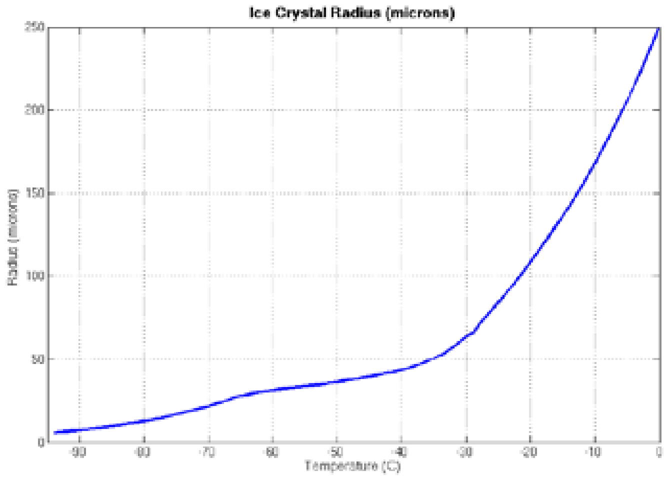

Fig. 3.3: The existing relationship between model temperature and assumed radiative effective radius of ice species in the WRF v3.4.1 code.

effective radii of cloud water, cloud ice, and snow from the Thompson et al. (2008) microphysics scheme into the RRTMG scheme. The updated code is now available in versions numbered v3.5.1 or higher when using only the combination of Thompson et al. (2008) or Thompson and Eidhammer (2014) microphysics options together with RRTMG shortwave and longwave radiation schemes. At the time of this writing, no other combinations for microphysics and radiation options contain proper physical coupling in a non-WRF-Chemistry version of the model. The cloud droplet, cloud ice, and snow radii are directly computed using the fundamental droplet and ice/snow parameters specific to the microphysics scheme. Using each species own number distribution and mass-diameter assumptions, a fully consistent effective radii is computed in the microphysics body of code and subsequently passed to the RRTMG interface code. Since the usual size of rain drops and graupel particles is far larger and the number density far lower than the other three species, rain and graupel were neglected in the radiation treatment as is currently done within all WRF radiation schemes at this time.

The radiative effective diameter (D_e) of water drops is the ratio of third (M_3) to second (M_2) moments of the drop size distribution (Slingo, 1989) as shown in Eq. (1) below:

$$\overline{D}_e = \frac{M_3}{M_2} = \frac{\int_0^\infty D^3 N(D)dD}{\int_0^\infty D^2 N(D)dD} \tag{1}$$

where D is diameter, $N(D) = N_0 D^{\mu} e^{-\lambda D}$ is the assumed size distribution, μ is the gamma shape factor and λ is the slope, which after integrating over the entire size distribution produces the final radiative effective radius (r_e) given by Eq. (2).

$$\bar{r}_e = \frac{1}{2} \times \frac{(3+\mu)}{\lambda} \tag{2}$$

The cloud water gamma distribution shape parameter, μ, varies as a function of droplet number concentration, which is fixed constant in Thompson et al. (2008) but not constant in the “aerosol-aware” Thompson and Eidhammer (2014) scheme. As such, changes to number concentration with constant liquid water content properly lead to changes in mean effective radii, something that is otherwise not available in a non-WRF-Chemistry framework. Similar to cloud water droplets, the cloud ice variable also follows a generalized gamma distribution but with $\mu = 0$, which effectively creates an inverse exponential distribution for cloud ice.

In order to compute a radiative effective radius of snow, all characteristics of the assumed snow number density function and size-to-mass relation must be used. Since the Thompson et al. (2008) scheme implements the Field et al. (2005) number distribution function, shown below in Eq. (3),

$$N(D) = \frac{M_2^4}{M_3^3}\left[\kappa_0 e^{-\frac{M_2}{M_3}\Lambda_0 D} + \kappa_1\left(\frac{M_2}{M_3}D\right)^{\mu_s} e^{-\frac{M_2}{M_3}\Lambda_1 D}\right] \tag{3}$$

and the Cox (1988) mass-diameter power law [$m(D) = 0.069D^2$], the calculation of effective radius of snow is profoundly different than one might get if spherical and constant density snow combined with an exponential distribution was assumed. To illustrate how different these values can be, a sample snow size distribution found at T = -20°C and snow content of 0.2 g m^{-3} produces a radiative effective radius of 336 μm when using all the proper characteristics of the microphysics scheme. If constant density (100 kg m^{-3}), spherical snow and an inverse exponential distribution is used together with a Y-intercept parameter of $2\text{x}10^7$ m^{-4}, taken from Houze et al. (1979), then the calculated radius would be 634 μm. However, if the standard WRF interface code for ice radius was applied, then the value would be approximately 100 μm (referring to Fig. 3.3). This is illustrated in Fig. 3.4 showing the distribution represented by Eq. (3) using values previously mentioned as well as the inverse exponential distribution.

Unfortunately, in the initial implementation of the calculations of snow size, a mistake was made in which the snow size was incorrectly diagnosed by accidentally setting Λ_1 to zero, thereby only considering the first term on the right-hand side of Eq. (3), which means that radiative effective radius of snow originally used the part of the snow size spectrum shaded in gray in Fig. 3.4. The incorrect snow size code was run by OU-CAPS for the duration of the 2013 Spring Experiment, and the error was not discov-

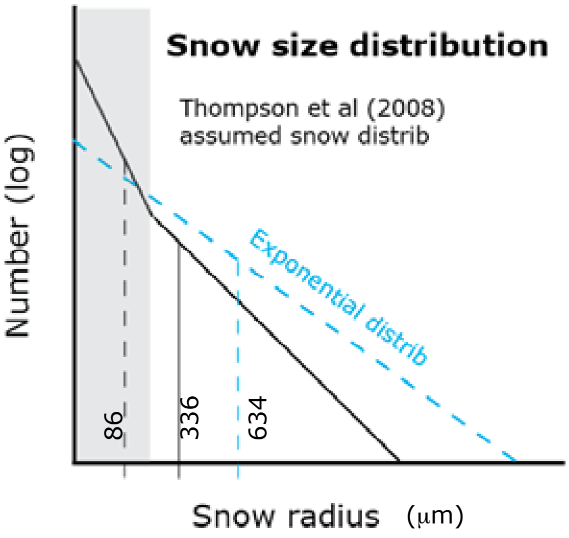

Fig. 3.4: A sample snow size distribution assumed in the Thompson et al. (2008) scheme and its associated radiative effective size assuming only the first term on R.H.S. of Eqn. (3), gray shading, as well as the full distribution and an example exponential distribution assumption.

ered until later that summer. Once corrected, OU-CAPS produced a new set of simulations using the corrected code for the simulations of 08 and 18 May. It was simply too costly to re-run a larger number of simulations with the newly corrected code. The nomenclature in the results and remaining sections will refer to the “control” or “uncoupled” WRF ensemble member for the original WRF v3.4.1 code that did not couple the cloud water, cloud ice and snow size to the RRTMG radiation code. The WRF ensemble member with coupled but incorrect snow size is referred to as “m25” while the corrected snow size was used in the ensemble member called “m30” for two days only. These two days were picked at random and were representative of most days with broad cloud areas in synoptic regime flow in the north parts of the domain and measoscale convection in the south.

3.2.3 Observed satellite data

Observed GOES-13 satellite data were collected between 23 Apr and 22 May 2013 but had to be switched to GOES-15 from 23 May to 06 Jun due to a total outage of GOES-13 from 23 May onward. In the results section below, some comparisons will be made for times and locations considered to be cloudy versus either cloudy or clear, so the observed satellite data was post-processed into a simple cloud mask. The cloud mask was created first using the normalized GOES visible albedo (channel 1, 0.67 μm) exceeding 25% combined with solar zenith angle exceeding 0.2 radian (daytime). Since this will also capture highly reflective desert surfaces, the data were subsequently screened for pixels whose difference from a climatology of satellite albedo differed by more than 10%. For example, bright pixels in the southwest desert areas of the U.S. had to have an albedo exceeding 10% of their climatological value in order to be classified as cloudy. The first albedo screening would also result in some clear-sky, snow-covered ground pixels being misidentified as cloudy. Therefore, these pixels were screened using the multi-spectral infrared data using channel 2 (3.9 μm) and channel 4 (10.8 μm) after scaling radiances into brightness temperatures, BT2 and BT4 respectively. Prior diagnosed cloudy pixels were changed to clear-sky snow cover if $-20 < BT4 < 0C$ and $(BT2-BT4) < 2$. Although fairly simplistic overall, this cloud mask worked effectively due to the time of year (May-June) and the scene of view since most snow-covered ground was confined only to mountainous regions. Such a simplistic method would not work to identify clouds year-round or worldwide.

3.2.4 Synthetic (WRF) satellite data

Simulated GOES channel 4 IR brightness temperatures were generated hourly (0-48 h) from all WRF model output using the Successive Order of Interaction (SOI) forward radiative transfer model (Heidinger et al. 2006; O'Dell et al. 2006) code provided by the University of Wisconsin group, who also used the same program in a similar way to compare model to observations in Cintineo et al. (2014). The only change from their prior usage was a more accurate calculation of radiative effective diameter of cloud droplets, cloud ice, and snow consistent with the Thompson et al. (2008) microphysics scheme using the same equations presented earlier. The software to create synthetic satellite images from WRF output generated other GOES IR channels, however, for the results section below, only the channel 4 results indicative of cloud-top temperature were used.

3.2.5 Shortwave radiation measurements

Observations of shortwave radiation reaching the ground were retrieved from 116 U.S. Climate Reference Network (USCRN; Diamond et al. 2013) sites and 15 Ameriflux sites around the continental U.S. for the time period of interest. In the results section below, when comparing the WRF data to these measurements during daytime periods only, we screened the measurements for times when the satellite-determined solar zenith angle exceeded 0.2 radian. In addition, for comparing times during which clouds existed, the USCRN data were screened by the simplistic GOES satellite mask mentioned above.

3.2.6 Surface temperature observations

Hourly measurements of surface temperature at 2500 to 3000 airports in the domain shown in Fig. 3.2 were collected from the National Weather Service METAR-format observations. In addition, approximately 75 USRCRN sites included temperature data, however, we found that these data essentially added nothing new to the results found below due to the density of METAR data across the U.S. Similar to the radiation measurements, we screened the temperature data points to locations with clouds found in the simple GOES cloud mask as well as any WRF model points that had clouds. Since the overall aim of this research is to isolate the impact of modeled cloud-radiation coupling, any clear sky temperature bias in the model was not the focus of this study.

3.3 Results

One of the major difficulties in analyzing these ensemble model sensitivities is that the magnitude of the error/bias of any individual member as compared to observations greatly exceeds the change in error by introducing the radiation coupling. While this might imply that the coupling is relatively unimportant, we plan to show specific cloud regimes in which positive impacts to incoming surface radiation and temperature forecasts results from this addition (Section 3.4). Since the focus of this study investigates cloud and radiation coupling, we concentrated our analysis on locations in both the observations and the model in which we diagnosed the existence of clouds in all of the products. Due to the model initialization time of 0000 UTC, which is near sunset time in the U.S., and due to model spin-up time, we neglected the first 6 hours of each forecast.

3.3.1 Satellite comparison

An example of the observed and synthetic satellite data near 1800 UTC 08 May 2013 is shown in Fig. 3.5. Clockwise from top-left is the GOES-13 observed IR brightness temperatures, followed by the control, m25, and m30 experiments, respectively. Overall the correspondence is relatively good with five primary features present: 1) a well-developed low-pressure system over the northeast U.S., 2) a mix of shallow/warm and mid-troposphere clouds extending from north to south through the central U.S., 3) scattered, moderately cold clouds extending from CO to OR likely along a frontal boundary, 4) a combination of high-altitude cold clouds in north TX over the top of shallow/warm clouds to its immediate south; 5) a band of clouds associated with an upper-level jet stream approaching the northwest coast of Mexico.

While the general cloud patterns of these five regions were rather well matched in all three WRF ensemble members and closely resemble the observations, there are some discrepancies to note. One area of concern is the amount of cloud cover associated with the northeast U.S. low pressure region (#1). In general, there are more extensive and colder clouds in the observations than shown in any WRF ensemble member. The next region westward (#2) has an even greater discrepancy, particularly with pixels in the observations of clouds with temperature approximately -10 to -15°C. This lack of clouds at these approximate temperatures was also clearly highlighted in Cintineo et al. (2014; their Fig. 3.6) and represents

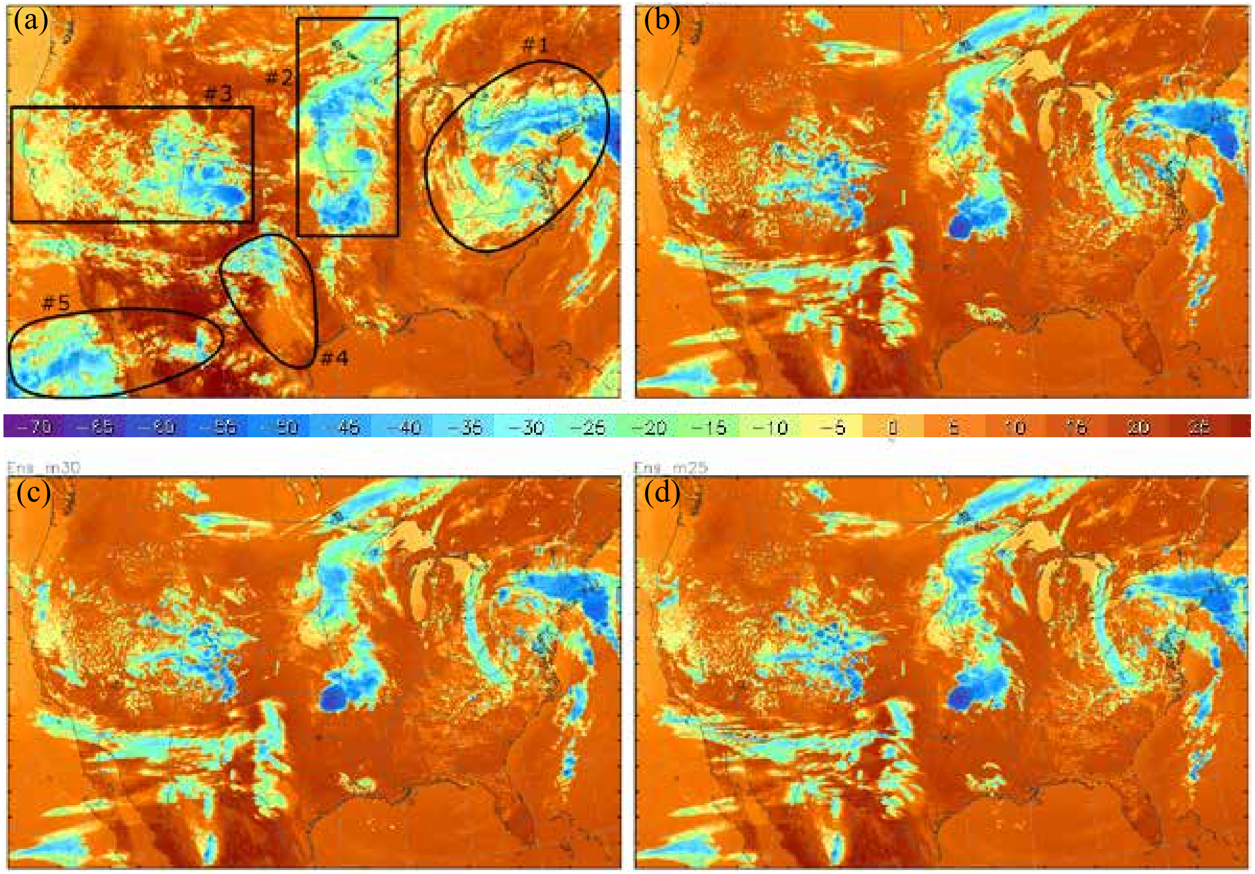

Fig. 3.5: (a) GOES-13 channel 4 infrared (IR) satellite image valid 1745 UTC 08 May 2013 with numbered cloudy regions mentioned in the text, WRF synthetic IR satellite image from the (b) Control experiment, (c) m30 experiment, and (d) m25 experiment.

a challenge to the numerical weather modeling community. We also note the general nature of more isolated and sporadic clouds seen in WRF as compared to the observations across the mountains from CO to OR (#3). None of the WRF simulations appears to have sufficient horizontal coverage of clouds in this region. The area of deepest convection near the center of the image (#2) appears more narrow in WRF than in the observations. The low/shallow clouds in region#4 in south Texas are poorly represented in the model. Lastly, the high-level clouds off the Mexican coast appear to be represented in WRF, however the height or depth may be too low/shallow with insufficient horizontal coverage because the satellite observations show broader and colder cloud tops there.

At first, we were tempted to believe that this general lack of cloud coverage might be just a simple matter of this particular day and time. However, upon deeper analysis, this condition appears to be prevalent throughout the duration of the WRF simulations over the 34 days studied and fully confirms numerous findings in Cintineo et al. (2014). A relative frequency analysis of all 34 simulation days from hourly (6-48) WRF control ensemble member versus satellite observations of IR brightness temperature in 5° C intervals is shown in Fig. 3.6. The relative frequency of specific ranges of IR temperatures

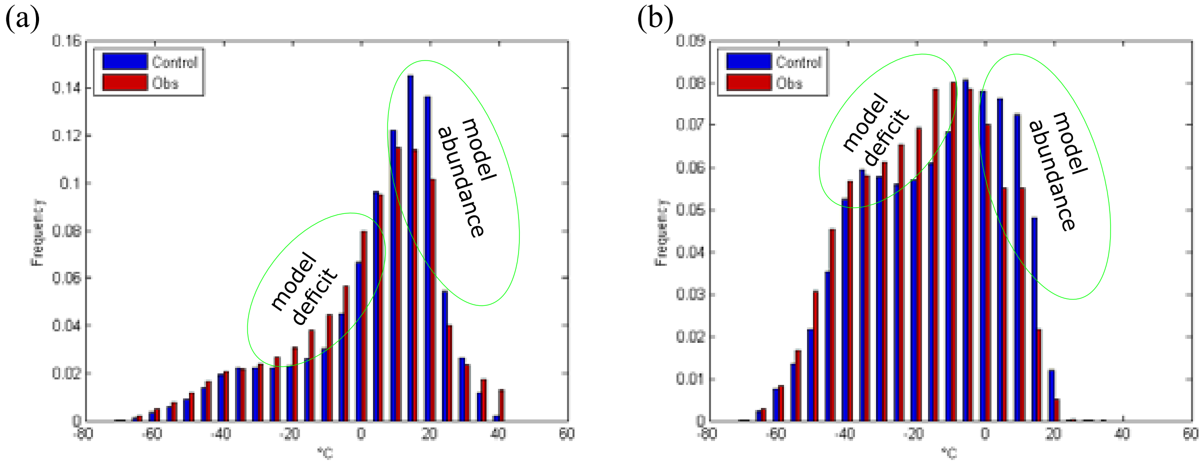

Fig. 3.6: Relative frequency of observed and WRF control member of specific 5°C intervals of infrared brightness temperature from all pixels (a) and from cloudy-only (b). Note the abundance of model points between 10 and 25°C as compared to observations, but also the deficit of model points between 0 and -25°C.

confirms what is seen visually by comparing the observed versus synthetic satellite imagery (Fig. 3.5). Besides confirming the prior work that included all WRF model grid points against observed IR temperatures, whether clear or cloudy, our analysis isolating only cloudy regions also shows the same general bias, which indicates that many WRF clouds do not extend to the proper height and are too shallow compared to observations. The same analysis was performed on WRF ensemble members m25 and m30 and revealed indistinguishable results from the control member shown in Fig. 3.6 and supports our assertion that analyzing only two days (08 and 18 May) is sufficient to show various discrepancies between the different WRF ensemble members, since we do not have the m30 member on any other days.

As further evidence of the overall lack of sufficient cloudiness in the model, and its dependence on forecast hour, we analyzed the overall hourly fraction of cloudy points in satellite observations versus WRF when the sun angle was high enough to eliminate any reasonable chance of including clear-sky pixels as clouds. Shown by the red line in Fig. 3.7 are the two daytime periods of cloud fraction in the GOES satellite data with a 34-day average in the 40-50% range whereas the WRF control member, shown in blue, was consistently predicting fewer cloudy pixels. The green line labelled “overlap” represents the

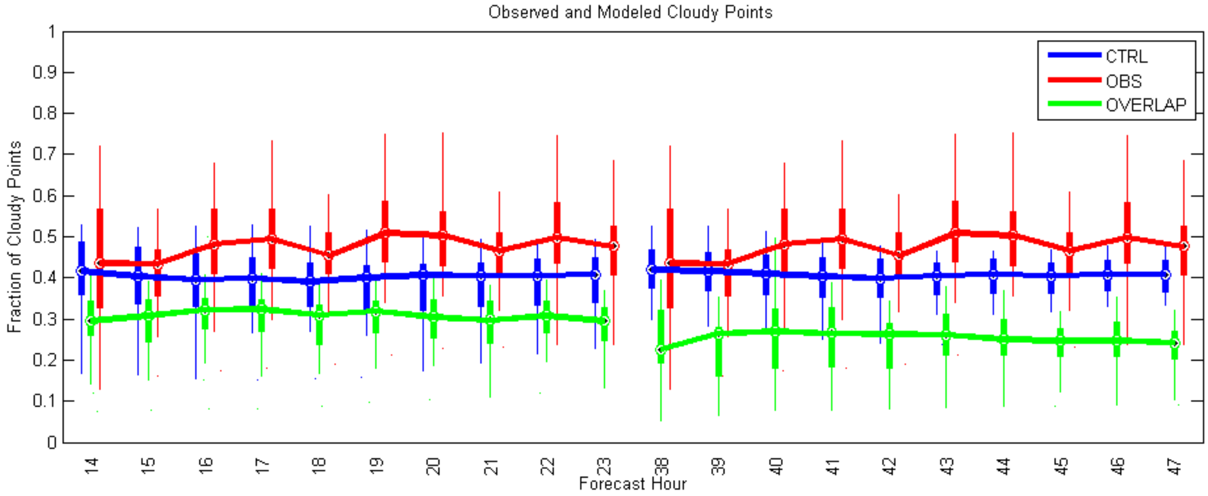

Fig. 3.7: Fraction of cloudy points from GOES observations (red) as a function of forecast hour (during relatively high solar angle) as compared to the WRF control ensemble member (blue) from 34 days of simulations. For each simulated hour during 34 days, the fraction of grid boxes containing clouds in the observations and simulations was calculated to create the boxplot. WRF consistently shows lower cloud fraction than observations. The fraction of the domain covered in clouds in both the observations and WRF is labeled "overlap" (green).

fraction of the domain that was diagnosed as cloudy in both observations and WRF. Whether or not WRF exhibits similar biases through different seasons has not yet been analyzed.

3.3.2 Shortwave radiation reaching the ground

The WRF control member data were interpolated using simple bi-linear method to the observational sites for the comparison shown in Fig. 3.8. When analyzing by the relative frequency of occurrence of specific 100 W m^{-2} intervals of shortwave radiation, we see that the model generally shows an excess of solar radiation reaching the ground when considering all points, cloudy or not (solid color-filled bars). When analyzing only the observational sites found to be cloudy in both the model and observations,

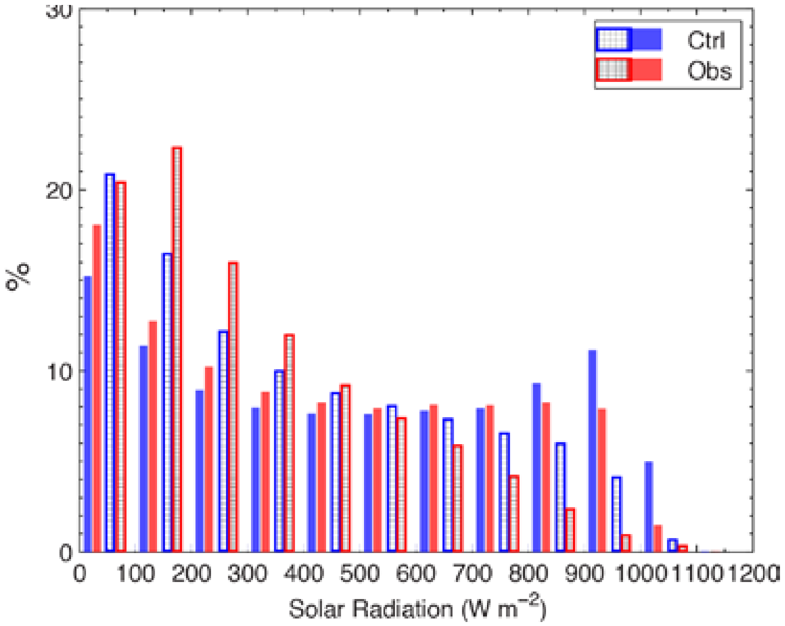

Fig. 3.8: Relative frequency of USCRN and Ameriflux observations of incoming surface solar radiation in bins of 100 W m-2 versus WRF control member regardless of whether the observing location has clouds or not (solid bars). The hatched bars represent observing locations diagnosed as having clouds overhead.

there are still too many locations receiving too much radiation in the model. The preponderance of WRF points with more solar radiation than found in observations is a clear indication of the lack of sufficient cloud coverage and/or physical cloud depth and/or the optical treatment of cloud properties in the radiation scheme. When combined with the preceding satellite data analysis, it is clear that some of the cause of excessive incoming solar radiation reaching the surface is due to insufficient areal coverage and thickness of clouds.

While Fig. 3.8 represents an analysis of all 34 days between the control member and the observations, a subsequent analysis of only the two days including the m30 ensemble member is shown in Fig. 3.9. Furthermore, the analysis in Fig. 3.9 represents only those points considered to be cloudy in the observations and each of the WRF ensemble members just as those points are represented by the hatched rectangles in Fig. 3.8. Among the subtle differences between the WRF ensemble members, the m25 member clearly has the largest number of points with the lowest radiation values. We interpret this to mean that the improper calculation of snow size too small produces a larger quantity of almost fully opaque clouds. The control experiment has far fewer sites with near fully opaque clouds and the m30 experiment has the fewest and matches the observations rather closely. On the other hand, as the measured incoming solar radiation increases, the control and m30 experiments are generally well-matched while the m25 experiment is clearly different. Again, due to the smaller radii calculated by m25, the clouds generally became more opaque so the relative fraction of points with high incoming radiation does appear better in m25 than either control or m30, but this is the right answer for the wrong reason as the overall opaqueness of the clouds is likely too great due to the excessively small snow radii. As such, we postulate that if the WRF model was doing a better job forecasting the

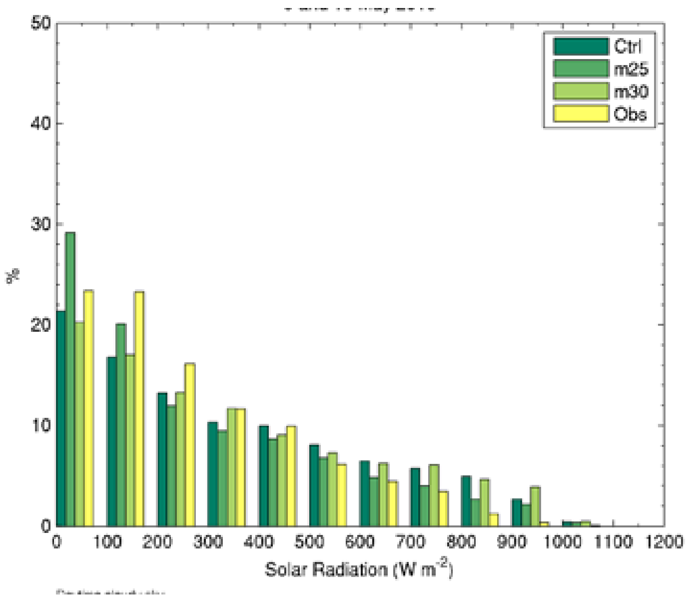

Fig. 3.9: Same as Fig. 8 except only at diagnosed cloudy points from the two days (May 08 and May 18) with all three WRF ensemble members.

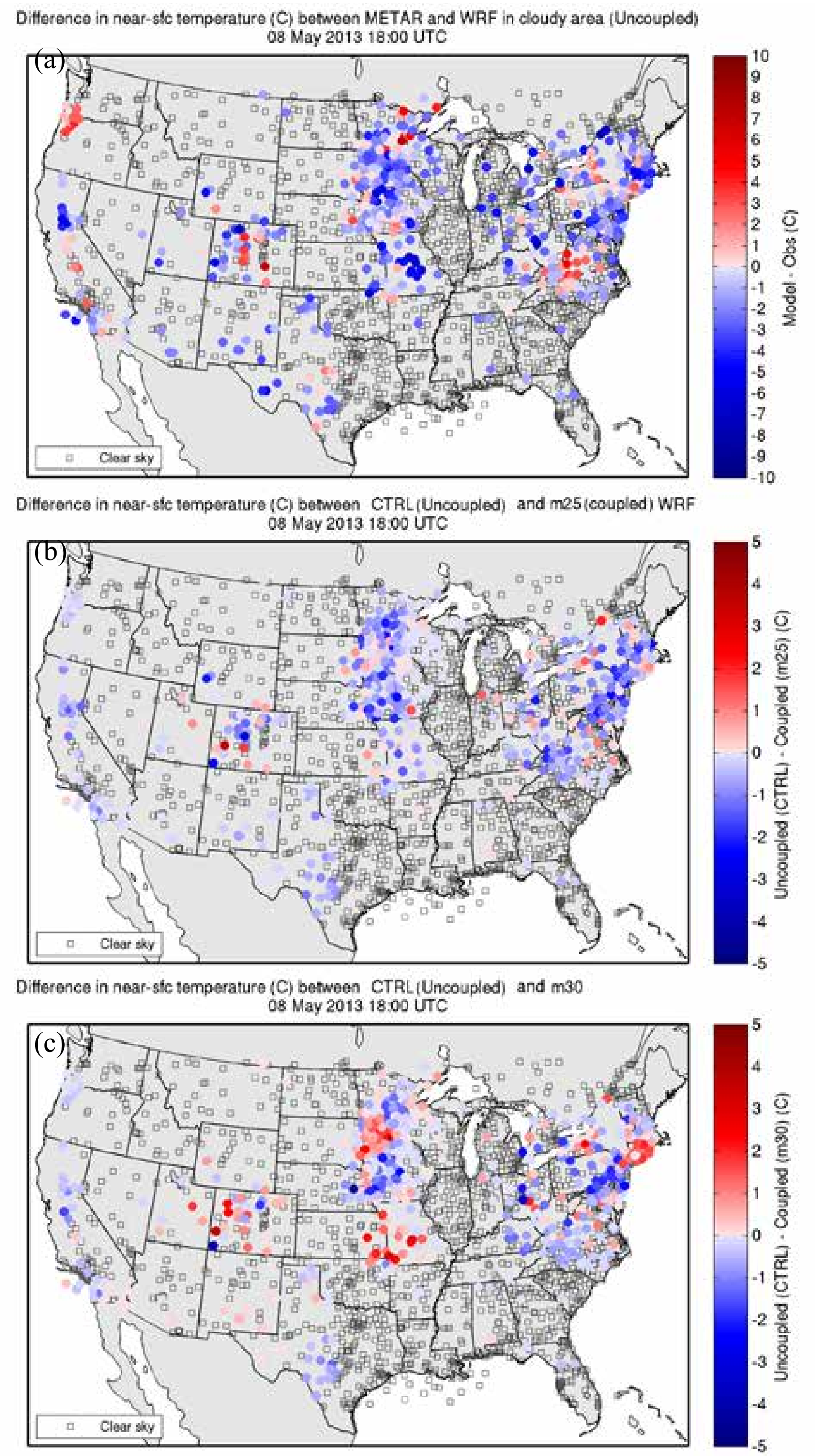
Difference in near-sfc temperature (C) between METAR and WRF in cloudy area (Uncoupled)
08 May 2013 18:00 UTC

Difference in near-sfc temperature (C) between CTRL (Uncoupled) and m25 (coupled) WRF
08 May 2013 18:00 UTC

Difference in near-sfc temperature (C) between CTRL (Uncoupled) and m30
08 May 2013 18:00 UTC

Fig. 3.10: Differences in near-surface temperature (°C) between WRF control member and (a) observations valid at 18:00 UTC 08 May 2013 (same time as Fig. 3). Differences in near-surface temperature (°C) between control and m25 (b) and control and m30 (c).

physical cloud depth and coverage, then it would be very likely that the incoming solar radiation would be over-attenuated because of the snow size calculation being too small in m25 member. On the other hand, the m30 member appears to represent rather well the thickest and most opaque clouds and fully incorporates the microphysics parameterization effective radii of water drops and ice crystals while the control member uses uncoupled a priori assumed sizes.

3.3.3 Surface temperature comparison

One of the final outcomes of the impacts of clouds and radiation in a numerical weather prediction model is the forecast surface temperature. An example of a single time WRF model forecast error of low-level temperature is shown in Fig. 3.10. Observational data are shown as color-filled and open circles where surface METAR reports are taken at approximately 2500 sites each hour. Sites that were excluded from the analysis are shown by open circles because such location either lacked clouds in the observed satellite data or one or more WRF ensemble members had no clouds at the location. The top panel shows the model minus observations from the control or uncoupled experiment while the middle and lower panels show the differences be

We avoid discussion of the clear-sky tended to address the interactions betwee that Fig. 3.10a clearly shows the prepond the incoming solar radiation was previou Instead, the overall model bias with the e turbulence, clouds and radiation, leads to whether clear or cloudy, we found there t 34-day period analyzed. Clearly seen in in locations with clouds. Notable exceptions is a low-altitude stratus cloud deck found near the OR/WA border and another cloud area near the V

In the next panel, Fig. 3.10b, the diff and m25 is shown. As suspected because snow size that is too small, the bias gener radiation than control. However, when s can note that some points now warmed, p note the previously mentioned areas near member, they were too warm, but the pro temperature bias slightly (additional discussion of this region in the next section).

Rather than considering only one day and time, the overall temperature biases in each ensemble member is confirmed by creating box plots from all time periods of both days seen in Fig. 3.11. The box

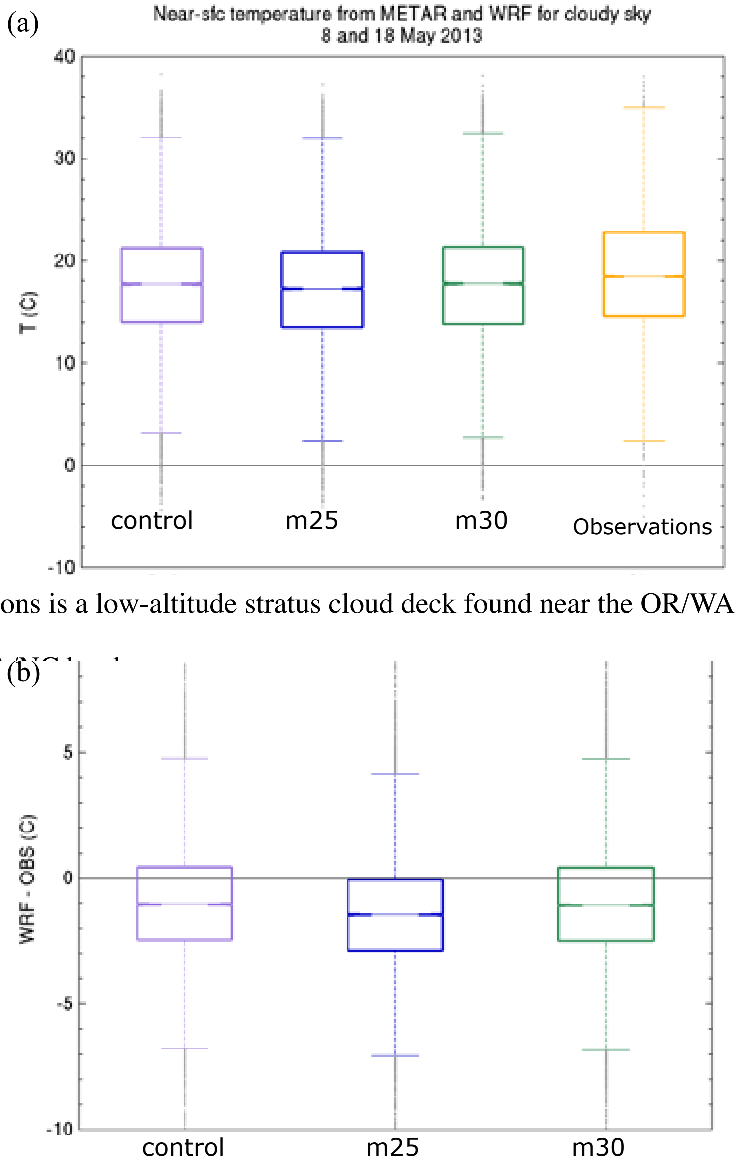

Fig. 3.11: Box plot of (a) observed (METAR) and WRF forecast, near-surface temperature for all hours, 6 to 48, from two days with all three WRF ensemble members. To distinguish WRF ensemble members, the lower panel (b) has the model minus observations distributions showing the generally lower temperatures in m25 compared to the other members.

plot show that bias appears very similar between control and m30 and more significant differences in m25. While Fig. 3.11a shows two days of observed temperature data and WRF forecasted temperature, a similar plot of all days (not shown) exhibit the same biases in control and m25. In fact, the temperature errors appear relatively small overall with significant overlap between all experiments and the observations. A more focused view of the bias (Fig. 3.11b) helps to separate the members a little better. The smaller overall snow size contributes to lower solar radiation (confirmed in subsection a and b above) that subsequently results in a stronger cold bias in low-level temperature. Although the box plot does not show a statistically-significant change, it supports the early statement that the clouds became too opaque.

In general, these results reveal somewhat systematic biases in these WRF simulations with regard to incoming solar radiation and resulting surface temperatures beneath clouds. Although the radiation bias is generally higher in WRF than in the observations, the low-level temperature comparison reveals a cool bias in temperature. One part of the cool bias can be explained by the usually strong near-surface heating at this time of year and the fact that METAR observations are taken near 2 meters whereas the lowest WRF model level at approximately 25 meters was used to calculate the bias. From local noon to late afternoon, when the atmospheric lapse rate may approach its dry adiabatic value of 9.8 K km^{-1}, the maximum error due to height difference alone would be about -0.25 K, which could account for part of the

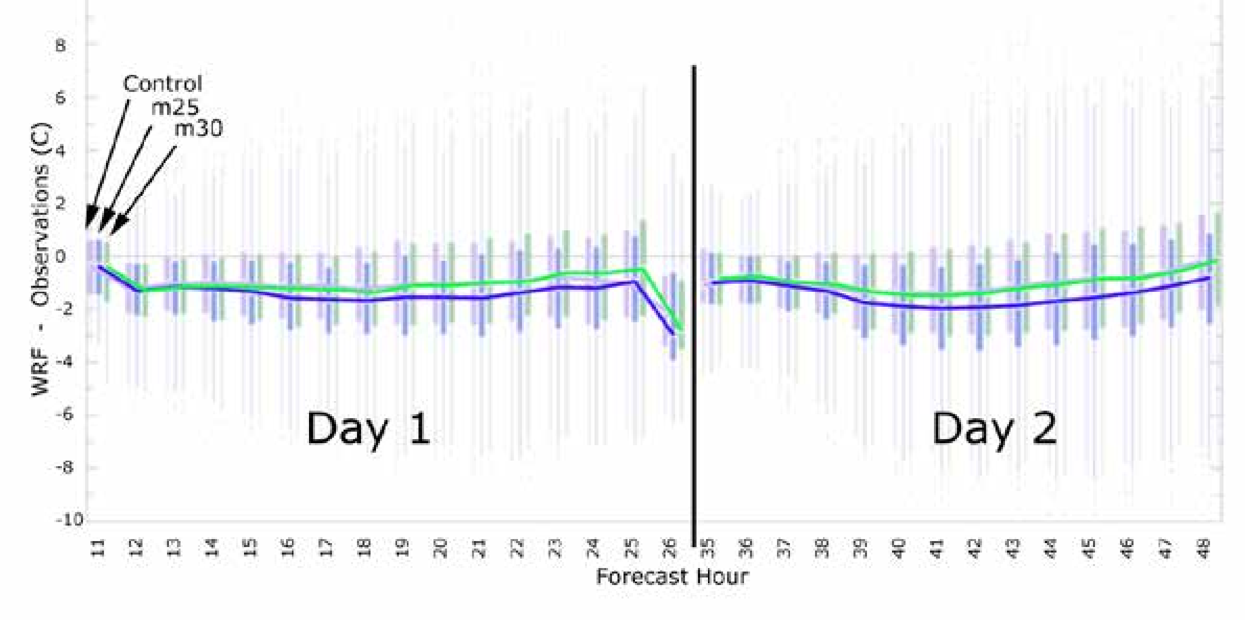

Fig. 3.12: The daytime evolution of near-surface temperature bias between the three WRF model ensemble members and METAR observations. The results of Control and m25 are nearly indistinguishable whereas m25 clearly drifts to a larger negative bias as each forecast day progresses.

three ensemble members during the two daytime periods of the total 48-h forecast. Note from the figure how the three ensemble members are nearly identical at approximately sunrise time and slowly diverge through the first day with noticeably cooler diurnal evolution in the m25 experiment compared to the other two experiments. The same basic progression occurs on the second daytime portion of the forecast as well.

3.4 Discussion: "needles in a haystack"

It was mentioned previously that the coupled and uncoupled experiments have only minor statistical differences for general characteristics of synthetic satellite analysis, solar radiation reaching the surface, and near-surface temperatures, however, there are certain cloud conditions worthy of more detailed investigation. As an example, Fig. 3.10a revealed a concentrated region of high temperature bias along the Pacific coastline near the border of WA and OR when using the uncoupled experiment that subsequently showed improvement in both the m25 and m30 experiments (Fig. 3.10b,c). This cloudy region was composed of low-altitude stratus clouds without any ice, so this specific region can be examined for the changes due to radiation passing through liquid water clouds only. A glimpse of a single level of WRF liquid water clouds in the region (Figs. 3.13a-c) shows that the uncoupled WRF experiment has the least LWC whereas the two coupled experiments clearly have more LWC at a single level. A snapshot of visible cloud albedo from GOES satellite is shown in Fig. 3.13d revealing widespread cloudiness at low altitudes with clear skies at the higher elevations over the Olympic and Cascade mountains. As further evidence, the corresponding WRF synthetic satellite visible albedo images are shown in Fig. 3.13e-g. Both coupled microphysics-radiation sensitivity experiments show more broad cloud coverage than the uncoupled experiment even though total cloud coverage in this region is still far less than what was observed.

As a second example of nearly the same type, Fig. 3.14 shows a small region of south Texas where shallow stratocumulus clouds are evident on the satellite image (Fig. 3.14a). As in Fig. 3.13, the control experiment has less overall extent of clouds than either the fully coupled m25 or m30. Clearly the integrated interaction/feedback between microphysics and radiation can give rise to differences in explicitly represented cloud water on NWP time scales. More subtle is the very thin ice cloud in the upper-left corner of each WRF graphic (Fig. 3.14b-d). The m25 experiment with the smaller snow radii is causing this cloud to appear more opaque than either the control or m30 experiment.

Another region worthy of more detailed investigation is the lower half of circled region#1 in Fig. 3.5a. It turns out that this region very well represents the bias of cloud top temperature seen in both Fig. 3.6b and the prior work of Cintineo et al. (2014). Recall that there is a model abundance of clouds with tops near 0 to +20°C, whereas there is a clear deficit of clouds in the -5 to -25°C temperature regime. The

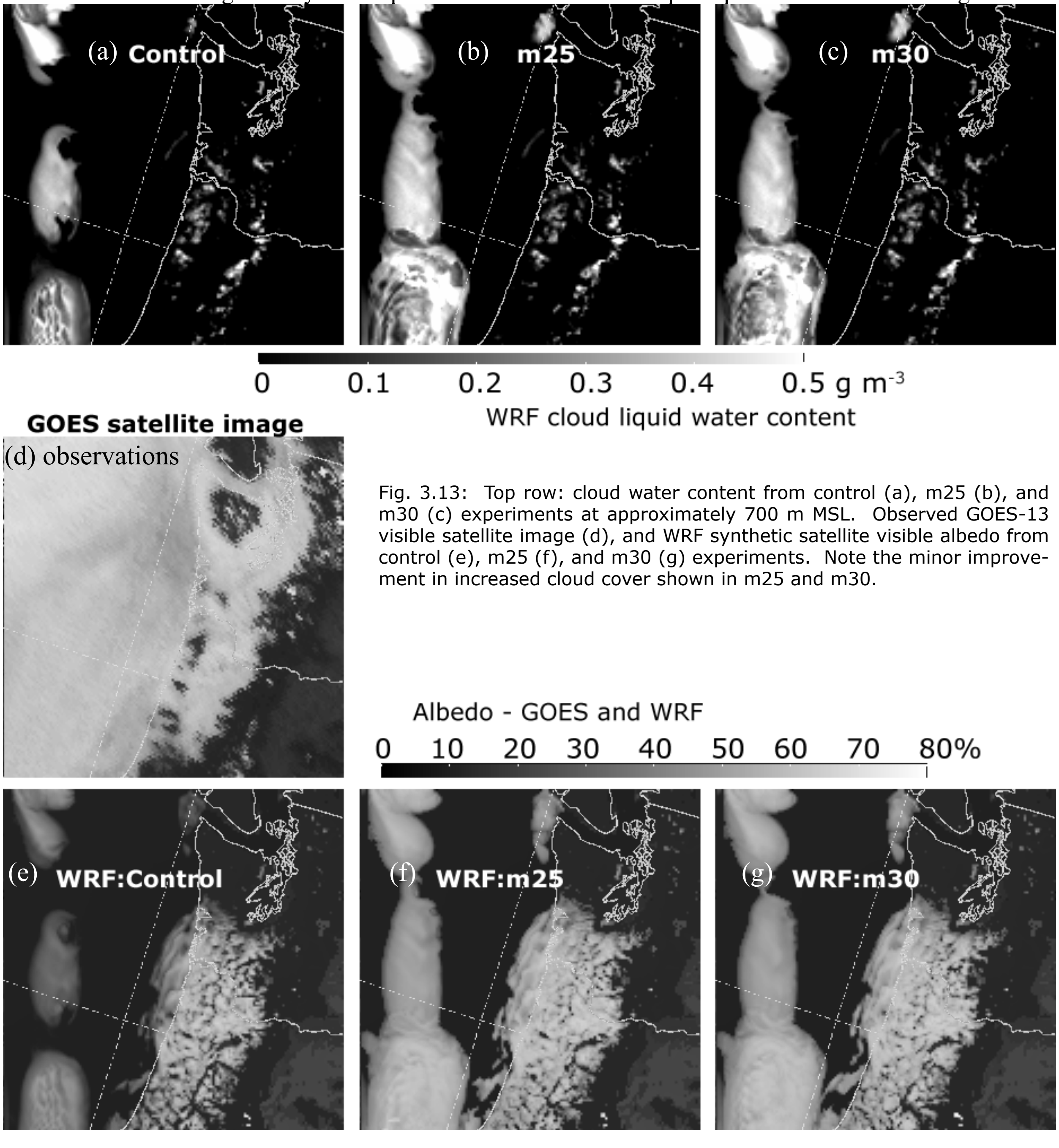

Fig. 3.13: Top row: cloud water content from control (a), m25 (b), and m30 (c) experiments at approximately 700 m MSL. Observed GOES-13 visible satellite image (d), and WRF synthetic satellite visible albedo from control (e), m25 (f), and m30 (g) experiments. Note the minor improvement in increased cloud cover shown in m25 and m30.

WRF synthetic satellite images from each ensemble member do reveal there to be model cloudiness similar in coverage to the observed in this region, but the clouds are modeled too low in the atmosphere (CTT too warm). A future step will be to study the reason why clouds in this portion of the cyclone are not achieving sufficient depths with possible causes related to vertical mixing and entrainment, model grid spacing, microphysical deficiencies or other reasons.

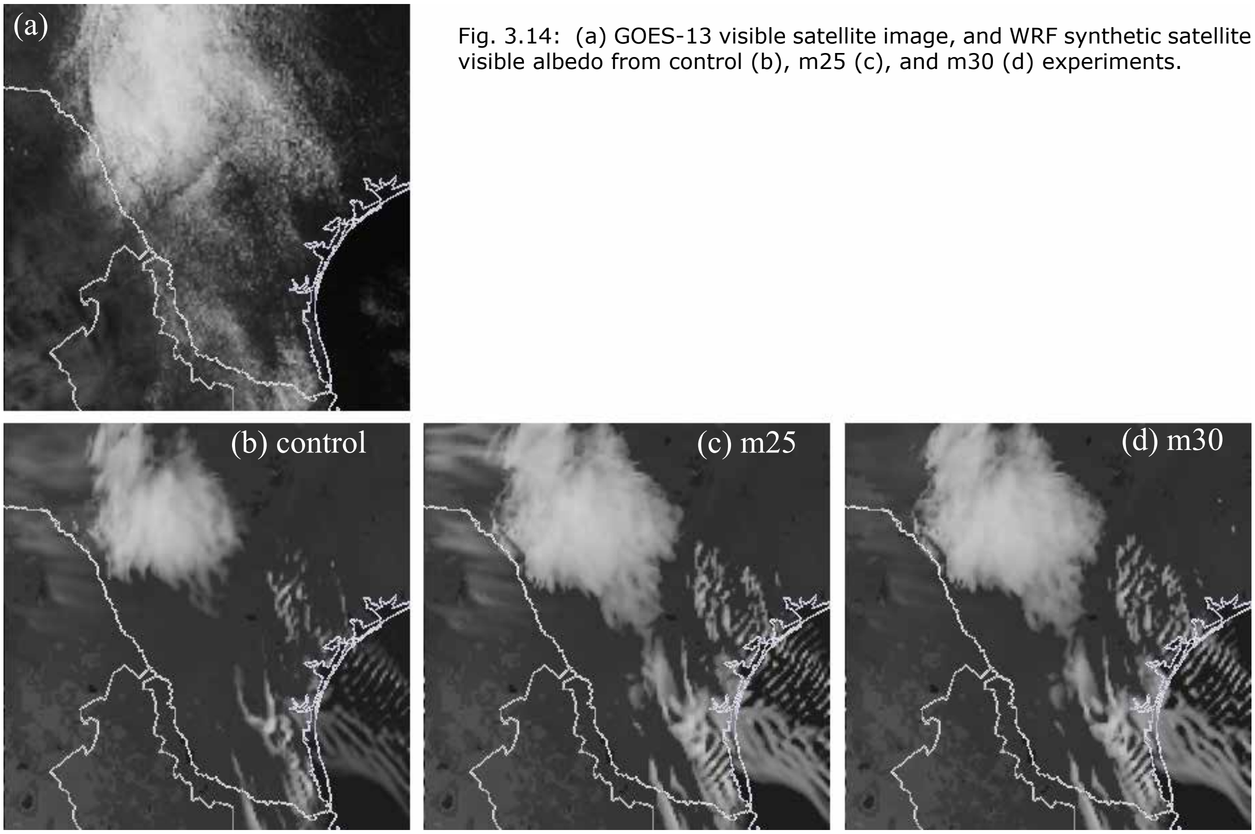

Fig. 3.14: (a) GOES-13 visible satellite image, and WRF synthetic satellite visible albedo from control (b), m25 (c), and m30 (d) experiments.

3.5 Conclusions

Explicit coupling between the Thompson microphysics scheme and the RRTMG radiation scheme for the purpose of calculating cloud optical properties is now available in WRF (v3.5.1 and higher). This new feature combined with the “aerosol aware” version of Thompson and Eidhammer (2014) provides the opportunity to simulate explicitly the aerosol indirect effects in the non-WRF-Chemistry version of the WRF model, which has significant computational advantages.

In addition to describing the coupling method, this study evaluated the impact of the coupling on high-resolution convective forecasts. Generally, the coupling showed relatively isolated and modest improvements relative to the uncoupled version of the model, in large part due to the greater overall errors in cloud forecasts present in the model. The coupling showed sensitivity to the treatment of ice/snow size, however, as demonstrated by the varying results between the “m25” and “m30” experiments. Treating cloud ice/snow as too small or too large can lead to somewhat substantial biases when comparing against observed satellite data.

In general, we conclude that the initial assumptions used to calculate effective radii and cloud optical depth in the uncoupled model were not large sources of error, at least for the mid-latitude clouds studied herein, but the former version of the code excluded the possibility to permit the aerosol indirect effects and were not appropriate for all cloud types. Furthermore, many researchers have begun using WRF and similar NWP models as a regional climate models and the proper coupling of different physical parameterizations should be thoroughly investigated for various couplings.

3.6 Acknowledgements

The authors wish to thank David Gill, Jimy Dudhia, and Wei Wang for their advice and support of various WRF code modifications. NCAR is sponsored by the National Science Foundation. This work was performed as part of NCAR’s Short Term Explicit Prediction (STEP) program, which is supported by the National Science Foundation funds for the United States Weather Research Program (USWRP). The OU-CAPS storm-scale ensemble forecasts were produced under the support of NOAA’s CSTAR program (NA17RJ1227), using computing resources at the National Science Foundation XSEDE National Institute of Computational Science (NICS) at the University of Tennessee and those at the OU Supercomputing Center for Education and Research (OSCER).

4. A Numerical Weather Model's Ability to Predict the Characteristics of Aircraft Icing Environments

This chapter is reprinted with permission from:

Thompson, G., M. K., Politovich, and R. M. Rasmussen, 2016: A numerical weather model's ability to predict the characteristics of aircraft icing environments. Wea. & Forecasting, (submitted).

4.0 Abstract

Recent advances in high-performance computing has enabled higher resolution numerical weather models with increasingly complex data assimilation and more accurate physical parameterizations. With respect to aircraft and ground icing applications, a weather model's cloud physics scheme is responsible for the direct forecasts of water phase and amount and is a critical ingredient to forecasting future icing conditions. In this paper, we compare numerical model results to aircraft observations taken during icing research flights and evaluate the general characteristics of liquid water content, median volume diameter, droplet concentration, and temperature within aircraft icing environments. The comparison reveals very promising skill by the model to predict these characteristics consistent with observations. The application of model results to create explicit forecasts of ice accretion rates for an example case of aircraft and ground icing are shown.

4.1 Introduction

Large volumes of aircraft icing data were collected and analyzed in the 1940s and 1950s when the FAA originally created rules for flight into icing conditions, known currently as Title 14 Code of Federal Regulations Part 25 Appendix C. Although newer instrumentation was developed in subsequent decades, additional data collected in the 1980s and reported by Sand et al. (1984) confirmed and validated what was previously analyzed. Jointly the FAA and the research community agreed that Appendix C captured the environmental conditions associated with icing encounters. Two fundamental classifications of icing conditions were stated in Appendix C as continuous versus intermittent maximum icing, based on flights through "stratiform" and "convective" clouds, respectively. For decades since, Appendix C, which is generally based only on cloud drop sizes with mean effective diameter smaller than 50 microns, has sufficed for aircraft certification purposes for new and existing aircraft, although Jeck (2001) described variations in interpretations and rule changes that have plagued its application/interpretation since inception.

Following the crash of an ATR-72 aircraft near Roselawn, Indiana on 31 Oct 1994 (NTSB, 1996; Marwitz et al. 1996), more focus has been placed on aircraft icing environments with water drops having diameters larger than what is described by Appendix C. Therefore, more recent data collection programs have investigated supercooled large drop (SLD) conditions. Various newer icing data collection efforts led by NASA, the FAA, and Environment Canada have concentrated on collecting SLD icing data in an attempt to extend Appendix C. These data are summarized in Cober and Isaac (2012) and Cober et al. (2009) and form the basis for the new Appendix O icing envelope for SLD (FAA, 2014).

While SLD conditions have garnered more attention in recent years, more sophisticated icing forecast algorithms have evolved as well. One of the earliest in-flight icing forecast algorithms applied relatively simplistic temperature and humidity thresholds to the Nested Grid Model output (Schultz and Politovich, 1992) to automate icing predictions. This general technique of "data mining" the output of numerical weather prediction (NWP) models was refined using vertical thermodynamic profiles by Forbes et al. (1993) followed by Thompson et al. (1997). Further refinements came from satellite, radar, surface stations, lightning network and pilot reports (Bernstein et al. 2005). These research efforts led to establishing the FAA-sponsored Current Icing Product (CIP) and Forecast Icing Product (FIP), which are run operationally by the National Weather Service. In CIP, the most recent weather observations are merged together with output from NOAA's Rapid Refresh (RAP) model to create a snapshot of current icing conditions over the Continental U.S. As a system that provides icing forecasts, FIP relies solely on the RAP model's thermodynamic and water phase data (Bernstein et al. 2005). Conceptually, if a numerical model correctly predicts the evolution of thermodynamic and moisture variables properly, then post-processing algorithms used to supplement explicit model-forecast variables will incrementally diminish since the direct prediction of icing relies on the direct prediction of supercooled liquid water.

The skill of numerical weather prediction models has continued to increase in recent years due to advances in high-performance computing permitting smaller grid spacing, data assimilation techniques, and improved physical parameterizations. This paper will discuss the last of these items in terms of the model component responsible for cloud and precipitation development: the microphysics scheme. Ultimately, the best possible direct model forecast of aircraft icing starts with the best forecast of water phase and amount, and the microphysics scheme in a weather model is responsible for creating all water species in the simulated atmosphere.

The Thompson et al. (2008) bulk cloud physics scheme has been used in the operational RAP model since May 2012. The scheme undergoes extensive development and testing as part of the FAA's Aviation Weather Research Program with regular code updates targeted at improving explicit forecasts of aircraft and ground icing as well as quantitative precipitation forecasts. In the most recent upgrade to the scheme by Thompson and Eidhammer (2014), activation of aerosols as cloud condensation nuclei (CCN) and subsequent explicit prediction of cloud droplet number concentration allows more realistic cloud environments often responsible for icing. The earlier versions of the scheme assumed a constant cloud droplet number concentration of 100 cm^{-3}, which is far from ideal considering the model simulates weather over an entire continent where variations from one-fourth to ten times larger droplet concentrations are very likely to exist.

In order to validate the numerical model results specific to aircraft icing environments, the model output using the newer "aerosol-aware" microphysics scheme was compared to observations that comprise the aforementioned Appendix C and Appendix O data. In subsequent sections of this paper, a direct case-by-case comparison of model to observed data is neither possible nor the purpose, but, rather, an analysis of the more general characteristics of most frequently found values of the key variables is performed in order to lend more credence to model results and, subsequently, the application of model results to explicit model-based icing forecasts. Furthermore, the aircraft data collected to form Appendix C and O occurred many years prior to the modern NWP models we have now. In Section 4.2, the observation data briefly mentioned above will be expanded in more detail. Then, in Section 4.3, we will briefly describe the numerical model and retrieval method of variables used in the subsequent Results (Section 4.4). Section 4.5 contains the potential application of explicit SLW model data to compute an ice accretion rate whereas Section 4.6 contains a sample case study. Then, Section 4.7 contains some overall conclusions.

4.2 Observational data

All of the observed data used in this study were provided directly by the FAA's William J. Hughs Technical Center and are fully described in Jeck (1998) and Jeck (2010). The data were taken over multiple decades, and the human effort to collect and analyze roughly 61,000 km (33,000 nmi) of cloud penetrations is tremendous. To coincide with each of the FAA Technical Reports, the earlier Jeck (1998) database essentially covers Appendix C conditions whereas the latter Jeck (2010) study concentrates primarily in SLD conditions or Appendix O. A brief description of each database is included below whereas the reader is referred to each reference for greater detail.

Observations that comprise the Appendix C database extend from the surface up to 7.3 km (24,000 feet) over portions of North America, Europe, and the northern oceans with about half collected by the National Advisory Committee for Aeronautics (NACA) in the 1940s and 1950s, whereas the other half were collected in modern years. Newer measurements came from various research projects having aircraft equipped with Particle Measuring Systems (PMS) cloud droplet size spectrometers, hot-wire liquid water meters, and other complementary sensors. Analyses have shown that the NACA data and modern data compared favorably with each other in the determination of LWC and MVD even though the measuring techniques were radically different.

The start of an icing event was defined by a threshold droplet concentration and liquid water content and terminated when the aircraft exited such conditions or changed altitude. This resulted in 3285 layer cloud events ranging in path length from 300 m to 296 km and 3234 convective cloud events ranging in path from 100 m to 51 km. The samples are independent with no overlap in time periods. Although these data were originally split between "layer" and "convective" clouds that form the basis for "continuous" versus "intermittent" icing, respectively, however, for comparison purposes in the present paper, this distinction is ignored. Furthermore, the current intermittent maximum envelopes in 14 CFR-25, Appendix-C, apply only to wintertime convective (cumuliform) clouds. They do not apply to thunderstorm interiors or to summertime, strongly convective clouds (Lewis, 1969).

The SLD data detailed in Jeck (2010) were collected over a limited portion of North America, such as the Great Lakes area, Colorado, Kansas, California, the Canadian east coast, and the Canadian Arctic, and a limited amount of data from Europe and the southern tip of South America. Nearly all the data collected for this database belong to wintertime, stratiform cloud conditions because these are believed to be the primary source of reported, SLD-related accidents and incidents. It is known, however, that SLD are generally plentiful in warm season convective clouds. Nevertheless, practically no SLD data from summer convective clouds were obtained for this database.

The principal selection criteria for admitting data into this database was a requirement for at least 0.01 g m^{-3} of liquid water in drops larger than 50 μm diameter for at least 1 uninterrupted nautical mile of flight. This combination of LWC and exposure distance was arbitrarily established as the threshold of concern for SLD exposures and for building a database of significant SLD measurements. By choosing the 30-second average data, which roughly corresponds to a path length of 3 km (assuming an airspeed of 100 m s^{-1}), 2444 data samples were incorporated together with the 6519 data samples from the earlier flight campaigns.

4.3 Model data

The Weather Research and Forecasting (WRF) community model is a fully compressible non-hydrostatic numerical weather prediction model that uses a mass-based terrain-following grid (Skamarock and Klemp 2008). It is widely used in education, research, and weather prediction centers around the world. Two specific configurations of WRF are run operationally within NOAA with a primary objective to improve aviation weather hazard forecasts of icing, turbulence, precipitation, cloud ceiling, and visibility. In one configuration, the Rapid Refresh (RAP) model applies a grid spacing of approximately 13 km whereas the High Resolution Rapid Refresh (HRRR) model utilizes a 3 km grid spacing (Benjamin et al. 2016).

In the present study, we configured WRF similarly to the HRRR model with 4 km horizontal grid spacing and 50 vertical levels using stretched spacing of ~30 m near the ground gradually increasing to the model top (~16 km). In total, the grid is 1360 x 1016 x 50 points covering the entire contiguous U.S. and portions of Canada and Mexico as shown in Fig. 4.1. Unlike the HRRR and RAP models that run every hour with a new cycle of data assimilation/analysis and subsequent forecast times from one to fifteen hours, our WRF simulation was run continuously from the start date of 01 Oct 2001 until 30 Sep 2013. As such, this type of simulation is a form of "reanalysis" of real weather conditions during the simulated time because WRF utilized the 6-hourly European Center for Medium-Range Weather Forecasts (ECMWF) reanalysis for its lateral boundary conditions in contrast to using a pure forecast model to drive the lateral boundaries in WRF. Since running WRF with this large a grid could lead to a drift between real and simulated weather patterns, a weakly-forced spectral wave number nudging technique was employed to keep the model interior solution synchronized with the long wavelength (approximately 2000 km scales and larger) weather systems.

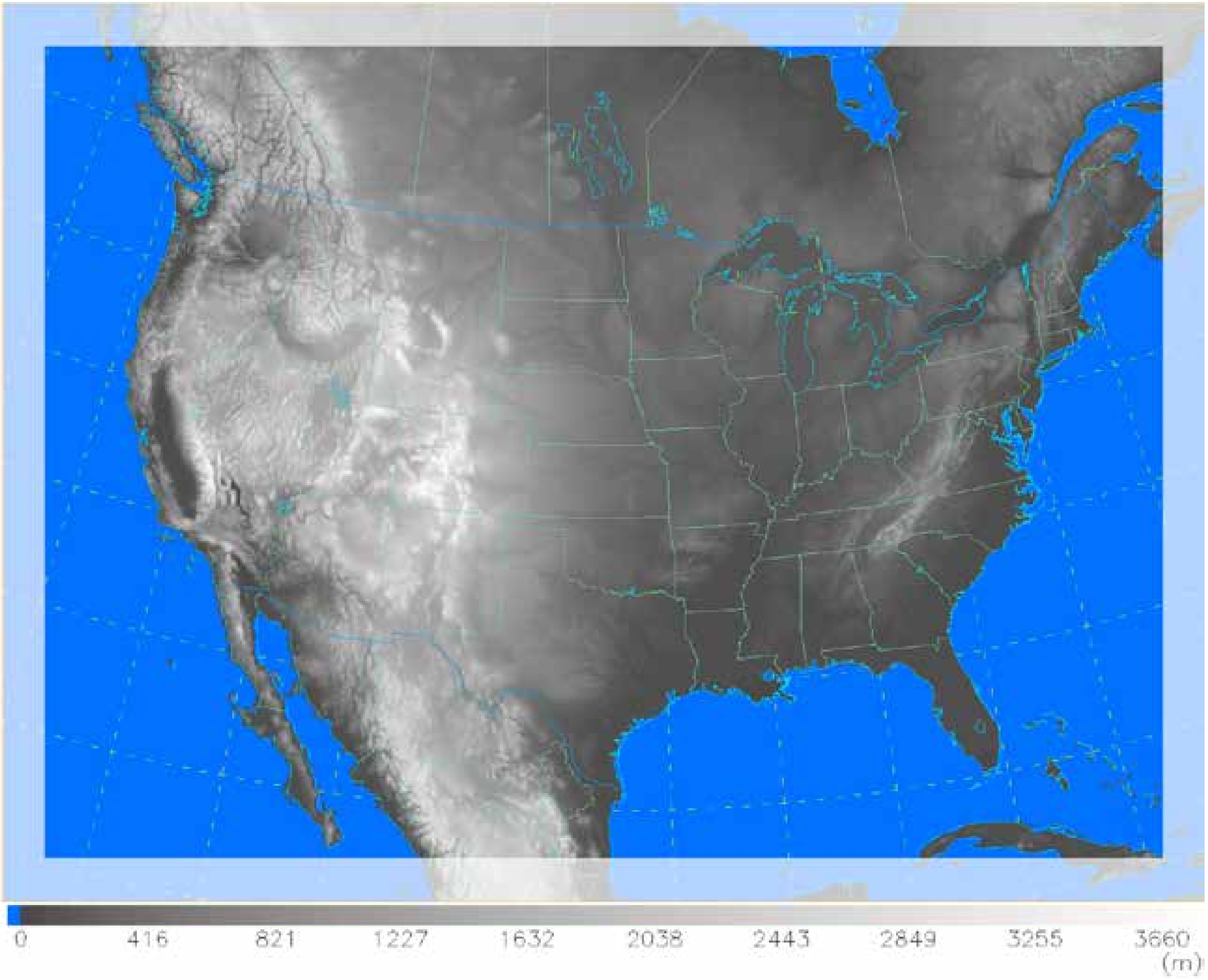

Fig. 4.1: WRF model domain showing topography height. The partly-shaded ring around the edge shows the 50 model points eliminated from statistical analysis due to higher likelihood of being influenced by the lateral boundary conditions.

As stated in the introduction, the new Thompson and Eidhammer (2014) “aerosol-aware” microphysics parameterization was employed, which is a critical ingredient for predicting icing environments because it includes explicit prediction of both the cloud water mass content and number concentration. As of this writing, NOAA's RAP and HRRR models use the older version of the scheme with constant droplet number concentration, whereas a scheduled implementation date of May 2016 will update the microphysics to the newer one used in this study. Having a more physically correct coupling between aerosols that act as CCN into the droplet number concentration is important for calculating properly the median volume diameter (MVD) of water drops that may impinge on the aircraft wings.

Other physical parameterizations included in this WRF simulation were the Noah-MP land surface model (Barlage et al. 2010), the RRTM-G radiation scheme (Iocono et al. 2000), and Yonsei University planetary boundary layer scheme (Hong et al. 2006). Since the model was run at convection-permitting scales, we did not use a cumulus cloud parameterization assuming that clouds are mostly resolved at this model resolution. Coarser model resolutions typically use a convective parameterization to account for convective clouds. WRF version 3.4.1 constituted the base version of code with changes to couple the cloud physics and radiation variables as described in Thompson et al. (2016) as well as various bug fixes after extensive testing.

In the following analysis, we skipped the first simulated year but included all of the next ten years of cool season data from 15 Oct to 15 Apr to compare against the observations. Ten half-years of 3-hourly saved WRF data comprise 28 TB of total data, therefore, we extracted columns of model data based on nearly 280,000 time-matched voice pilot reports (PIREPs) with explicit icing information. For each icing PIREP from 30 minutes prior to 30 minutes after the top of each hour (00:00, 03:00, 06:00 UTC, etc.), we retrieved the set of WRF variables at all 50 levels for three consecutive "rings" of model points that surrounded the reported position in the PIREP. This data mining technique reduced the total records from ~10^{12} to a final database size of 500 million records, containing WRF-model pressure, height, temperature, wind, humidity, and all water species: cloud water, rain, cloud ice, snow, and graupel.

For an ideal comparison, we would have model simulations of the same events and times as the data that were collected by aircraft documented by Jeck (1998, 2010), however, that isn't feasible, and point-by-point comparisons of model forecasts versus observations aren't possible using these data. However, the aircraft measurements were taken on various days and times and represent clouds of many types and sizes from a variety of environmental conditions. Likewise, our collection of 60 cool-season months of simulation over most of North America encompasses all of the same cloud types and environmental conditions. Thus we feel this sub-sample fairly well represents the range of modeled atmospheric conditions.

4.4 Results

In the first analysis of observed versus model liquid water content, we refer to Fig. 4.2 showing the FAA's 5605 cool-season values of LWC versus temperature and one million similar points from the WRF model. The preponderance (97%) of observed LWC > 0.01 g m^{-3} was found with T > -20°C. The 50th percentile of observed LWC is approximately 0.1 g m^{-3} regardless of temperature, while the 90 and 99th percentile are about 0.35 and 0.65 g m^{-3} respectively. Some tendency for LWC decreasing with decreasing temperature is evident, as would be expected if the probability of forming ice increases, which would result in lower LWC since clouds tend to glaciate once ice is formed (due to the Bergeron-Wegener-Findeisen process). Qualitative inspection of similar findings by Cober and Isaac (2012; Fig. 2 and Fig. 8), Sand et al. (1984; Fig. 4) and Politovich and Bernstein (2002; Fig. 8) all show similar corroboration to Fig. 4.2.

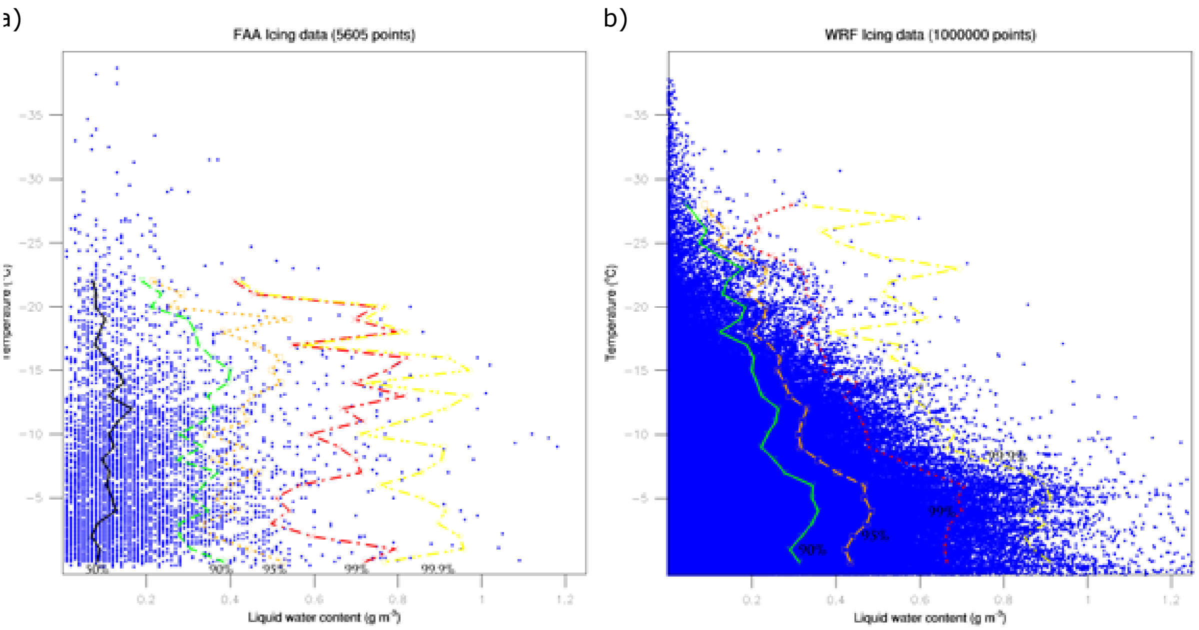

Fig. 4.2: Observed (a) liquid water content vs. temperature from 5605 measurements in icing clouds. Distribution percentiles (50th, black; 90th, green; 95th, orange; 99th, red; and 99.9th, yellow) are labeled when at least 20 points per degree temperature and per 0.05 g m^{-3} water content were found. (b) Same as in (a) except a random sample of 1 million WRF model points with supercooled liquid water. The 50th percentile is omitted because it is always found in the first water content bin due to including any LWC>0 whereas the observed data had a 0.05 g m^{-3} water content threshold

The WRF-model results show a more prominent decrease of LWC with decreasing temperature than found in the observations. This could be due, in part, to the non-random sampling done by icing flight scientists. The usual inclination of flight scientists would not be to sample the lowest possible LWC with high frequency, nor the relatively low temperature regimes where icing would not be as commonly found as at higher temperatures. The 50th percentile of the WRF LWC distribution is approximately 0.05 g m^{-3}, but this would include all LWC > 0, and a great many points would also be in thin clouds or near cloud base, which flight scientists would have no interest in sampling as often as random sampling of the model data that these points represent. Therefore, the lower distribution percentiles in WRF would be expected to be lower than the observed values. However, note that the 90, 95, and 99th percentiles are a relatively close match to the observed values at the highest temperatures and have gradual declines as temperature decreases. The exact accuracy of the declining LWC amount with decreasing temperature is subject to further study and an aircraft measurement campaign that strictly flew in a random sampling strategy could be a worthwhile endeavor.

An alternate view of the observed versus model variability of LWC with temperature is shown in Fig. 4.3. The relative frequency of occurrence of particular intervals of LWC (0.05 g m^{-3}) and temperature (5°C) show a much more obvious trend in the WRF model than seen in the observations. In particular, for each 5°C decrease in temperature, the relative frequency of high LWC values rapidly decreases in WRF. There is only a minor hint of the same trend seen at low LWC values in the observations. Given that the Y-axis is presented in log scale, the agreement between observations and the model is very good. Note in particularly the slope of the lines showing the highest temperature ranges in WRF as compared to the same lines in the observations.

Besides LWC, another important variable in the physics of aircraft icing is the size of water droplets, typically expressed as the median volume diameter (MVD). Both the FAA icing database and Sand et al. (1984; Fig. 9) show that 75% of all MVD values in icing occur between 10 and 20 μm. An analysis of nearly 20M WRF model points with any supercooled liquid water had 75% of MVD values in this range as well (not shown). In a similar manner to Fig. 4.3, the relative frequency of occurrence of a specific range of MVD values in 5°C temperature bins is shown in Fig. 4.4. Both the observations and WRF show the most prominent occurrence of typical cloud droplets (6-26 μm) followed by a dramatic decrease from ~30-100 μm. While the observations show a lower secondary maximum in the typical drizzle/rain size range (MVD > 100 μm), the WRF results have nearly as many points with MVD near 200-400 μm as in the typical cloud droplet sizes. This discrepancy with the observations could be due to including all WRF model points regardless if they are found in convective clouds. As a fail-safe method to eliminate convective-like clouds in WRF is difficult to create a priori, the WRF data includes a blend of all clouds in the full 60 months of simulated cool seasons whereas the observed data were collected specifically in winter storms typically containing freezing drizzle or freezing rain conditions. Furthermore, it could be extremely unwise to fly into conditions of high LWC, large MVD, and relatively low temperatures as the aircraft could encounter the most severe

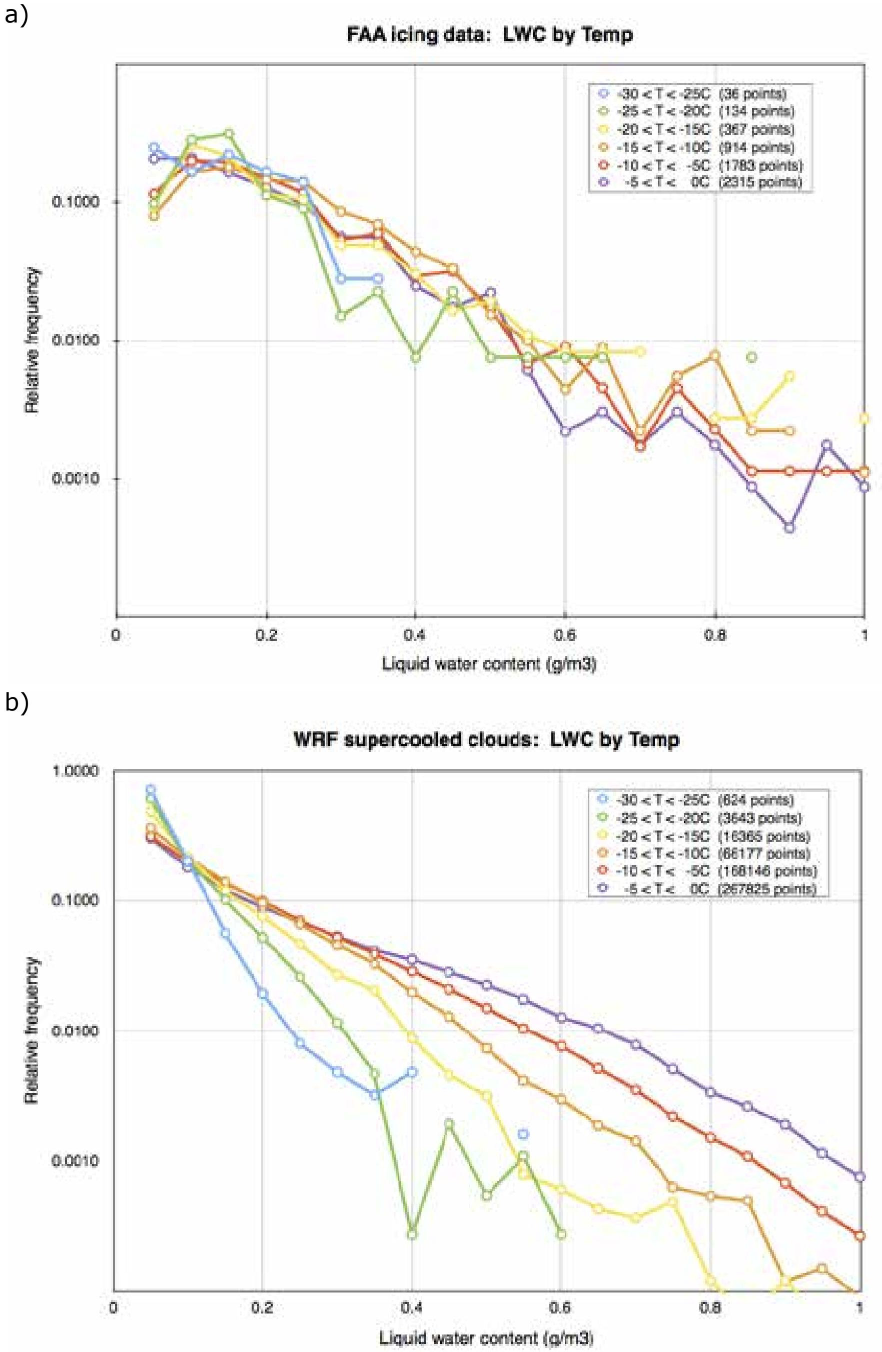

Fig. 4.3: Observed (a) compared to WRF model (b) data of relative frequency of occurence of specific ranges of liquid water content (LWC) in 5° bin interval of temperature.

of all icing conditions that could threaten the lives of the crew. For this reason, the FAA observed data likely does not include all possible conditions found in the atmosphere. However, the accuracy of the WRF results remains questionable as well.

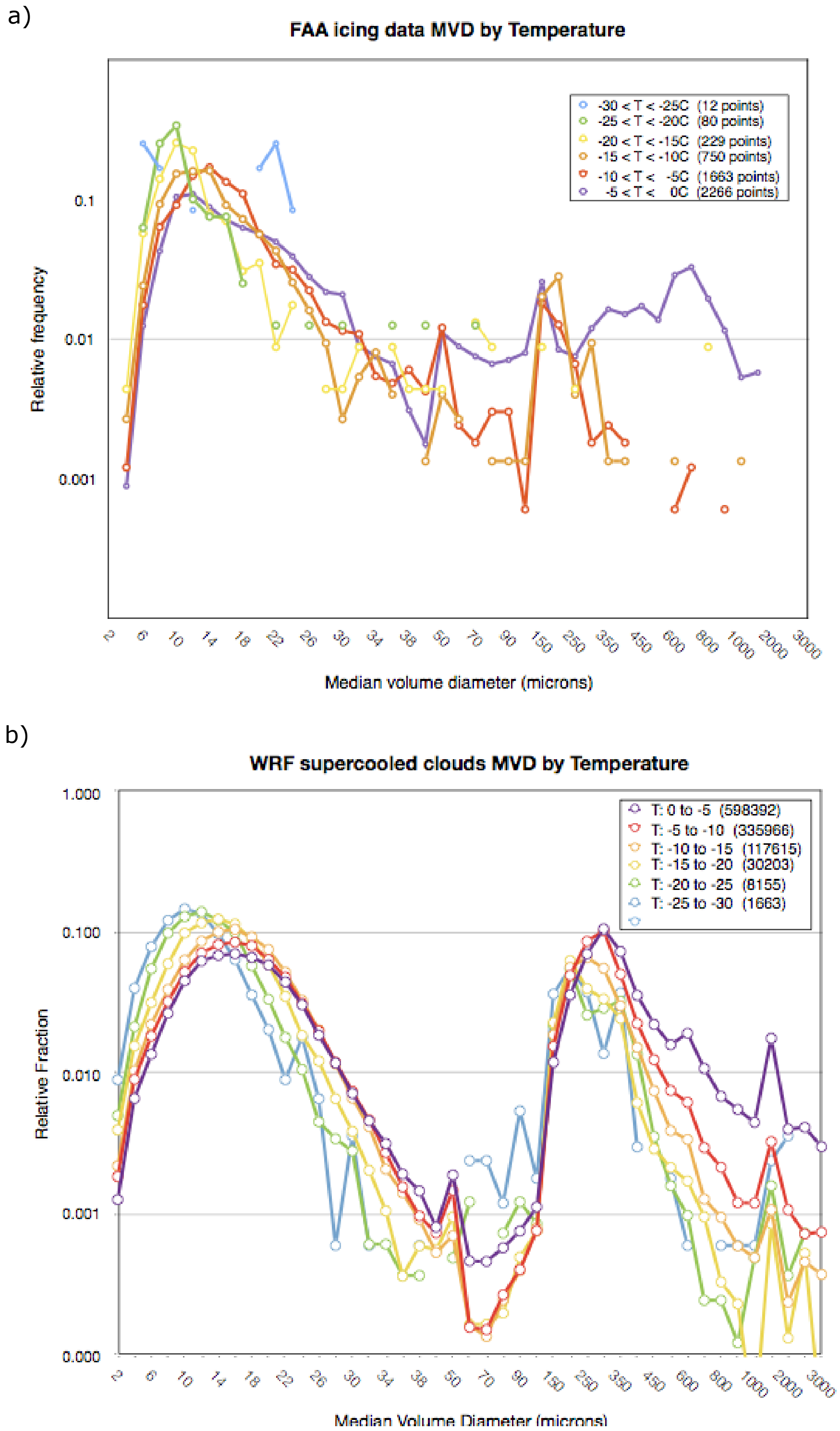

Fig. 4.4: Observed (a) compared to WRF model (b) data of relative occurence of median volume diamter (MVD) in 5° bin interval of temperature.

Also note in Fig. 4.4 that the WRF model shows a very prominent stratification of MVD with respect to temperature, with smaller MVD at lower temperature. This is less obvious in the observations, but it is still visible, especially for MVD < 26 μm. If the largest water drops are the most likely to freeze first, then it is sensible to believe the WRF model reflects natural mixed-phase clouds accurately. The simple fact that icing scientists tried to find relatively large MVD in all temperatures, but collected only 11 data points (out of 5545) with MVD > 50 μm and T < -15°C is very strong evidence to support laboratory studies that large drops freeze before smaller ones (Bigg, 1953).

An alternative means to evaluate all three previous variables (temperature, LWC, and MVD) in unison is presented in Fig. 4.5. Plotted in this figure are all 8779 FAA icing database points with X-axis values of MVD and Y-axis values of LWC, color-coded by 10°C temperature intervals. Similarly, over a half-million WRF model points are plotted in the right half of the figure. By plotting in this manner, a tendency for higher LWC and larger MVD coincides with higher temperatures in both observations and WRF. Furthermore, the preponderance of largest MVD coincides with relatively low LWC and relatively high temperatures. The small spike of WRF data points near MVD = 1250 μm is due to a mistaken numerical artifact in calculating the joint distribution MVD from separate cloud water and rain species in the WRF model.

Since liquid water content is directly proportional to the number concentration and volume of water droplets, it is possible to infer a realistic range of droplet concentrations. Recall that the earlier version of the microphysics scheme used the simplification of constant in time and space cloud droplet concentration whereas the newer "aerosol-aware" scheme explicitly predicts the CCN and droplet concentration. To illustrate if we had run the older microphysics scheme with a very low concentration of 25 cm^{-3}, we

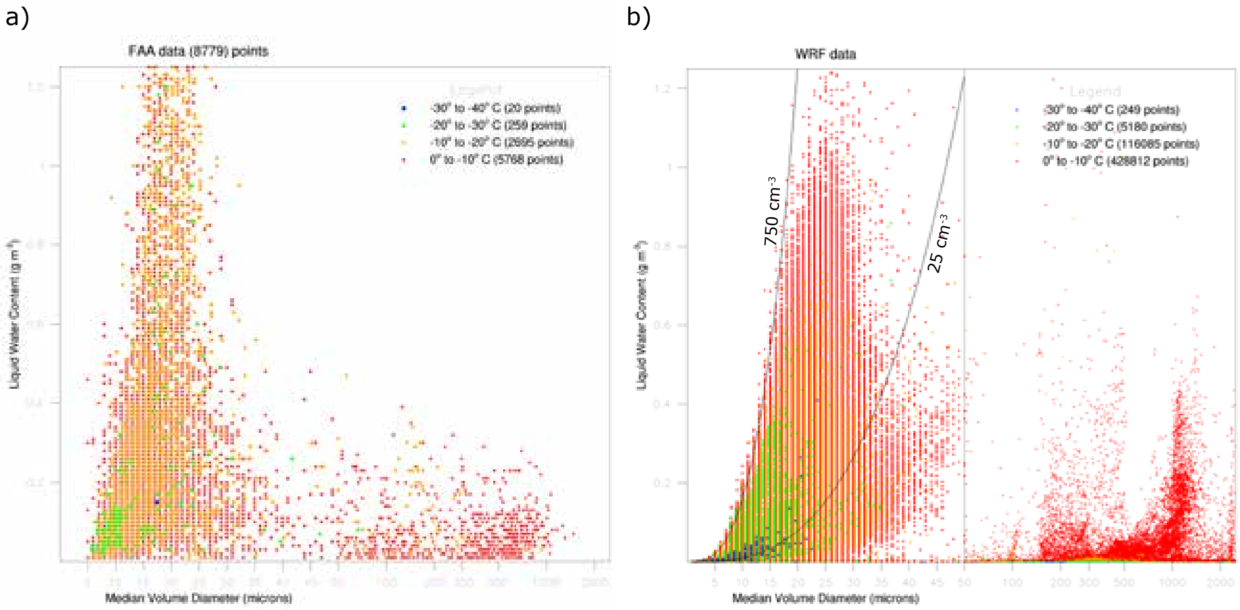

Fig. 4.5: Scatterplots of FAA observations (a) and WRF model (b) of MVD versus LWC color coded by temperature. The left portion of each panel shows typical cloud droplet size and is displayed with a linear scale of MVD whereas the right portion of each panel shows the drizzle and rain size (SLD) and uses a logarithmic scale to capture the full range of values in the data.

sketched the line to show the LWC-to-MVD relationship as well as a second line if we had an assumed concentration of 750 cm^{-3}. As you can readily see, the WRF model results using the newer scheme produce a majority of points within this range. In a very pristine airmass that typically approaches the west coast of the U.S. and is generally devoid of most anthropogenic aerosols, a typical water droplet concentration would be near the lower limit of 25 cm^{-3} whereas a very polluted airmass more typical of the urban corridor of the northeast U.S. may coincide with the upper limit of 750 cm^{-3}. It is worthwhile to note the general range of MVD-LWC combination places most points between these two values of droplet concentration, which should be quite commonly found over the continental U.S.

In a more focused analysis of observed versus model water droplet concentrations, Fig. 4.6 shows the count of specific ranges of cloud droplet number concentrations associated with specific ranges of MVD. The general decrease in occurrence of large droplet concentrations is found in both the observations and the model. The broad overall peak in observations between approximately 50 and 250 cm^{-3} is not well represented in the model results, although,

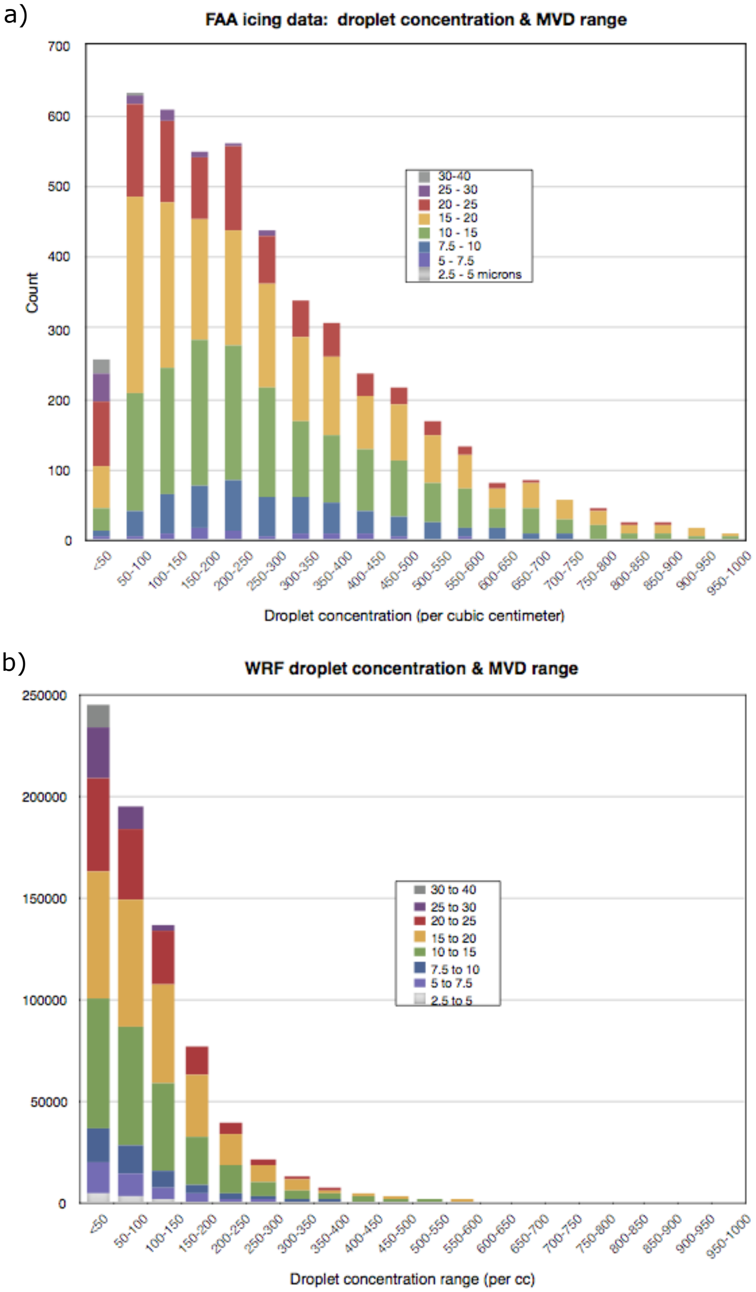

Fig. 4.6: Histogram of observed (a) and WRF-model (b) water droplet concentration in specific range of MVD

since the model incorporates very low LWC amounts, it is likely to contain many more data samples with correspondingly low droplet concentrations of relatively small size since LWC is directly proportional to the cube of diameter. Some contradiction to the observations found in Fig. 4.6a and more corroboration of the model results of rapidly decreasing number concentration is found in Fig. 10 of Sand et al. (1989).

A more subtle but highly important feature revealed in Fig. 4.6 is the trend of reduced occurrence of the largest MVDs as the droplet concentration increases. This is noted by following the color bars at the top of each column and noticing how each colored rectangle shrinks until it is removed from the plot as droplet concentration increases. This trend is easily seen in both the observations and the model and is entirely plausible and physically logical. As the number of aerosols and CCN increases (pollution), the mean size of cloud droplets formed on CCN tends to decrease for the same LWC value. In other words, in increasingly polluted airmasses, the water drop sizes tend to decrease and reduce the likelihood of encountering the relatively large drops that may be responsible for significant icing. Alternatively, more pristine environments increase the likelihood of larger drops and potentially offer greater probability of aircraft icing, which was also pointed out by Rosenfeld et al. (2013). The fact that the model is able to reproduce the observations of this effect shows the importance of increasing the complexity in model microphysics to represent the observed water droplet spectra.

4.5 Applications

Since the numerical weather model described here showed reasonable skill in representing supercooled liquid water content and drop sizes versus FAA icing observations, we apply the direct model variables to predict aircraft (or ground) ice accretion rates. The method followed here is nearly the same as that described by Makkonen (2000) together with decades-old assumptions from Lewis et al. (1947) of a 3-inch cylinder moving at 200 mph through the WRF-predicted clouds (complete details are found in the Appendix). Nygaard et al. (2011) and Podolskiy et al. (2012) similarly used WRF-simulated low-level wind speed, LWC, and MVD to compute ice accretion on a standard cylinder as a surrogate for ice accretion on ground objects (such as power transmission lines). In addition, Nygaard et al. (2011) further analyzed multiple alternative microphysics schemes besides Thompson et al. (2008) and concluded that, of the various schemes tested, the Thompson scheme gave the best results compared to observations.

In this analysis, the ice accretion calculations described in the Appendix were applied to the WRF model data for the entire 60 months of WRF simulation data. This resulted in 17M points in which the ice accretion exceeded 0.01 g cm^{-2} h^{-1}, which might represent the first perceptible ice accretion for typical aircraft. Using the thresholds suggested in Jeck (1980, 2001), values between 0.01 and 1 g cm^{-2} h^{-1} would classify as trace icing; values from 1 to 6 g cm^{-2} h^{-1} would classify as light icing; from 6 to 12 g cm^{-2} h^{-1} would be moderate icing; and values greater than 12 g cm^{-2} h^{-1} would be heavy icing. Using this system, the WRF model would indicate 44% trace, 38% light, 12% moderate, and 7% heavy categorical icing during the 10 years of cool seasons (2001-2011). The actual percentages of icing PIREPs in this same period was 8% trace, 57% light, 34% moderate, and 1.4% severe as illustrated in Fig. 4.7. For comparison, Brown et al. (1997) found approximately 73% of PIREPs in the trace or light categories, 24% in the moderate category, and 3% in the heavy category for a multiple week period in March 1994.

There are two likely causes of large discrepancies in the model versus observed percentages. The first reason is that, in all likelihood, a model prediction of heavy icing will always be more frequently produced than it is observed since the harshest weather conditions will be under-sampled, because some pilots will avoid such conditions as would be the case in a widespread freezing drizzle or freezing rain case. Similarly, once a report of heavy/severe icing is broadcast, there is an obvious tendency to avoid this region as potentially dangerous. A second reason for large model discrepancy from observations relates to the trace icing category. This is generally considered relatively benign and operationally less important than more intense conditions of light or moderate icing. For this reason, we believe that reports of trace icing are greatly under-reported, which is supported by only 6092 trace icing reports collected in 60 months in contrast to over 72,000 reports of light and moderate intensity icing.

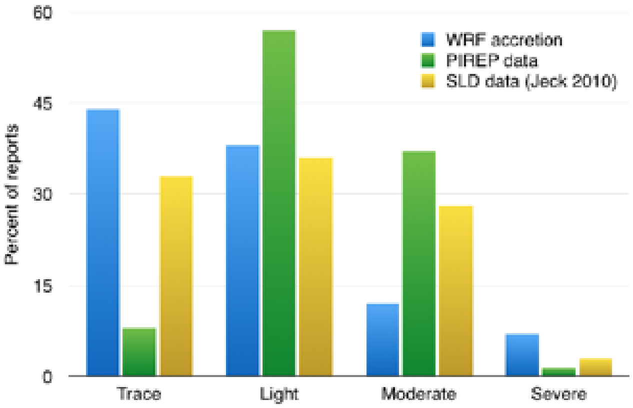

Fig. 4.7: Percentage of icing by category found using WRF model data (blue) with applied ice accretion rate proposed by Jeck (2010); corresponding percentage from actual icing PIREPs (green) in the 60 cool-season months; and percentages obtained by Jeck (2010) using the FAA database SLD data directly (yellow).

While the WRF model ice accretion calculations were computed assuming a standard cylinder, Jeck (1998) calculated ice accretion on various NACA wing profiles as well as the standard 3-inch cylinder and a 1/4-inch cylinder using the well known LEWICE computer software. Using the concept of the smaller cylinder to be an hypothetical icing rate detector, Jeck (2010) concluded that 33, 36, 28, and 3% of icing data points in the FAA SLD database would qualify as trace, light, moderate, and heavy icing respectively (Fig. 4.7). Since Jeck's analysis included only the SLD data and not the more common Appendix-C conditions, we might speculate that inclusion of all points in the FAA database may increase the percentages of trace and light icing categories and align better with the model results. Furthermore, one could hypothesize a method to scale the calculations of icing rate on a standard reference cylinder to various aircraft using the Jeck (1998) approach.

4.6 Case Study: 16 Jan 2013

Although aircraft icing occurs quite frequently in cool season months, there are not a large number of icing events that cause widespread impacts to the national aerospace system (NAS). Most icing events that cause havoc to the NAS are associated with large winter storms with heavy snow and ice at major airports, which often impose ground delays. One such case occurred on 16 Jan 2013 that included a weak area of low pressure located southeast of New York, with a warm front extending northeastward and a cold front southwestward toward Alabama. Throughout this entire region, a wide band of deep clouds was found along with heavy snow in the northeast U.S., widespread rain from Delaware to Georgia, and a persistent band of freezing rain and ice pellets located approximately from Pittsburg to Boston. This storm was not a typical "Nor'easter" with blizzard conditions in the New England states, but, rather a far weaker storm system that was less likely to capture the attention of major airlines to consider its operational impact.

The FAA William J. Hughs Technical Center provided operational logs from this event that showed all major airports from PHL to BOS with delays, diversions, ground stops, and runway closures due to the snow and ice. As the northeast corridor impacts intensified from 1000 to 1200 UTC, the resulting effects propagated to air travel as far away as Denver. Only after about 2200 UTC did the NAS start to recover to more typical operations as the weather pattern slowly propagated farther north and east, although residuals delays were noted in the logs for as long as 6 hours later. Besides the major disruptions associated with the winter surface conditions, there were a total of 494 trace to severe icing PIREPs collected from 0930 to 2130 UTC over the eastern half of the U.S.

To illustrate the potential value of applying numerical weather model data to predict events such as this, we processed the real-time HRRR model forecasts in the identical manner as we did the 10-year WRF simulation discussed in Section 4.3. HRRR repeatedly creates hourly forecasts from 1 to 15 hours each hour of the day. A user of these data might presume that the most recent model cycle combined with the shortest possible forecast time has the best overall skill to predict any particular clouds or weather features. However, due to uncertainties in observations and data assimilation together with model errors, it's highly possible that a blend of multiple model forecasts created from successive model cycles but valid all at the same time might improve icing prediction as compared to any individual, deterministic forecast.

For this reason, we performed an analysis of HRRR-based icing model predictive skill by individual as well as time-lag-ensemble average forecasts of supercooled liquid water when compared to pilot-reported icing during this event. The following evaluation was done by taking icing PIREPs from 30 minutes prior to 30 minutes after each hour (1200 to 2100 UTC) and inspecting the 4 x 4 set of grid boxes that surrounded the reported icing location for any presence (no matter the amount) of HRRR-predicted SLW, hence explicit icing. Table 4.1 below shows each verified hour in the first column, whereas the top

Table 4.1: Fraction of icing pilot reports (NEG, LGT, MOD) correctly predicted by the HRRR model forecasts of explicit supercooled liquid water within a 12 x 12 km^2 (4 x 4 grid boxes) area surrounding the PIREP location. The gray column used a time-lag-ensemble average (see text for details) including all HRRR hourly forecasts shown in each row. The final column shows the highest percent correct LGT and MOD PIREPs by any single HRRR forecast versus those correct using TLE method.

Valid\Init time (UTC)	**03z**	**06z**	**09z**	**12z**	**15z**	**18z**	**Time-lag ensmble**	**Best HRRR v. TLE**
12z	9/11 9/21 4/9	8/11 9/21 3/9	5/11 8/21 2/9	NA	NA	NA	4/11 16/21 4/9	43% v. 67%
13z	6/7 15/29 6/19	7/7 17/29 9/19	5/7 12/29 6/19	5/7 19/29 6/19	NA	NA	4/7 22/29 10/19	54% v. 67%
14z	3/6 12/26 8/25	4/6 16/26 11/25	4/6 9/26 10/25	5/6 6/26 11/25	NA	NA	2/6 18/26 14/25	53% v. 63%
15z	5/6 14/31 14/26	5/6 15/31 17/26	5/6 11/31 11/26	3/6 10/31 13/26	NA	NA	3/6 18/26 17/25	63% v. 69%
16z	6/7 15/30 9/25	6/7 17/30 15/25	5/7 17/30 8/25	6/7 14/30 13/25	4/7 17/30 15/25	NA	4/7 24/30 18/25	58% v. 76%
17z	4/6 15/25 11/24	6/6 16/25 19/24	4/6 12/25 13/24	3/6 11/25 13/24	6/6 14/25 16/24	NA	3/6 17/25 20/24	71% v. 76%
18z	6/6 17/30 14/21	6/6 16/30 14/21	6/6 8/30 13/21	6/6 16/30 13/21	5/6 16/30 8/21	NA	5/6 19/30 16/21	61% v. 69%
19z	NA	4/4 18/27 11/15	4/4 12/27 9/15	4/4 16/27 9/15	2/4 12/27 6/15	4/4 14/27 8/15	2/4 20/27 13/15	69% v. 79%
20z	NA	4/4 12/27 10/23	4/4 9/27 10/23	4/4 11/27 10/23	4/4 8/27 9/23	4/4 15/27 15/23	4/4 23/27 19/23	60% v. 84%
21z	NA	7/7 13/20 9/16	7/7 12/20 6/16	7/7 11/20 7/16	7/7 13/20 5/16	7/7 12/20 6/16	4/7 19/20 11/16	61% v. 83%

row indicates the starting cycle time of the HRRR. [Each forecast hour evaluated is simply the valid time in the first table column minus the initial time shown in the first table row.] The gray-highlighted column shows the fractions of correctly predicted icing PIREPs by using a time-lag-ensemble (TLE) average of all the forecast times shown across a table row. Each fraction of correctly captured icing reports for categories of negative icing (NEG), trace or light icing (LGT), and moderate or severe icing (MOD) are shown in each cell of the table. Of the total 457 trace to severe icing PIREPs in Table 4.1, only 12 were trace and 6 were severe, so trace was combined into the LGT category and severe was combined into the MOD category for simplification.

A model prediction was scored as correct if any of the 4 x 4 grid boxes surrounding the icing report had SLW regardless of reported severity; except in the case of negative icing in which case all 4 boxes immediately surrounding the PIREP had to have zero SLW. Given the spatial requirements employed in this method, the scoring treatment was far more stringent than previous, similar analyses (Brown et al. 1997) of icing predictive skill using much lower resolution numerical models (i.e., RUC). For this reason, we would expect this analysis to capture fewer total icing PIREPs in general, however, we used this technique in order to ascertain if the time-lag-ensemble methodology shows promise as compared to single deterministic HRRR forecasts of SLW.

Although this analysis represents a single case study, the results clearly indicate that majority of icing reports are properly captured with very stringent test of nearby grid boxes with explicit SLW. A prior study by Wolff and McDonough (2010) revealed that only about 20-25% of icing PIREPs were properly predicted by the SLW forecast in the RAP and RUC models. Therefore, the gain in forecast skill with the HRRR model and TLE method appears significant.

As we anticipated from viewing of multiple cases of various icing days, Table 4.1 does reveal what we found in subjective evaluations. For every single valid time shown, the time-lag-ensemble technique increases, sometimes substantially, the number of correctly captured icing PIREPs. An example benefit of the time-lag-ensemble average technique can be found for the 1800 UTC valid time. If we had assumed the shortest forecast time of 3 h from the 1500 UTC HRRR cycle time, we would only capture 8 of 21 MOD icing PIREPs; whereas if we choose the 12 h forecast started from 0600 UTC, we would have captured 14 of 21 MOD reports. Then, if we used the TLE method, we would capture 16 of 21 MOD reports. The final column in Table 4.1 combines the number of correctly predicted LGT and MOD icing PIREPs together for the best individual HRRR-based icing forecast as compared to the TLE method and clearly reveals the improvement gained when using multiple forecast times in an ensemble approach.

Also, as expected, there is a trade off with the correct prediction of negative icing reports. This is to be expected since taking averages of SLW from multiple forecasts will effectively "spread out" the total icing area anticipated at any valid time as compared to a single forecasted time. Unfortunately, there are no systematic and comprehensive reports of non-icing encounters that would truly be required to measure the actual False Alarm Ratio (FAR) of any icing forecast. The only true means to compute FAR for these model-based predictions would be to have routine and/or widespread measurements of SLW. As a potential alternative to FAR, Brown et al. (1997) calculated the total impacted airspace from predicted icing by various algorithms against the probability of detecting (POD) icing PIREPs. This concept could be applied in this analysis to determine the possibility of over-warning forecast icing conditions using the HRRR-based TLE approach versus the existing operational FIP icing forecasts.

To augment the values found in Table 4.1 and gain some sense of subjective fidelity of a time-lag-ensemble average HRRR forecast of surface and icing conditions aloft, we present graphics at 2-h intervals from this event in Fig. 4.8. Not every surface reporting location has a proper identification of every possible precipitation type and there are some known deficiencies (Ramsay, 1999) with reporting freezing drizzle (FZDZ), freezing rain (FZRA), and ice pellets (PL) in particular at various automated surface observing stations (ASOS) and automated weather observing stations (AWOS), however, these are the best available data at this time. In general, note that, at the surface (left side of Fig. 4.8), the observed locations of FZRA or FZDZ or PL are very well captured by the regions from the model showing similar conditions (various shades of orange/red), which are all indicative of SLD at the ground. Also the majority of regions with snow (SN, blue) and rain (RA, green) are also very well predicted by the HRRR-derived surface weather condition.

Similar to the surface prediction of icing conditions, the right panels of Fig. 4.8 show the results of ice accretion calculations after computing a time-lag-ensemble average of liquid water content and drop

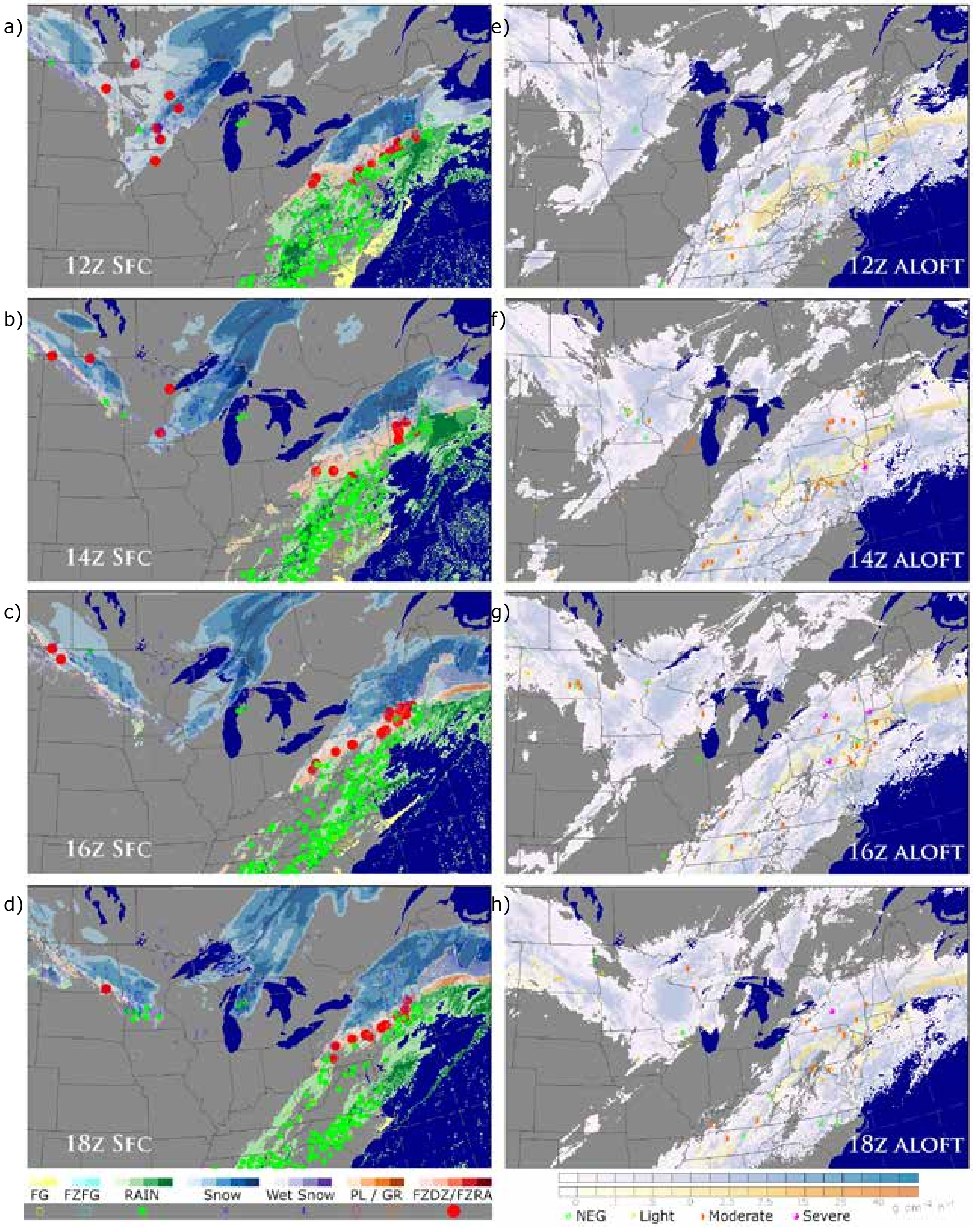

Fig. 4.8: Sequence of time-lag-ensemble forecasts from the HRRR model valid at (a) 1200, (b) 1400, (c) 1600, and (d) 1800 UTC 16 Jan 2013. The color filling on the left panels (a-d) represent model-predicted types of surface weather (legend at bottom) and the right-side panels (e-h) show model predicted ice accretion rates from Appendix-C drop sizes in blue shades and Appendix-O conditions in orange shades (see text for details). Observations of METAR surface condition and icing PIREPs are overlayed by symbol and color (see legend) from 30 minutes prior to 30 minutes after the time noted.

size applied in the same manner as found in the Appendix. Since there is a value of ice accretion at each of 50 levels in the model, the figure shows the maximum value found in a vertical column along with an overlay of the icing PIREP. As of this time, no attempt has been made to compare the model-predicted ice accretion rate to the icing PIREP intensity. Unfortunately due to the subjective nature of pilot's experience in icing, different handling characteristics of different airplanes in icing conditions, and the lack of systematic reports, a true statistical study of forecast skill of a numerical model's ice accretion rate will require more controlled measurements.

4.7 Conclusions

Numerical weather models have rapidly matured in recent years to give far more accurate predictions of water phase, amount, and droplet size that are critically important to aircraft and ground icing. Whereas only a couple decades ago the explicit prediction of supercooled water demonstrated very low skill, today's models show great promise to forecast explicitly the threat of icing conditions. The combination of increased computer power, higher horizontal and vertical model resolution, more extensive data assimilation techniques, and more complex and physically-based cloud physics parameterizations is responsible for the improvements. One such example is the Weather Research and Forecasting (WRF) model and its operational counterpart, the High Resolution Rapid Refresh (HRRR) when using the Thompson et al. (2008) and newer Thompson and Eidhammer (2014) microphysics parameterization.

The analysis presented here showed that the weather prediction model has skill at reproducing numerous characteristics of the environments associated with aircraft icing. In particular, the relationships between temperature, liquid water content, median volume diameter, and droplet concentration reasonably reproduce those relations seen in aircraft observations. The data shown in Figs. 4.2, 4.3 and 4.5 reveal the subtle yet important point that predicting two variables, mass and number concentration of cloud droplets and rain is necessary to encompass the range of LWC and MVD found in observations. A remaining hurdle to making accurate forecasts of cloud droplet number concentration is the prediction of the aerosols and CCN that form into cloud droplets. The comparison of observed versus modeled water droplet concentration in Fig. 4.6 revealed a potential bias in the new aerosol-aware microphysics scheme with the model creating too few droplets in all likelihood. The fewer but overall larger droplets are evident in Fig. 4.5 by the many points found to the right of the constant droplet concentration line of 25 cm^{-3}. Furthermore, a bias of too many clouds with MVD larger than 25 μm will accelerate the onset of drizzle through the subsequent collision-coalescence process. This is likely to be the cause of higher frequency of drizzle found in WRF (Fig. 4.4b) compared to the observations. It's also possible that the parameterized droplet freezing rate is potentially creating ice prematurely since there are very obvious trends of decreasing LWC when temperature decreases in the model as compared to the observations. The science of cloud chemistry and droplet activation is still in its early phases but also rapidly improving due to increasing computing power. As it matures, the subsequent model variables most important to icing environments will benefit. As another example, there is considerable uncertainty and natural variability in the activation of aerosols to become ice nuclei. Since ice crystals are more favored to grow by vapor diffusion at the expense of water droplets, improving the modeling of aerosols as ice nuclei will also impact the prediction of icing environments.

In the meantime, a model such as WRF/HRRR shows very promising results for predicting icing events at the surface and aloft, especially when applied with a time-lag-ensemble average from multiple HRRR SLW forecasts all valid at the same time. In the not too distant future, an ensemble of HRRR forecasts created using different data assimilation methods, different physical parameterizations or different lateral boundary conditions will be run from the same model cycle time and provide even more potential ensemble members to include in the technique. This is where the science of numerical weather prediction is naturally headed and rapid consideration of these new technologies and how they are applied to solve the needs of aviation is paramount to aviation safety and efficiency. Also, we believe that newer aircraft and ground icing products would show greater skill and future promise through more dedicated capture of observed icing and supercooled water conditions. As it was so clearly stated in Schultz and Politovich (1992): "It must be stressed that future research and development toward the icing forecast problem would be most effectively served by improved aircraft icing observations."

4.8 Appendix: Ice accretion rates

The equation (A1) used for ice accretion follows Makkonen (2000) where the change in ice mass with time is a product of a collision efficiency, α_1, (computed using A2-A8 following Finstad et al. 1998), *LWC*, velocity, v, and cross-sectional area of the cylinder, *A*. For simplicity, we used standard values of 76.2 mm (3 inches) diameter cylinder assumed to be moving at 89.1 m s^{-1} (200 mph), consistent with values used for decades by the aircraft icing research community. Computed rates in units of kg s^{-1} are converted to g cm^{-2} hr^{-1} and categorized as trace icing for rates below 1, light for rates from 1 to 6, moderate for rates from 6 to 12, and heavy for rates higher than 12 as proposed by Jeck (1980).

4.9 Acknowledgments

This research is in response to requirements and funding by the Federal Aviation Administration (FAA). The views expressed are those of the authors and do not necessarily represent the official policy or position of the FAA. Mr. Ben Bernstein is thanked for his many thoughtful comments on a draft of this paper and regarding aircraft icing as a whole. A team of colleagues in NCAR's Research Application Laboratory helped to make possible the 13-year WRF simulation that was used in this study and, we thank, in particular, Changhai Liu and Kyoko Ikeda for their massive efforts. Likewise, we thank WRF model developers at NCAR's Mesoscale and Microscale Meteorology division along with colleagues at NOAA's Earth System Research Laboratory. Starr McGettigan at the FAA's Wm. J. Hugh Technical Center is acknowledged for bringing to our attention the major icing event of 16 Jan 2013 and for providing the FAA logs for this date. NCAR is sponsored by the National Science Foundation. We would like to acknowledge high-performance computing support from Yellowstone (ark:/85065/d7wd3xhc) provided by NCAR's Computational and Information Systems Laboratory, sponsored by the National Science Foundation.

5. Conclusions

In an effort to simulate more realistically the particle size distribution of cloud droplets, the Thompson et al. (2008) bulk microphysics scheme was modified to predict the cloud drop number concentration in addition to previous mass mixing ratio. To do this, a new treatment of aerosol activation into CCN from a fully prognostic variable of available water-soluble aerosol number concentration was implemented in the WRF model. Furthermore, an aerosol species that is essentially considered mineral dust concentration was added as an explicit ice nuclei. In total, the three new additional predicted variables permit a coupled aerosol-aware microphysics scheme at a fraction of the cost of using the more computationally prohibitive WRF-Chem model (16% added CPU time versus an order of magnitude or more with WRF-Chem).

As detailed in Chapter 2, extensive testing of the new scheme revealed numerous sensitivities of aerosols to simulated cloud droplet spectra, associated radiative cloud properties, and precipitation development. By far, the most affected areas of precipitation were relatively low amounts, below about 2.5 mm h^{-1}, whereas more vigorous precipitating areas showed more subtle impacts from changing the aerosol number concentration. The scheme clearly demonstrated the long-established results of higher aerosol number concentration leading to overall smaller MVD but also higher LWC due to a hindered precipitation (warm-rain) process. Though initially a surprise, the study of a large winter cyclone case showed a noticeable shift in precipitation amounts with increased snowfall to the north of a warm front and decreased rainfall to the south. This was due to more cloud water carried in smaller droplets that were not as efficiently captured into rain in the south, but more efficiently captured by falling snow in the north. This implies a potential shift in regional precipitation and phase associated with aerosol increases or decreases and should be studied in greater detail in the future through much longer numerical integrations.

The winter cyclone case study presented in Chapter 2 together with the radiation coupling of water drop and ice crystal sizes presented in Chapter 3 rather clearly showed the importance of aerosol impacts to cloud particle size distributions and resulting radiation. Whereas most global climate models explicitly include the first aerosol indirect effect (Twomey, 1974), the described implementation of fully coupled cloud particle sizes and what the RRTM-G scheme uses in radiative transfer functions is newly added into WRF (although it is not new in WRF-Chem). Through an unintentional mistake in diagnosing the radiative effective diameter of snow, a series of experiments showed the sensitivity of cloud particle sizes to the shortwave and longwave radiation in WRF simulations. In the end, the a priori assumed particle sizes in the RRTM-G scheme may be appropriate for typical clouds, however, the prior coding in WRF would not have permitted appropriate simulation of known aerosol indirect effects: i.e., cloud albedo increase by smaller size drops in association with more pollution. The effort described in Chapter 3 completes the aerosol-radiation-cloud coupling needed for future WRF regional climate studies involving aerosol feedbacks to cloud properties. Unfortunately, results discussed in Chapter 3 also revealed that WRF simulations even using moderately high resolution of 4 km have deficient clouds, particularly within the mid-troposphere in mixed-phase conditions around 0 to -20°C. The well-known issue of properly predicting all cloud systems in the "gray zone" of physical parameterizations (~1-10 km grid spacing) was apparent from the results of Chapter 3. Besides the further refinement with smaller grid spacings, it is highly uncertain if more improvements to microphysics, turbulence, radiation or other model physical parameterization will suffice to create better explicit forecasts of clouds. Therefore, a subject of future research is a more sophisticated treatment of sub-grid, or unresolved, vertical motions responsible for some clouds.

In contrast to the single winter cyclone case presented in Chapter 2, the comparison in Chapter 4 provided a very robust test of the aerosol-aware microphysics scheme in the decade-long WRF simulation at high resolution over the Continental U.S. By comparing WRF-prediction supercooled water data to FAA aircraft icing data collected over multiple decades, there is a strong suggestion that the aerosol-aware scheme will require modifying to nucleate more aerosols as CCN due to sub-grid, unresolved vertical motions. Furthermore, there was sufficient evidence to consider altering the technique or parameterization to nucleate ice from water drops, because the model potentially had a deficit of moderately high LWC at temperatures of approximately -5 to -20°C; although this deficit could also be related to the same finding of Chapter 3 which was a general under-prediction of clouds in this temperature range.

Another primary conclusion noted in Chapter 4 is the potential for using WRF's explicitly-predicted supercooled liquid water amount and drop size to create forecasts of in-flight aircraft and ground icing events. From a case study of high-impact aircraft and ground icing, the skill of the real-time HRRR model to anticipate events such as this appears very favorable. Furthermore, using a time-lag-ensemble averaging technique to combine multiple real-time HRRR forecasts all valid at the same time captured far more reports from pilots of icing encounters than any single HRRR forecast. This finding has resulted in the FAA supporting further research and development at NCAR-RAL of en-route and airport terminal icing product development to support the safety and efficiency of the national aerospace system.

Additional future steps needed for the aerosol-aware scheme include more in-depth study of the ice initiation by mineral dust and the potential influence to precipitation production. Also, the initial version of the scheme used a very elementary surface aerosol emission formulation. A future topic remains to provide the scheme with a form of aerosol emission inventory data to replenish the aerosols and keep their number concentration well matched to the true atmosphere. At NCAR, the U.S. Environmental Protection Agency, and in the Brazilian weather service, the new Thompson and Eidhammer (2014) aerosol-aware scheme is being interfaced with much more sophisticated full chemistry models, because the existing tests have previously used climatological aerosol conditions. With coupling to other real-time models to provide real-time aerosols, the combined scheme should enhance the overall quality of cloud, radiation, and precipitation forecasts.

Ultimately, the aerosol-aware microphysics scheme could be a viable option to study future climate change projections related to aerosol impacts to radiation, clouds, precipitation, and water phase aloft and at the surface. As such, a wide range of applications could be investigated from aerosol impacts to surface transportation as well as to aviation and to renewable energy such as solar, hydro, and wind power. Furthermore, there exists the prospect of using long-duration WRF simulations (seasonal and longer) to quantify various aerosol direct and indirect effects as a baseline for GCMs.

6. References

Albrecht, B., 1989: Aerosols, cloud microphysics, and fractional cloudiness, Science, 245, 1227-1230.

Arenberg, D. L., 1943: Determination of icing conditions for airplanes. Trans. AGU, 24, 99-122.

Barlage, M., F. Chen, M. Tewari, K. Ikeda, D. Gochis, J. Dudhia, R. M. Rasmussen, B. Livneh, M. Ek, K. Mitchell, 2010: Noah land surface model modifications to improve snowpack prediction in the Colorado Rocky Mountains. J. Geophys. Res., 115:D22

Bigg, E. K., 1953: The supercooling of water. Proc. Phys. Soc., London, B66, 688-694.

Cober, S. G. and G. A. Isaac, 2012: Characterization of aircraft icing environments with supercooled large drops for application to commercial aircraft certification. J. Clim. Appl. Meteo., 51, 265 284.

Colarco, P., A. da Silva, M. Chin, and T. Diehl, 2010: Online simulations of global aerosol distributions in the NASA GEOS-4 model and comparisons to satellite and ground-based aerosol optical depth, J. Geophys. Res., 115, D14207.

Cooper, W.A., 1986: Ice Initiation in Natural Clouds. Meteorological Monographs, 21, 29–32.

Cui, Z., S. Davies, K. S. Carslaw and A. M. Blyth, 2011: The response of precipitation to aerosol through riming and melting in deep convective clouds. Atmos. Chem. Phys., 11, 3495-3510, doi:10.5194/acp-11-3495-2011.

Cziczo, D. J., D. M. Murphy, P. K. Hudson, and D. S. Thomson, 2004: Single particle measurements of the chemical composition of cirrus ice residue during CRYSTAL-FACE. J. Geophys. Res., 109, D04201.

Chin, Mian, and Coauthors, 2002: Tropospheric aerosol optical thickness from the GOCART model and comparisons with satellite and sun photometer measurements. J. Atmos. Sci., 59, 461–483.

DeMott, P. J., K. Sassen, M. R. Poellot, D. Baumgardner, D. C. Rogers, S. D. Brooks, A. J. Prenni, and S. M. Kreidenweis, 2003: African dust aerosols as atmospheric ice nuclei. Geophys. Res. Lett., 30, 1732.

——, and Coauthors, 2010: Predicting global atmospheric ice nuclei distributions and their impacts on climate. Proc. Natl. Acad. Sci. USA, 107, 11 217-11 222.

Dusek U., G. P. Frank, L. Hildebrandt, J. Curtius, J. Schneider, S. Walter, D. Chand, F. Drewnick, S. Hings, D. Jung, S. Borrmann, and M. O. Andreae, 2006: Size matters more than chemistry for cloud nucleating ability of aerosol particles. Science, 312, 1375-1378.

Eidhammer, T., P. J. DeMott, and S. M. Kreidenweis, 2009: A comparison of heterogeneous ice nucleation parameterizations using a parcel model framework. J. Geophys. Res., 114, D06202.

Fan, J.W., and Coauthors, 2009: Dominant role by vertical wind shear in regulating aerosol effects on deep convective clouds. J. Geophys. Res., 114, D22206.

Feingold, G., A. J. Heymsfield, 1992: Parameterizations of condensational growth of droplets for use in general circulation models. J. Atmos. Sci., 49, 2325–2342.

Finstad, K. J., E. P. Lozowski, and E. M. Gates, 1988: A computational investigation of water droplet trajectories. J. Atmos. Oceannic Technol., 5, 160-170.

Ghan, S. J., L. R. Leung, R. C. Easter, and H. Abdul-Razzak, 1997: Prediction of cloud droplet number in a general circulation model. J. Geophys. Res., 102(D18), 21777–21794.

——, H. Abdul-Razzak, A. Nenes, Y. Ming, X. Liu, M. Ovchinnikov, B. Shipway, N. Meskhidze, J. Xu, and X. Shi, 2011: Droplet nucleation: physically-based parameterizations and comparative evaluation. J. Adv. Model. Earth Syst., 3, M100001.

Ginoux, P., M. Chin, I. Tegen, J. M. Prospero, B. Holben, O. Dubovik, and S.-J. Lin, 2001: Sources and distributions of dust aerosols simulated with the GOCART model, J. Geophys. Res., 106(D17), 20255–20273.

Grabowski, W.W., and H. Morrison, 2011: Indirect impact of atmospheric aerosol in idealized simulations of convective-radiative quasi equilibrium. Part II: Double-moment microphysics. J. Clim., 24, 1897–1912.

Grell, G. A., S. E. Peckham, R. Schmitz, S. A. McKeen, G. Frost, W. C. Skamarock and B. Eder, 2005: Fully coupled online chemistry within the WRF model. Atmos. Environ., 39, 6957-6975.

Hindman, E. E. , E. Carter, R. Borys, and D. Mitchell, 1992: Collecting supercooled cloud droplets as a function of droplet size. J. Atmos. Oceanic Technol., 9, 337–353.

Hong, S.-Y., Y. Noh, and J. Dudhia, 2006: A new vertical diffusion package with explicit treatment of entrainment processes. Mon. Wea. Rev., 134, 2318–2341.

Hoose, C., J. E. Kristjánsson and S. M. Burrows (2010): How important is biological ice nucleation in clouds on a global scale? Environ. Res. Lett., 5, 024009.

Iacono, M.J., E.J. Mlawer, S.A. Clough and J.-J. Morcrette, 2000: Impact of an improved longwave radiation model, RRTM. on the energy budget and thermodynamic properties of the NCAR community climate mode, CCM3. J. Geophys. Res., 105, 14873-14890.

Igel, A. L., S. C. van den Heever, C. M. Naud, S. M. Saleeby, and D. J. Posselt, 2013: Sensitivity of warm-frontal processes to cloud-nucleating aerosol concentrations. J. Atmos. Sci., 70, 1768–1783.

Ikeda, K., and Coauthors, 2010: Simulation of seasonal snowfall over Colorado. Atmos. Res., 97, 462–477.

Jeck, R. K., 2001: A history and interpretation of aircraft icing intensity definitions and FAA rules for operating in icing conditions. FAA Technical Report, DOT/FAA/AR-01/91.

Khain, A.P., N. BenMoshe, and A. Pokrovsky, 2008: Factors determining the impact of aerosols on surface precipitation from clouds: An attempt at classification. J. Atmos. Sci., 65, 1721-1748.

——, L. R. Leung, B. Lynn, and S. Ghan, 2009: Effects of aerosols on the dynamics and microphysics of squall lines simulated by spectral bin and bulk parameterization schemes. J. Geophys. Res., 114, D22203.

Koop, T., B. P. Luo, A. Tsias, and T. Peter, 2000: Water activity as the determinant for homogeneous ice nucleation in aqueous solutions. Nature, 406(6796), 611-614.

Lebo, Z., and H. Morrison, 2013: A novel scheme for parameterizing aerosol processing in warm clouds. J. Atmos. Sci., in press.

Lee, S-S, G. Feingold, P. Y. Chuang, 2012: Effect of Aerosol on Cloud–Environment Interactions in Trade Cumulus. J. Atmos. Sci., 69, 3607–3632.

Levin, Z. and Cotton, W. R. (Eds.), 2009: Aerosol Pollution Impact on Precipitation: A Scientific Review, Springer, Heidelberg and Karlsruhe, Germany, 386 pp.

Li, Z., F. Niu, J. Fan, Y. Liu, D. Rosenfeld, and Y. Ding, 2011: Long-term impacts of aerosols on the vertical development of clouds and precipitation, Nature-Geoscience, 4, 888–894.

Liu, C., K., G. Thompson, R.M. Rasmussen, and J. Dudhia, 2011: High-resolution simulations of wintertime precipitation in the Colorado Headwaters region: sensitivity to physics parameterizations. Mon. Wea. Rev., 139, 3533–3553.

Lohmann, U., 2004: Can anthropogenic aerosols decrease the snowfall rate? J. Atmos. Sci., 61, 2457–2468.

Makkonen, L., 2000: Models for the growth of rime, glaze, icicles and wet snow on structures. Philos. Trans. R. Soc. London A, 358(1776), 2913–2939.

Molthan, A. and B. Colle, 2013: Comparisons of single- and double-moment microphysics schemes in the simulation of a synotic-scale snowfall event. Mon. Wea. Rev., in press.

Morales, R. and A. Nenes, 2010: Characteristic updrafts for computing distribution-averaged cloud droplet number and stratocumulus cloud properties. J. Geophys. Res., 115, D18220.

Morrison, H., J. O. Pinto, 2005: Mesoscale modeling of springtime arctic mixed-phase stratiform clouds using a new two-moment bulk microphysics scheme. J. Atmos. Sci., 62, 3683–3704.

——, and A. Gettelman, 2008: A new two-moment bulk stratiform cloud microphysics scheme in the Community Atmosphere Model, version 3 (CAM3). Part I: Description and numerical tests. J. Clim., 21, 3642–3659.

——, and W. W. Grabowski, 2011: Cloud system-resolving model simulations of aerosol indirect effects on tropical deep convection and its thermodynamic environment, Atmos. Chem. Phys., 11, 10503-10523.

——, ——, 2013: Response of tropical deep convection to localized heating perturbations: Implications for aerosol-induced convective invigoration, J. Atmos. Science, accepted.

Murray BJ; D. O'Sullivan, J. D. Atkinson, and M. E. Webb, 2012: Ice nucleation by particles immersed in supercooled cloud droplets. Chem. Soc. Rev., 41, 6519-6554.

Nygaard, B. E., K., J. E. Kristjánsson, and L. Makkonen, 2011: Prediction of in-cloud icing conditions at ground level using the WRF model. J. Appl. Meteor. Climatol., 50, 2445-2459.

Petters, M.D. and S.M. Kreidenweis, 2007: A single parameter representation of hygroscopic growth and cloud condensation nucleus activity. Atmos. Chem. Phys., 7, 1961–1971.

Phillips,V. T. J., P. J. DeMott, and C. Andronache, 2008:An empirical parameterization of heterogeneous ice nucleation for multiple chemical species of aerosol. J. Atmos. Sci., 65, 2757-2783.

Podolskiy, E. A., B. E. K. Nygaard, K. Nishimura, L. Makkonen, and E. P. Lozowski, 2012: Study of unusual atmospheric icing at Mount Zao, Japan, using the Weather Research and Forecasting model. J. Geophys. Res., 117, D12106.

Politovich, M. K. and T. A. O. Bernstein, 2002: Aircraft icing conditions in northeast Colorado. J. Appl. Meteo., 41, 118 132.

Qian, Y., D. Gong, J. Fan, L. R. Leung, R. Bennartz, D. Chen, and W. Wang, 2009: Heavy pollution suppresses light rain in China: Observations and modeling. J. Geophys. Res., 114, D00K02.

Rasmussen, R.M., and coauthors, 2011: High-resolution coupled climate runoff simulations of seasonal snowfall over Colorado: A process study of current and warmer climate. J. Clim., 24, 3015–3048.

——, and coauthors, 2012: How well are we measuring snow. Bull. Amer. Meteorol. Soc., 93, 811–829.

Richardson, M. S., and Coauthors, 2007: Measurements of heterogeneous ice nuclei in the western United States in springtime and their relation to aerosol characteristics. J. Geophys. Res., 112, D02209.

Rosenfeld, D., and coauthors, 2013: The common occurrence of highly supercooled drizzle and rain near the coastal regions of the western United States. J. Geophys. Res., 118, D50529.

Saleeby, S.M., and W.R. Cotton, 2004: A large-droplet mode and prognostic number concentration of cloud droplets in the Colorado State University Regional Atmospheric Modeling System (RAMS). Part I: Module descriptions and supercell test simulations. J. Appl. Meteor., 43, 182-195.

——, ——, 2008: A binned approach to cloud-droplet riming implemented in a bulk microphysics model. J. Appl. Meteor. Climatol., 47, 694–703.

——, ——, D. Lowenthal, R. D. Borys, and M. A. Wetzel, 2009: Influence of cloud condensation nuclei on orographic snowfall. J. Appl. Meteor. Climatol., 48, 903–922.

Sand, W. R., W. A. Cooper, M. K. Politovich, and D. L. Veal, 1984: Icing conditions encountered by a research aircraft. J. Clim. Appl. Meteo., 23, 1427 1440.

Seifert, A., C. Kohler, and K.D. Beheng, 2012: Aerosol-cloud-precipitation effects over Germany as simulated by a convective scale numerical weather prediction model. Atmos. Chem. Phys., 12, 709–725.

Skamarock, W.C., and J.B. Klemp, 2008: A time-split nonhydrostatic atmospheric model for weather research and forecasting applications. J. Comput. Phys., 227, 3465–3485.

Slingo, A., 1989: A GCM parameterization for the shortwave radiative properties of water cloud. J. Atmos. Sci., 46, 1419-1427.

Sorooshian, A., G. Feingold, M. D. Lebsock, H. Jiang, and G. L. Stephens, 2010: Deconstructing the precipitation susceptibility construct: Improving methodology for aerosol-cloud precipitation studies, J. Geophys. Res., 115, D17201.

Stephens, G. L., S. C. Tsay, P. W. Stackhouse, and P. J. Flatau, 1990: The relevance of the microphysical and radiative properties of cirrus clouds to climate and climatic feedback. J. Atmos. Sci., 47, 1742-1753.

Tao, W.-K., J.-P. Chen, Z. Li, C. Wang, and C. Zhang, 2012: Impact of aerosols on convective clouds and precipitation, Rev. Geophys., 50, RG2001.

Teller, A., and Z. Levin, 2008: Factorial method as a tool for estimating the relative contribution to precipitation of cloud microphysical processes and environmental conditions: Method and application. J. Geophys. Res., 113, D02202.

Thompson, G., R. M. Rasmussen, and K. Manning, 2004: Explicit forecasts of winter precipitation using an improved bulk microphysics scheme. Part I: Description and sensitivity analysis. Mon. Wea. Rev., 132, 519–542.

——, P. R. Field, R. M. Rasmussen, and W. D. Hall, 2008: Explicit forecasts of winter precipitation using an improved bulk microphysics scheme. Part II: Implementation of a new snow parameterization. Mon. Wea. Rev., 136, 5095-5115.

Twomey, S., 1974: Pollution and the planetary albedo. Atmos. Environ., 8, 1251-1256.

van den Heever, S.C., G.L. Stephens, and N.B. Wood, 2011: Aerosol indirect effects on tropical convection characteristics under conditions of radiative-convective equilibrium. J. Atmos. Sci., 68, 699-718.

Wang, X., L. Zhang, and M.D. Moran, 2010: Uncertainty assessment of current size-resolved parameterizations for below-cloud particle scavenging by rain. Atmos. Chem. Phys., 10, 5685–5705.

Ward, D. S., Eidhammer, T., Cotton, W. R., and Kreidenweis, S. M., 2010: The role of the particle size distribution in assessing aerosol composition effects on simulated droplet activation, Atmos. Chem. Phys., 10, 5435-5447.

Wong, D. C., J. Pleim, R. Mathur, F. Binkowski, T. Otte, R. Gilliam, G. Pouliot, A. Xiu, J. O. Young, and D. Kang, 2012: WRF-CMAQ two-way coupled system with aerosol feedback: software development and preliminary results. Geosci. Model Dev., 5, 299-312

Albrecht, B., 1989: Aerosols, cloud microphysics, and fractional cloudiness, Science, 245, 1227-1230.

Barlage, M., F. Chen, M. Tewari, K. Ikeda, D. Gochis, J. Dudhia, R. M. Rasmussen, B. Livneh, M. Ek, K. Mitchell, 2010: Noah land surface model modifications to improve snowpack prediction in the Colorado Rocky Mountains. J. Geophys. Res., 115:D22.

Bikos, D., and Coauthors, 2012: Synthetic satellite imagery for real-time high-resolution model evaluation. Wea. Forecasting, 27, 784–795.

Boucher, O., S. E. Schwartz, T. P. Ackerman, T. L. Anderson, B. Bergstrom, B. Bonnel, P. Chylek, A. Dahlback, Y. Fouquart, Q. Fu, R. N. Halthore, J. M. Haywood, T. Iversen, S. Kato, S. Kinne, A. Kirkevåg, K. R. Knapp, A. Lacis, I. Laszlo, M. I. Mishchenko, S. Nemesure, V. Ramaswamy, D. L. Roberts, P. Russell, M. E. Schlesinger, G. L. Stephens, R. Wagener, M. Wang, J. Wong, and F. Yang, 1998: Intercomparison of models representing direct shortwave radiative forcing by sulfate aerosols. J. Geophys. Res., 103, 16979-16998.

Bryan, G. H., J. C. Wyngaard, J. M. Fritsch, 2003: Resolution Requirements for the Simulation of Deep Moist Convection. Mon. Wea. Rev., 131, 2394–2416.

Chaboureau, J.-P., and J.-P. Pinty, 2006: Validation of a cirrus parameterization with Meteosat Second Generation observations. Geophys. Res. Lett., 33, L03815.

Chen, F., and J. Dudhia, 2001: Coupling an advanced land-surface/ hydrology model with the Penn State/ NCAR MM5 modeling system. Part I: Model description and implementation. Mon. Wea. Rev., 129, 569–585.

Chou, M.-D., M. J. Suarez, C.-H. Ho, M. M.-H. Yah, and K.-T. Lee, 1998: Parameterizations for cloud overlapping and shortwave single-scattering properties for use in general circulation and cloud ensemble models. J. Climate, 11, 202-214.

Cintineo, R., J. A. Otkin, M. Xue, and F. Kong, 2014: Evaluating the performance of planetary boundary layer and cloud microphysical parameterization schemes in convection-permitting ensemble forecasts using synthetic GOES-13 satellite observations. Mon. Wea. Rev., 142, 163–182.

Clark, A. J., and Coauthors, 2012: An overview of the 2010 Hazardous Weather Testbed Experimental Forecast Program Spring Experiment. Bull. Amer. Meteor. Soc., 93, 55–74.

——, M. C., Coniglio, B. E. Coffer, G. Thompson, M. Xue, and F. Kong, 2015: Sensitivity of 24-h Forecast Dryline Position and Structure to Boundary Layer Parameterizations in Convection-Allowing WRF Model Simulations. Wea. Forecasting, 30, 613-638.

Cox, G. P., 1988: Modelling precipitation in frontal rainbands. Quart. J. Roy. Meteor. Soc., 114, 115–127.

Diamond, H. J., T. R. Karl, M. A. Palecki, C. B. Baker, J. E. Bell, R. D. Leeper, D. R. Easterling, J. H. Lawrimore, T. P. Meyers, M. R. Helfert, G. Goodge, and P. W. Thorne, 2013: U.S. Climate Reference Network after one decade of operations: status and assessment. Bull. Amer. Meteor. Soc., 94, 489-498.

Dudhia, J., 1989: Numerical study of convection observed during the winter monsoon experiment using a mesoscale two-dimensional model. J. Atmos. Sci., 46, 3077-3107.

Feltz, W. F., K. M. Bedka, J. A. Otkin, T. Greenwald, and S. A. Ackerman, 2009: Understanding satellite-observed mountain wave signatures using high-resolution numerical model data. Wea. Forecasting, 24, 76–86.

Field, P. R., R. J. Hogan, P. R. A. Brown, A. J. Illingworth, T. W. Choularton, and R. J. Cotton, 2005: Parameterization of ice-particle size distributions for mid-latitude stratiform cloud. Quart. J. Roy. Meteor. Soc., 131, 1997–2017.

Fouquart, Y., J. Buriez, M. Herman, and R. Kandel, 1990: The influence of clouds on radiation: A climate-modeling perspective. Rev. Geophys., 28, 145–166.

Fu, Q., 1996: An accurate parameterization of the solar radiative properties of cirrus clouds for climate models. J. Climate, 9, 2058-2082.

——, P. Yang, and W. B. Sun, 1998: An accurate parameterization of the infrared radiative properties of cirrus clouds for climate models. J. Climate, 11, 2223–2237.

Grasso, L. D., and T. Greenwald, 2004: Analysis of 10.7-μm brightness temperatures of a simulated thunderstorm with two-moment microphysics. Mon. Wea. Rev., 132, 815–825.

——, M. Sengupta, J. F. Dostalek, R. Brummer, and M. DeMaria, 2008: Synthetic satellite imagery for current and future environmental satellites. Int. J. Remote Sens., 29, 4373–4384.

——, M. Sengupta, and M. DeMaria, 2010: Comparison between observed and synthetic 6.5 and 10.7 μm GOES-12 imagery of thunderstorms that occurred on 8 May 2003. Int. J. Remote Sens., 31, 647–663.

——, D. T. Lindsey, K.-S. Sunny Lim, A. J. Clark, D. Bikos, and S. R. Dembek, 2014: Evaluation of and suggested improvements to the WSM6 microphysics in WRF-ARW using synthetic and observed GOES-13 imagery. Mon. Wea. Rev., 142, 3635-3650.

Grell, G. A., S. E. Peckham, R. Schmitz, S. A. McKeen, G. Frost, W. C. Skamarock, and B. Eder, 2005: Fully coupled online chemistry within the WRF model. Atmos. Environ., 39, 6957– 6975

Heidinger, A. K., C. O'Dell, R. Bennartz, and T. Greenwald, 2006: The successive-order-of-interaction radiative transfer model. Part I: Model development. J. Appl. Meteor. Climatol., 45, 1388–1402.

Houze, R. A., P. V. Hobbs, P. H. Herzegh, and D. B. Parsons, 1979: Size distributions of precipitation particles in frontal clouds. J. Atmos. Sci., 36, 156–162.

Hu, Y. X., and K. Stamnes, 1993: An accurate parameterization of the radiative properties of water clouds suitable for use in climate models. J. Clim., 6, 728-742.

Iacono, M.J., E.J. Mlawer, S.A. Clough and J.-J. Morcrette, 2000: Impact of an improved longwave radiation model, RRTM, on the energy budget and thermodynamic properties of the NCAR community climate mode, CCM3. J. Geophys. Res., 105, 14873-14890.

IPCC, 2007: Climate Change 2007: The physical science basis. Contribution of working group I to the fourth assessment report of the Intergovernmental Panel on Climate Change [Solomon, S., D. Qin, M. Manning, Z. Chen, M. Marquis, K.B. Averyt, M. Tignor and H.L. Miller (eds.)]. Cambridge University Press, Cambridge, United Kingdom and New York, NY, USA, 996 pp.

Janjic, Z. I., 2002: Nonsingular implementation of the Mellor-Yamada Level 2.5 Scheme in the NCEP Meso model. NCEP Office Note No. 437, NOAA/NWS, 61 pp.

Jankov, I., L. D. Grasso, M. Sengupta, P. J. Neiman, D. Zupanski, M. Zupanski, D. Lindsey, D. W. Hillger, D. L. Birkenheuer, R. Brummer, and H. Yuan, 2011: An Evaluation of Five ARW-WRF Microphysics Schemes Using Synthetic GOES Imagery for an Atmospheric River Event Affecting the California Coast. J. Hydrometeor, 12, 618–633.

Karlsson, K.-G., 1996: Validation of modeled cloudiness using satellite-estimated cloud climatologies. Tellus, 48A, 767–785.

Kong, F., and Coauthors, 2014: CAPS Storm-Scale Ensemble Forecasting System: Impact of IC and LBC perturbations. Preprints, 26th WAF/22nd NWP Conf., Atlanta, GA, Amer. Meteor. Soc., Paper 119.

Lopez, P., K. Finkele, P. Clark, and P. Mascart, 2003: Validation and intercomparison of three FASTEX cloud systems: Comparison with coarse-resolution simulations. Quart. J. Roy. Meteor. Soc., 129, 1841–1871.

Mellor, G. L., and T. Yamada, 1982: Development of a turbulence closure model for geophysical fluid problems. Rev. Geophys., 20, 851–875.

Meyers, M. P., R. L. Walko, J. Y. Harrington, and W. R. Cotton, 1997: New RAMS cloud microphysics parameterization. Part II: The two-moment scheme. Atmos. Res., 45, 3–39.

Milbrandt, J. A., and M. K. Yau, 2005: A multimoment bulk microphysics parameterization. Part I: Analysis of the role of the spectral shape parameter. J. Atmos. Sci., 62, 3051–3064.

Mlawer, E. J., S. J. Taubman, P. D. Brown, M. J. Iacono, and S. A. Clough, 1997: Radiative transfer for inhomogeneous atmospheres: RRTM, a validated correlated-k model for the longwave. J Geophys. Res. 102, doi: 10.1029/97JD00237.

Morrison, H., and J. O. Pinto, 2005: Mesoscale modeling of springtime arctic mixed-phase stratiform clouds using a new two-moment bulk microphysics scheme. J. Atmos. Sci., 62, 3683–3704.

—— and Milbrandt, J. A., 2015: Parameterization of Cloud Microphysics Based on the Prediction of Bulk Ice Particle Properties. Part I: Scheme Description and Idealized Tests. J. Atmos. Sci., 72, 287-311.

Noh, Y., W. G. Cheon, S.-Y. Hong, and S. Raasch, 2003: Improvement of the K-profile model for the planetary boundary layer based on large eddy simulation data. Bound.-Layer Meteor., 107, 401–427.

O'Dell, C. W., A. K. Heidinger, T. Greenwald, P. Bauer, and R. Bennartz, 2006: The successive-order-of-interaction radiative transfer model. Part II: Model performance and applications. J. Appl. Meteor. Climatol., 45, 1403–1413.

Otkin, J. A., D. J. Posselt, E. R. Olson, H.-L. Huang, J. E. Davies, J. Li, and C. S. Velden, 2007: Mesoscale numerical weather prediction models used in support of infrared hyperspectral measurement simulation and product algorithm development. J. Atmos. Oceanic Technol., 24, 585–601.

——, and T. J. Greenwald, 2008: Comparison of WRF model-simulated and MODIS-derived cloud data. Mon. Wea. Rev., 136, 1957–1970.

——, T. J. Greenwald, J. Sieglaff, and H.-L. Huang, 2009: Validation of a large-scale simulated brightness temperature dataset using SEVIRI satellite observations. J. Appl. Meteor. Climatol., 48, 1613-1626.

Rikus, L., 1997: Application of a scheme for validating clouds in an operational global NWP model. Mon. Wea. Rev., 125, 1615–1637.

Skamarock, W. C., and J. B. Klemp, 2008: A time-split non-hydrostatic atmospheric model for weather research and forecasting applications. J. Comput. Phys., 227, 3465–3485.

Slingo, A., 1989: A GCM parameterization for the shortwave radiative properties of water cloud. J. Atmos. Sci., 46, 1419-1427.

Stensrud, D. J., 2007: Parameterization Schemes: Keys to Understanding Numerical Weather Prediction Models. Cambridge Univ. Press, 459pp.

Stephens, G. L., S. C. Tsay, P. W. Stackhouse, and P. J. Flatau, 1990: The relevance of the microphysical and radiative properties of cirrus clouds to climate and climatic feedback. J. Atmos. Sci., 47, 1742-1753.

Sun, Z., and L. Rikus, 2004: Validating model clouds and their optical properties using geostationary satellite imagery. Mon. Wea. Rev., 132, 2006–2020.

Tao, W.-K., J.-P. Chen, Z. Li, C. Wang, and C. Zhang, 2012: Impact of aerosols on convective clouds and precipitation, Rev. Geophys., 50, RG2001.

Thompson, G., R. M. Rasmussen, and K. Manning, 2004: Explicit forecasts of winter precipitation using an improved bulk microphysics scheme. Part I: Description and sensitivity analysis. Mon. Wea. Rev., 132, 519–542.

——, P. R. Field, R. M. Rasmussen, and W. D. Hall, 2008: Explicit forecasts of winter precipitation using an improved bulk microphysics scheme. Part II: Implementation of a new snow parameterization. Mon. Wea. Rev., 136, 5095-5115.

—— and T. Eidhammer, 2014: A study of aerosol impacts to clouds and precipitation development in a large winter cyclone. J. Atmos. Sci., 71, 3636-3658.

Tselioudis, G., and C. Jakob, 2002: Evaluation of midlatitude cloud properties in a weather and a climate model: Dependence on dynamic regime and spatial resolution. J. Geophys. Res., 107, 4781.

Twomey, S., 1974: Pollution and the planetary albedo. Atmos. Environ., 8, 1251-1256.

Wood, R., 2012: Stratocumulus Clouds. Mon. Wea. Rev., 140, 2373-2423.

Woods, C. P., M. T. Stoelinga, and J. D. Locatelli, 2007: The IMPROVE-1 storm of 1–2 February 2001. Part III: Sensitivity of a mesoscale model simulation to the representation of snow particle types and testing of a bulk microphysical scheme with snow habit prediction. J. Atmos. Sci., 64, 3927– 3948.

Xue, M., and Coauthors, 2010: CAPS realtime storm scale ensemble and high resolution forecasts for the NOAA Hazardous Weather Testbed 2010 Spring Experiment. Preprints, 25th Conf. on Severe Local Storms, Denver, CO, Amer. Meteor. Soc., Paper 7B.3.

Zamora, R. J., E. G. Dutton, M. Trainer, S. A. McKeen, J. M. Wilczak, and Y.-T. Hou, 2005: The Accuracy of Solar Irradiance Calculations Used in Mesoscale Numerical Weather Prediction. Mon. Wea. Rev., 133, 783–792.

Federal Aviation Administration, 1999: Part 25: Airworthiness Standard: Transport Category Airplanes, Appendix C. Title 14: Aeronautics and Space, U.S. Code of Federal Regulations, 9 pp. [Available from the Office of the Federal Register, National Archives and Records Administration, Washington, DC 20402-9328.]

Sand, W. R., W. A. Cooper, M. K. Politovich, and D. L. Veal, 1984: Icing Conditions Encountered by a Research Aircraft. J. Clim. Appl. Meteo., 23, 1427-1440.

Jeck, R. K., 2001: A History and Interpretation of Aircraft Icing Intensity Definitions and FAA Rules for Operating in Icing Conditions. FAA Technical Report, DOT/FAA/AR-01/91.

NTSB, 1996: Aircraft Accident Report, ATR Model 72-212, Roselawn, Indiana, October 31, 1994. NTSB/AAR-96/01, National Transportation Safety Board.

Marwitz, J., M. Politovich, B. Bernstein, F. Ralph, P. Neiman, R. Ashenden, and J. Bresch, 1996: Meteorological Conditions Associated with the ATR72 aircraft accident near Roselawn, Indiana on 31 October 1994. Bull. Amer. Meteor. Soc., 78, 41-52.

Cober, S. G. and G. A. Isaac, 2012: Characterization of Aircraft Icing Environments with Supercooled Large Drops for Application to Commercial Aircraft Certification. J. Clim. Appl. Meteo., 51, 265-284.

Cober, S., B. Bernstein, R. Jeck, E. Hill, G. Isaac, J. Riley, and A. Shah, 2009: Data and Analysis for the Development of an Engineering Standard for Supercooled Large Drop Conditions. FAA Technical Report, DOT/FAA/AR-09/10, 89pp

Federal Aviation Administration, 2014: Parts 25 and 33: Airplane and Engine Certification Requirements in Supercooled Large Drop, Mixed Phase, and Ice Crystal Icing Conditions; Final Rule, U.S. Code of Federal Regulations, Vol. 79, #213. [Available from the Office of the Federal Register, National Archives and Records Administration, Washington, DC 20402-9328.]

Schultz, P., and M. K. Politovich, 1992: Toward the improvement of aircraft icing forecasts for the continental United States. Wea. Forecasting, 7, 492–500.

Forbes, G. S., Y. Hu, B. G. Brown, B. C. Bernstein, and M. K. Politovich, 1993: Examination of conditions in the proximity of pilot reports of icing during STORM-FEST. Preprints, Fifth Int. Conf. on Aviation Weather Systems, Vienna, VA, Amer. Meteor. Soc., 282–286.

Thompson, G., R. Bruintjes, B. Brown, and F. Hage, 1997: Intercomparison of In-Flight Icing Algorithms. Part I: WISP94 Real-Time Icing Prediction and Evaluation Program. Wea. Forecasting, 12, 878-889.

Bernstein, B.C., F. McDonough, M.K. Politovich, B.G. Brown, T.P. Ratvasky, D.R. Miller, C.A. Wolff, and G. Cunning, 2005: Current Icing Potential (CIP): Algorithm Description and Comparison with Aircraft Observations, J. Appl. Meteor., 44, 969-986.

Thompson, G., P. R. Field, R.M. Rasmussen, and W. D. Hall, 2008: Explicit Forecasts of winter precipitation using an improved bulk microphysics scheme. Part II: Implementation of a new snow parameterization. Mon. Wea. Rev., 136, 5095–5115.

Thompson, G. and T. Eidhammer, 2014: A study of aerosol impacts on clouds and precipitation development in a large winter cyclone. J. Atmos. Sci., 71, 3636–3658.

Jeck, R. K., 1998: A workable, aircraft-specific icing severity scheme. Paper No. AIAA-98-0094, 36th AIAA Aerospace Sciences Meeting, Reno, Nevada, Jan 1998.

Jeck, R. K., 2010: Models and Characteristics of Freezing Rain and Freezing Drizzle for Aircraft Icing Applications. FAA Technical Report, DOT/FAA/AR-09/45.

Lewis, W., D. B. Kline, and C. P. Steinmetz, 1947: A further investigation of the meteorological conditions conducive to aircraft icing. NACA TN 1424.

Skamarock, W. C. and J. B. Klemp, 2008: A Time-split Nonhydrostatic Atmospheric Model for Weather Research and Forecasting. J. Comput. Phys., 227, 3465-3485.

Benjamin, S., J. M. Brown, and T. Smirnova, 2016: Explicit Precipitation-Type Diagnosis from a Model Using a Mixed-Phase Bulk Cloud–Precipitation Microphysics Parameterization. Wea. Forecasting, early online release.

Barlage, M., and Coauthors, 2010: Noah land surface model modifications to improve snowpack prediction in the Colorado Rocky Mountains. J. Geophys. Res., 115, D22101, doi:10.1029/2009JD013470.

Iacono, M. J., E. J. Mlawer, S. A. Clough, and J.-J. Morcrette, 2000: Impact of an improved longwave radiation model, RRTM, on the energy budget and thermodynamic properties of the NCAR community climate mode, CCM3. J. Geophys. Res., 105, 14 873–14 890, doi:10.1029/2000JD900091.

Hong, S.-Y., Y. Noh, and J. Dudhia, 2006: A new vertical diffusion package with explicit treatment of entrainment processes. Mon. Wea. Rev., 134, 2318–234.

Thompson, G., M. Tewari, K. Ikeda, S. Tessendorf, C. Weeks, J. Otkin and F. Kong, 2016: Explicitly-coupled cloud physics and radiation parameterization and subsequent evaluation in WRF high-resolution convective forecasts. Atmos. Res., 168, 92–104.

Politovich, M. K. and T. A. O. Bernstein, 2002: Aircraft Icing Conditions in Northeast Colorado. J. Appl. Meteo., 41, 118-132.

Bigg, E. K., 1953: The supercooling of water. Proc. Phys. Soc., London, B66, 688-694.

Rosenfeld, D., and coauthors, 2013: The Common Occurrence of Highly Supercooled Drizzle and Rain Near the Coastal Regions of the Western United States. J. Geophys. Res., 118, D50529.

Makkonen, L., 2000: Models for the Growth of Rime, Glaze, Icicles and Wet Snow on Structures. Philos. Trans. R.

Soc. London A, 358(1776), 2913-2939.

Nygaard, B. E. K., J. E. Kristjansson, and L. Makkonen, 2011: Prediction of in-cloud icing conditions at ground level using the WRF model. J. Appl. Meteor., 50, 2445-2459.

Podolskiy, E. A., B. E. K. Nygaard, K. Nishimura, L. Makkonen, and E. P. Lozowski, 2012: Study of unusual atmospheric icing at Mount Zao, Japan, using the Weather Research and Forecasting model. J. Geophys. Res., 117, D12106, doi:10.1029/ 2011JD017042.

Jeck, R. K., 1980: Icing characteristics of low altitude supercooled layer clouds. FAA Technical Report, DOT/FAA/ RD-80-24.

Brown, B., G. Thompson, R. Bruintjes, R. Bullock, and T. Kane, 1997: Intercomparison of In-flight Icing Algorithms. Part II: Statistical Verification Results. Wea. & Forecasting, 12, 890-914.

Wolff, C. and F. McDonough, 2010: A comparison of WRF-RR and RUC forecasts of aircraft icing conditions. Preprints, 14th Conference on Aviation, Range, and Aerospace Meteorology, Atlanta, GA, Amer. Meteor. Soc.

Ramsay, A., 1999: A multi-sensor freezing drizzle algorithm for the automated surface observing system. Preprints, 15th Int. Conf. on Interactive Information and Processing Systems for Meteorology, Oceanography, and Hydrology, Dallas, TX, Amer. Meteor. Soc., 193–196.

Finstad, K. J., E. P. Lozowski, and E. M. Gates, 1988: A Computational Investigation of Water Droplet Trajectories. J. Atmos. Oceannic Technol., 5, 160-170.